

# Pressure evolutions of electronic and crystal structures of europium compounds

---

**Dhami, Naveen Singh**

**Doctoral thesis / Doktorski rad**

**2024**

*Degree Grantor / Ustanova koja je dodijelila akademski / stručni stupanj:* **University of Zagreb, Faculty of Science / Sveučilište u Zagrebu, Prirodoslovno-matematički fakultet**

*Permanent link / Trajna poveznica:* <https://um.nsk.hr/um:nbn:hr:217:189091>

*Rights / Prava:* [In copyright](#)/[Zaštićeno autorskim pravom.](#)

*Download date / Datum preuzimanja:* **2025-03-23**



*Repository / Repozitorij:*

[Repository of the Faculty of Science - University of Zagreb](#)





University of Zagreb

Faculty of Science  
Department of Physics

Naveen Singh Dhani

**Pressure evolutions of electronic and crystal  
structures of europium compounds**

DOCTORAL DISSERTATION

Zagreb, 2024



University of Zagreb

Faculty of Science  
Department of Physics

Naveen Singh Dhani

**Pressure evolutions of electronic and crystal  
structures of europium compounds**

DOCTORAL DISSERTATION

Supervisor:  
Dr. sc. Yuki UTSUMI BOUCHER

Zagreb, 2024



Sveučilište u Zagrebu

Prirodoslovno-matematički fakultet

Fizički odsjek

Naveen Singh Dhani

**Evolucije elektroničkih i kristalnih struktura  
spojeva europija u ovisnosti o tlaku**

DOKTORSKI RAD

Mentor:

Dr. sc. Yuki Utsumi Boucher

Zagreb, 2024

# Supervisor information

**Dr. Sc. Yuki Utsumi Boucher**

## **Education**

- Doctor of Science (Physics), Graduate School of Science, Hiroshima University, Japan : 2013: Doctoral thesis: Electronic structure of Yb-based Kondo compounds YbInCu<sub>4</sub> and YbNi<sub>3</sub>X<sub>9</sub> (X=Al, Ga) investigated by means of photoemission spectroscopy
- Master of Science (Physics), Graduate School of Science, Hiroshima University, Japan : 2010 : Master thesis: Studies of valence transition in YbInCu<sub>4</sub> and unoccupied electronic structure of FeAs-based superconductors (in Japanese)
- Bachelor of Science (Physics), School of Science, Hiroshima University, Japan : 2008 : Bachelor thesis: Angle resolved inverse photoemission spectroscopy of charge density wave compound 1T-TaS<sub>2</sub> (in Japanese)

## **Employment history**

- Dec. 2023-current: Senior research associate, Institute of Physics, Croatia
- Jul. 2018–Dec. 2023: Research associate, Institute of Physics, Croatia
- Mar. 2018–Jul. 2018: Postdoctoral researcher, Institute of Physics, Croatia
- Jan. 2016–Jan. 2018: Postdoctoral researcher, GALAXIES beamline, Synchrotron SOLEIL, France
- Apr. 2013–Dec. 2015: Postdoctoral researcher, Max-Planck Institute for Chemical Physics of Solids, Germany
- Apr. 2010–Mar. 2013: PhD research assistant (part time), Graduate School of Science, Hiroshima University, Japan

---

## **Fellowships and awards**

- 2011–2013: Hayashi Memorial Foundation for Female Natural Scientists
- 2012: Best student poster award (The 16<sup>th</sup> Hiroshima International Symposium on Synchrotron radiation)
- 2008: Best speaker of undergraduate thesis presentation, School of Science, Hiroshima University, Japan

## **Project participation and project management**

- 2020-current: UIP-2019-04-2154 Croatian science foundation installation research project, “Pressure-and Temperature-drive phase transition in strongly correlated electron systems” (principal investigator)
- 2019-current: DOK-2018-09-9906 Croatian science foundation young researcher’s career development project-training of doctoral student (mentor of Naveen Singh Dhami)
- 2018-2022: IP-2016-06-7258 Croatian science foundation research project, “The physics of many body systems-exploiting the world of complexity” (associate)

## **Few selected recent publications**

- Boucher, Y. U., et al. "Intercalation-induced states at the Fermi level and the coupling of intercalated magnetic ions to conducting layers in  $\text{Ni}_{1/3}\text{NbS}_2$ ." *Physical Review B* 109.8 (2024): 085135.
- Dhami, N. S., et al. "Pressure evolution of electronic and crystal structure of noncentrosymmetric  $\text{EuCoGe}_3$ ." *Physical Review B* 107.15 (2023): 155119.
- Takegami, D., et al. "Direct imaging of valence orbitals using hard x-ray photoelectron spectroscopy." *Physical Review Research* 4.3 (2022): 033108.
- Popčević, P., et al. "Role of intercalated cobalt in the electronic structure of  $\text{Co}_{1/3}\text{NbS}_2$ ." *Physical Review B* 105.15 (2022): 155114.
- Utsumi, Y., et al. "Pressure evolution of the electronic structure of non-centrosymmetric  $\text{EuRhGe}_3$ ." *Electronic structure* 3.3 (2021): 034002.
- Utsumi, Y., et al. "Electronic Structure of  $\text{Yb}(\text{Ni}_{1-x}\text{Co}_x)_3\text{Ga}_9$  Studied by Angle-resolved Photoelectron Spectroscopy." *Journal of the Physical Society of Japan* 89.4 (2020): 044711

# Acknowledgements

I am deeply grateful to my parents for the gift of life and their unwavering support throughout my journey.

I extend my sincerest appreciation to my supervisor, Dr. Yuki Utsumi Boucher, for her invaluable guidance, patience, and boundless expertise, which have been instrumental in the success of this research project. I am also thankful to Dr. Petar Popčević, our group leader, for his continuous support and guidance. Additionally, I extend my gratitude to Prof. Victor Balédent for his invaluable contributions during synchrotron experiments and his assistance with preliminary lab measurements for synchrotron experiments. Furthermore, I would like to express my gratitude to Dr. C.M.N. Kumar for guiding me through XRD data refinement and structure solution.

I express my gratitude towards Dr. O. Bednarchuk and Prof. D. Kaczorowski for providing me high quality single crystals of europium compounds.

Special appreciation is extended to the beamline scientists at the Soleil synchrotron Dr. J. M. Ablett and Dr. J.-P. Rueff at the Galaxies beamline, Dr. J. P. Itié at the Psiche beamline, Dr. F. Pierre at the Cristal beamline, and Dr. L. Nataf at the ODE beamline for their pivotal role in facilitating various synchrotron experiments. I would also like to thank the staffs of the High pressure laboratory in SOLEIL synchrotron for their skillful technical support.

I extend my appreciation to Prof. Ivo Batistić for his expertise in DFT calculations and theoretical guidance. Additionally, I am grateful to Dr. Eduard Tutiš, Prof. Denis Sunko and Prof. Neven Barišić for engaging discussions on various topics and scientific ethics, which greatly enriched my research experience. I acknowledge Prof. S. R. Shieh for his invaluable contribution to the sample preparation for high-pressure synchrotron experiments and helpful discussions which supported my research endeavors. Special thanks are extended to Marko Hum for his constant assistance with doctoral courses and paperwork. I would like to thank Dr. Nikolina Novosel and Josip Pogačić for their work in handling cryogenics at the Institute of Physics. Special appreciation is extended to Marija Sobol for her invaluable assistance with administrative tasks. I also gratefully acknowledge the support received from Dr. Osor Slaven

---

Barišić, Dr. Ana Smontara and Dr. Tomislav Vuletić. Additionally, I would like to extend my gratitude to the technicians from the institute workshop for their precision in machining various parts essential to my research. Furthermore, I am thankful to the dedicated cleaning staffs, finance and project management teams, and IT supports at the Institute of Physics for their indispensable contributions to maintaining a conducive environment for scientific research.

My heartfelt thanks go out to all my colleagues and lab mates, including Priyanka Reddy, Seyed Ashkan Moghadam Ziabari, Gaurav Pransu, Pavla Senug, Bruno Gudac, Saswat Mishra, Marija Zorić, Juraj Krsnik and Wojciech J. Sas, for their camaraderie and support throughout my academic journey. I am indebted to Pooja Negi Dhama, D. Jadoun, S. Bam, K. K. Bisht, P. Gusain, V. Agarwal, and P. Jeena for their unwavering support and presence during challenging times.

I will always be grateful to P. Digari, Prof. Nandan Bisht, Dr. Pawan Joshi, Prof. D. S. Dhama, and Prof. M. C. Durgapal for inspiring me to pursue a career in physics. I also extend my heartfelt thanks to Prof. K. Das Gupta for his continuous support and guidance throughout my academic journey.

I would like to acknowledge financing from the Croatian Science Foundation under the “Young Researchers’ Career Development Project:” Project No. DOK-2018-09-9906, and Croatian Science Foundation under the project numbers, IP-2016-06-7258, IP 2020-02-9666 and UIP 2019-04-2154, and by the project Cryogenic Centre at the Institute of Physics – KaCIF co-financed by the Croatian Government and the European Union through the European Regional Development Fund-Competitiveness and Cohesion Operational Programme (Grant No. KK.01.1.1.02.0012).

I extend my thanks to Prof. Neven Barišić, Prof. Mario Novak, and Dr. Dino Novko for generously dedicating their time to read and evaluate the thesis.

Last but not least, special thanks to all of my family and friends for continuous support and help.

# Abstract

In this thesis, I present results of evolution of electronic and crystal structures of non-centrosymmetric  $\text{EuTGe}_3$  ( $T = \text{Co, Rh and Ir}$ ) under hydrostatic pressure.

**Keywords:** High-pressure, Strongly correlated electron system, Eu valence, Intermediate valence, Non-centrosymmetric crystal structure.

Since the discovery of the first heavy-fermion superconductor  $\text{CeCu}_2\text{Si}_2$ , more than 30 systems have been discovered that exhibit unconventional  $f$ -electron superconductivity. Most of them belong to Ce and U compounds, and their phase diagrams are often discussed by using the Doniach model. The ground state is characterized by the competition between the Kondo effect and the Ruderman Kittel-Kasuya-Yosida (RKKY) interaction, which originates from the interaction of localized  $f$ -electrons with conduction electrons. The Kondo effect screens the magnetic moments, while the RKKY interactions stabilize the magnetic ordering. Superconductivity tends to appear near the magnetic quantum critical point (QCP). Recently, pressure induced heavy-fermion superconductors have been discovered among  $\text{CeTX}_3$  ( $T = \text{Co, Rh, Ir}$ ;  $X = \text{Si, Ge}$ ) with the  $\text{BaNiSn}_3$ -type ( $I4mm$ ) structure which does not possess inversion symmetry. They have attracted much attention due to the possible coexistence of spin-singlet and -triplet Cooper channels initiated by antisymmetric spin-orbit interaction as well as strong correlations.

A series of Eu compounds  $\text{EuTX}_3$  were also discovered with the  $\text{BaNiSn}_3$ -type structure. Although the emergence of pressure-induced superconductivity has not been reported, their complex magnetic structures are of great interest to the scientific community. Germanide series  $\text{EuTGe}_3$  exhibits antiferromagnetic ordering below  $\sim 16$  K, and the ordering direction of moments varies depending on the transition metal constituent. In  $\text{EuRhGe}_3$  the AFM order sets in at  $T_N = 11.3$  K and the Eu moments are confined in the  $ab$  plane, while they are aligned along the  $c$ -axis in  $\text{EuCoGe}_3$ , and  $\text{EuIrGe}_3$  that order at  $T_N = 15.4$ , and 12.3 K, respectively. Below  $T_N$ , successive magnetic phase transitions were observed at  $T_{N'} = 13.4$  K in  $\text{EuCoGe}_3$ , and  $T_{N'}$

---

= 7.5 K and  $T_{N^*} = 5.0$  K in  $\text{EuIrGe}_3$ . A smaller number of compounds have been reported in silicides compared to germanides. Among them, antiferromagnetic  $\text{EuRhSi}_3$  was recently discovered to exhibit an atypical pressure behavior that cannot be explained by the conventional phase diagram of Eu compounds.

In Eu-compounds, Eu ions tend to be  $\text{Eu}^{2+}$  ( $4f^7$ ,  $J=7/2$ ) and form an antiferromagnetic ground state. However, the energy difference between the magnetic  $\text{Eu}^{2+}$  and the non-magnetic  $\text{Eu}^{3+}$  ( $4f^6$ ,  $J=0$ ) states is not very large and can be adjusted by external pressure or chemical substitution. Among Eu-compounds, the most insensitively studied series is  $\text{EuT}_2\text{X}_2$  ( $T$ : transition metal,  $X =$  group 14/15 in the periodic table) with the  $\text{ThCr}_2\text{Si}_2$ -type ( $I4/mmm$ ) structure. In general, their pressure-temperature phase diagram exhibits a first-order phase transition accompanied by Eu valence transition and collapse of the antiferromagnetic ordering. Furthermore, a correlation between the Eu valence and the unit cell volume tends to appear as a lattice volume collapse simultaneously with the Eu valence transition since the size of the  $\text{Eu}^{3+}$  ion is about 10% smaller than the  $\text{Eu}^{2+}$  ion.

Although the  $\text{BaNiSn}_3$ -type structure is a close relative to the  $\text{ThCr}_2\text{Si}_2$ -type structure, the pressure-temperature phase diagram of the  $\text{EuTX}_3$  series and the relation between Eu valence and unit cell volume have not been studied well. A few earlier studies reported a stable antiferromagnetic ground state in  $\text{EuTX}_3$  even under high pressure of  $\sim 10$  GPa, unlike the Eu-compounds with the  $\text{ThCr}_2\text{Si}_2$ -type structure (Eu122 systems) that usually show the phase transitions in a few GPa range. Moreover, as mentioned earlier,  $\text{EuRhSi}_3$  exhibits an atypical pressure behavior in that  $T_N$  takes a maximum at 5-7 GPa and smoothly decreases with an increase of pressure in a manner compatible with the Doniach-type phase diagram. These results suggest a clear distinction of  $\text{EuTX}_3$  characters from the Eu122-systems. Therefore, the pressure-dependent structural change in the  $\text{EuTGe}_3$  series and its relation to the Eu valence evolutions are studied in this thesis by using multiple experimental techniques. The valence state of Eu provides complementary information for understanding the magnetic properties and phase diagram of these compounds under pressure.

The thesis presents the study of the evolution of electronic and crystal structures in non-centrosymmetric  $\text{EuTGe}_3$  ( $T = \text{Co, Rh \& Ir}$ ) under hydrostatic pressure. The investigation involved pressure dependent high energy resolved fluorescence detected (HERFD) X-ray absorption spectroscopy (XAS) experiments conducted on  $\text{EuTGe}_3$ . No pressure-induced transition in the Eu valence was observed in any of the three compounds. In the case of  $\text{EuCoGe}_3$ , the obtained Eu valence changes from 2.2 to 2.3 in the pressure range from 2 to 50 GPa. The XAS spectra recorded on Ge  $K$  and Co  $K$  edge as a function of pressure did not show significant changes. This indicates that the pressure evolution of the mean Eu valence is due to

---

intra-atomic charge transfer from Eu  $4f$  to  $5d$ , with no contribution from Ge and Co ions. The pressure-dependent Eu  $L_3$  HERFD XAS of EuRhGe<sub>3</sub> shows a change of Eu valence from 2.1 to 2.4 around 40 GPa. Similarly, the pressure-dependent Eu  $L_3$  HERFD XAS spectra of EuIrGe<sub>3</sub> showed the Eu valence change from 2.1 to 2.43 around 50 GPa. The Eu  $L_3$  transmission mode XAS of EuIrGe<sub>3</sub> as a function of pressure were also recorded at 300 K and 4 K up to 50 GPa, which shows a similar pressure evolution of Eu valence as HERFD XAS. The XAS spectra recorded at the Ge  $K$  edge of EuIrGe<sub>3</sub> reveal a spectral intensity shift as pressure increases. Specifically, the Ge  $K$  XAS spectra shift from an absorption peak at 11102 eV associated with Ge ions at Wyckoff 4b to a peak at 11108 eV associated with Ge ions at Wyckoff 2a. The Ir  $L_3$  absorption peak shifts to higher energy with an increase of pressure. These results suggest a possible effect of inter-atomic charge transfer in the evolution of Eu valence in EuIrGe<sub>3</sub>.

At ambient pressure, all three compounds show the mean Eu valence close to  $\sim 2.1$ , the maximum change of mean Eu valence with pressure was observed for EuIrGe<sub>3</sub> and minimum change for EuCoGe<sub>3</sub>.

To study the correlation between the pressure evolution of the electronic structure and crystal structure, powder x-ray diffraction under pressure was performed on EuTGe<sub>3</sub>. No pressure induced structure transition was observed in all three compounds up to 40 GPa. Anisotropic compression between the  $a$  and the  $c$  lattice parameters was observed, where the  $a$  lattice parameter showed a larger change compared with the  $c$  lattice parameter. This pressure behaviour is in contrast to that of centrosymmetric Eu-122 systems. In the Eu-122 systems, the  $c$  lattice parameter is more compressed than the  $a$  lattice parameter under pressure. The pressure evolution of axial ratio ( $c/a$ ) shows linear increase with increasing pressure and exhibits a slope change at certain pressure in all three compounds. No direct correlation between unit cell volume and Eu valence was found in the non-centrosymmetric EuTGe<sub>3</sub> series, contrasting with the behavior observed in the Eu-122 systems.

To investigate the potential pressure induced superconductivity, electric resistivity under pressure was performed up to 15 GPa in EuIrGe<sub>3</sub>. The magnetic ordering temperatures show monotonous increases as function of pressure, though no pressure induced superconductivity was observed till 15 GPa. A pressure-temperature phase diagram of EuIrGe<sub>3</sub> up to 15 GPa is proposed.

# Sažetak

U disertaciji su predstavljeni rezultati evolucije elektronske i kristalne strukture necentrosimetričnih  $\text{EuTGe}_3$  ( $T = \text{Co, Rh i Ir}$ ) sustava pod hidrostatskim tlakom.

Ključne riječi: Visoki tlak, Jako korelirani elektronski sustavi, Eu valencija, Srednja valencija, Necentrosimetrična kristalna struktura.

Od otkrića prvog teškofermionskog supravodiča  $\text{CeCu}_2\text{Si}_2$ , otkriveno je više od 30 sustava koji pokazuju nekonvencionalnu  $f$ -elektronsku supravodljivost. Većina njih pripada spojevima Ce i U, a njihovi fazni dijagrami često se diskutiraju u okviru Doniachovog modela. Osnovno stanje karakterizirano je natjecanjem Kondo efekta i Ruderman-Kittel-Kasuya-Yosida (RKKY) interakcije. Obje interakcije proizlaze iz interakcije lokaliziranih  $f$ -elektrona s metalničnim elektronima. Kondo efekt zasjenjuje magnetske momente, dok RKKY interakcija stabilizira magnetsko uređenje. Supravodljivost se obično pojavljuje blizu magnetske kvantne kritične točke (QCP). Nedavno je otkrivena tlakom inducirana supravodljivost u teškofermionskom sustavu  $\text{CeTX}_3$  ( $T = \text{Co, Rh, Ir; X = Si, Ge}$ ) s  $\text{BaNiSn}_3$ -tipom (I4mm) strukture koja ne posjeduje inverzijsku simetriju. Ovi sustavi su privukli veliku pažnju zbog moguće koegzistencije spin-singletnih i -tripletnih Cooperovih kanala iniciranih antisimetričnom spin-orbit interakcijom, kao i jakim korelacijama.

Nedavno je otkriven i niz Eu spojeva  $\text{EuTX}_3$  s  $\text{BaNiSn}_3$ -tipom strukture. Iako kod njih nije zabilježena pojava tlakom inducirane supravodljivosti, njihove složene magnetske strukture vrlo su zanimljive znanstvenoj zajednici. Serija germanida  $\text{EuTGe}_3$  pokazuje antiferromagnetsko uređenje ispod  $\sim 16$  K, a smjer uređenja momenata varira ovisno o prijelaznom metalu. U  $\text{EuRhGe}_3$  AFM uređenje se uspostavlja na  $T_N = 11,3$  K, a Eu momenti su orijentirani u  $ab$  ravnini, dok su u  $\text{EuCoGe}_3$  i  $\text{EuIrGe}_3$  orijentirani duž  $c$ -osi, s  $T_N = 15,4$  K, odnosno 12,3 K. Ispod  $T_N$ , u  $\text{EuIrGe}_3$  su zabilježeni sukcesivni magnetski prijelazi na  $T_{N'} = 7,5$  K i  $T_{N^*} = 5,0$  K, a u  $\text{EuCoGe}_3$  na  $T_{N'} = 13,4$  K. U usporedbi s germanidima, silicidi čine manju skupinu spojeva. Među njima je nedavno otkriven antiferromagnetski  $\text{EuRhSi}_3$  s atipičnim ponašanjem pod tlakom, koje se ne može objasniti konvencionalnim faznim dijagramom Eu spojeva.

U Eu spojevima, Eu ioni teže biti u  $2+$  stanju ( $4f^7$ ,  $J=7/2$ ) i formirati antiferromagnetsko

osnovno stanje. Međutim, energetska razlika između magnetskog  $\text{Eu}^{2+}$  i nemagnetskog  $\text{Eu}^{3+}$  ( $4f^6$ ,  $J=0$ ) stanja nije velika i podložna je promjeni pod utjecajem vanjskog tlaka ili kemijske supstitucije. Među Eu spojevima, najintenzivnije proučavana serija je  $\text{EuT}_2\text{X}_2$  ( $T$ : prijelazni metal,  $X$  = element 14./15. grupe u periodnom sustavu) s  $\text{ThCr}_2\text{Si}_2$ -tipom ( $I4/mmm$ ) strukture. Općenito, njihov fazni dijagram u ovisnosti o tlaku i temperaturi pokazuje fazni prijelaz prvog reda popraćen promjenom Eu valencije i kolapsom antiferromagnetskog uređenja. Nadalje, postoji korelacija između Eu valencije i volumena jedinične ćelije u vidu kolapsa volumena kristalne rešetke istodobno s promjenom Eu valencije, jer je veličina  $\text{Eu}^{3+}$  iona oko 10% manja od  $\text{Eu}^{2+}$  iona.

Iako je  $\text{BaNiSn}_3$ -tip strukture vrlo blizak  $\text{ThCr}_2\text{Si}_2$ -tipu strukture, fazni dijagram u ovisnosti o tlaku i temperaturi  $\text{EuTX}_3$  serije i odnos između Eu valencije i volumena jedinične ćelije nisu dobro proučeni. Nekoliko ranijih studija pokazalo je stabilno antiferromagnetsko osnovno stanje u  $\text{EuTX}_3$  čak i pod visokim hidrostatskim tlakom od  $\sim 10$  GPa, za razliku od Eu spojeva s  $\text{ThCr}_2\text{Si}_2$ -tipom strukture (Eu122 sustavi) koji obično pokazuju fazne prijelaze pod tlakom od nekoliko GPa. Štoviše, kao što je ranije spomenuto,  $\text{EuRhSi}_3$  pokazuje atipično ponašanje pod tlakom gdje  $T_N$  doseže maksimum na 5-7 GPa i nakon toga se smanjuje s povećanjem tlaka na način kompatibilan s Doniachovim faznim dijagramom. Ovi rezultati sugeriraju jasnu distinkciju karaktera  $\text{EuTX}_3$  sustava od Eu122 sustava. Stoga su u ovoj disertaciji proučavane tlakom uzrokovane promjene strukture  $\text{EuTGe}_3$  serije i njihova korelacija s evolucijom Eu valencije. U tu svrhu je korišteno više eksperimentalnih tehnika. Eu valencija pruža komplementarne informacije za razumijevanje magnetskih svojstava kao i faznog dijagrama ovih spojeva pod tlakom.

Disertacija predstavlja studiju evolucije elektronske i kristalne strukture necentrosimetričnih  $\text{EuTGe}_3$  ( $T = \text{Co}, \text{Rh} \ \& \ \text{Ir}$ ) sustava pod hidrostatskim tlakom. Istraživanje obuhvaća eksperimente rendgenske apsorpcijske spektroskopije s visokom energetsom razlučivosti (HERFD XAS) na  $\text{EuTGe}_3$  sustavu pod visokim hidrostatskim tlakom. Nije uočen prijelaz Eu valencije induciran tlakom ni u jednom od tri spoja. U slučaju  $\text{EuCoGe}_3$ , dobivena Eu valencija se mijenja s 2,2 na 2,3 u rasponu tlaka od 2 do 50 GPa. XAS spektri snimljeni na Ge  $K$  i Co  $K$  rubu kao funkcija tlaka nisu pokazali značajne promjene. To ukazuje da je promjena Eu valencije pod tlakom rezultat intra-atomskog prijenosa naboja iz Eu  $4f$  u  $5d$  stanja, bez doprinosa Ge i Co iona. HERFD XAS spektri pod tlakom na Eu  $L_3$  rubu za  $\text{EuRhGe}_3$  pokazuju promjenu valencije Eu s 2,1 na 2,4 oko 40 GPa. Slično, HERFD XAS spektri pod tlakom na Eu  $L_3$  rubu za  $\text{EuIrGe}_3$  pokazali su promjenu valencije Eu s 2,1 na 2,43 oko 50 GPa. XAS u transmisijskom modu na Eu  $L_3$  rubu za  $\text{EuIrGe}_3$  kao funkcija tlaka također su snimljeni na 300 K i 4 K do 50 GPa, što pokazuje sličnu evoluciju valencije Eu kao HERFD XAS. XAS spektri snimljeni na Ge

$K$  rubu kod  $\text{EuIrGe}_3$  otkrivaju pomak spektralnog intenziteta s povećanjem tlaka. Konkretno,  $\text{Ge } K$  XAS spektri pokazuju pomak apsorpcijskog vrha sa 11102 eV, povezanog s Ge ionima na Wyckoff 4b poziciji, na 11108 eV, povezanog s Ge ionima na Wyckoff 2a poziciji. Apсорpcijski vrh na  $\text{Ir } L_3$  rubu pomiče se prema višoj energiji s povećanjem tlaka. Ovi rezultati sugeriraju mogući učinak međuatomskog prijenosa naboja u evoluciji Eu valencije u  $\text{EuIrGe}_3$ .

Pri atmosferskom tlaku, sva tri spoja pokazuju srednju Eu valenciju blizu 2,1, a najveća promjena srednje Eu valencije s tlakom zabilježena je za  $\text{EuIrGe}_3$ , dok je najmanja promjena zabilježena za  $\text{EuCoGe}_3$ .

Za proučavanje korelacije između evolucije elektronske strukture i kristalne strukture pod tlakom, provedeno je istraživanje rendgenske difrakcije na prahu pod tlakom na  $\text{EuTGe}_3$ . Nije zabilježen strukturni prijelaz induciran tlakom ni u jednom od tri spoja do 40 GPa. Uočena je anizotropna promjena  $a$  i  $c$  parametara kristalne rešetke, pri čemu je parametar  $a$  kristalne rešetke pokazao veće promjene odnosu na parametar  $c$ . Ovo ponašanje pod tlakom suprotno je onome kod centrosimetričnih Eu-122 sustava. U Eu-122 sustavima, parametar  $c$  kristalne rešetke je više komprimiran pod tlakom nego parametar  $a$ . Aksijalni omjer ( $c/a$ ) pokazuje trend linearnog povećanja s porastom tlaka te promjenu nagiba pri određenom tlaku kod sva tri spoja. Nije pronađena izravna korelacija između volumena jedinične ćelije i Eu valencije u necentrosimetričnim  $\text{EuTGe}_3$  sustavima, što je također u suprotnosti s ponašanjem zabilježenim u Eu-122 sustavima.

Kako bi se istražilo potencijalno postojanje supravodljivosti inducirano tlakom, izmjeren je električni otpor u  $\text{EuIrGe}_3$  pod hidrostatskim tlakom do 15 GPa. Temperature magnetskog uređenja pokazuju monoton porast u funkciji tlaka kod svih spojeva, iako supravodljivost inducirana tlakom nije uočena do 15 GPa. Predložen je fazni dijagram u ovisnosti o tlaku i temperaturi za  $\text{EuIrGe}_3$  do 15 GPa.

# Contents

<b>1</b>	<b>Introduction</b>	<b>1</b>
1.1	4 <i>f</i> electron system . . . . .	1
1.2	Kondo effect . . . . .	2
1.3	RKKY interaction . . . . .	3
1.4	Doniach phase diagram . . . . .	4
1.5	Valence fluctuation . . . . .	5
1.6	Europium compounds . . . . .	5
1.6.1	EuT <sub>2</sub> X <sub>2</sub> (Eu-122) . . . . .	7
1.6.2	EuTX <sub>3</sub> (Eu -113) . . . . .	8
1.7	Aims of Research . . . . .	10
1.8	Thesis outline . . . . .	11
<b>2</b>	<b>Experimental</b>	<b>13</b>
2.1	Working Principle of DAC . . . . .	14
2.1.1	Gasket and pressure transmitting mediums . . . . .	14
2.2	Pressure calibration methods . . . . .	15
2.2.1	Ruby fluorescence pressure gauge . . . . .	16
2.2.2	Gold equation of state . . . . .	17
2.2.3	Lead (Pb) superconducting transition temperature . . . . .	18
2.3	Electric resistivity under pressure . . . . .	19
2.3.1	DAC Design . . . . .	20
2.3.2	Gasket material selection . . . . .	20
2.3.3	Preparation . . . . .	22
2.3.4	Sample loading in DAC . . . . .	22
2.3.5	Measurement setup and conditions . . . . .	23
2.4	X-ray absorption spectroscopy under pressure . . . . .	23
2.4.1	Principle of HERFD XAS . . . . .	24
2.4.2	Experimental conditions of HERFD XAS under pressure . . . . .	26
2.4.3	Transmission mode XAS . . . . .	27
2.5	X-ray diffraction under pressure . . . . .	28
2.5.1	Principles of X-ray Diffraction . . . . .	29
2.5.2	Experimental conditions of XRD under pressure . . . . .	30

<b>3</b>	<b>Results</b>	<b>31</b>
3.1	X-ray absorption spectroscopy under pressure . . . . .	31
3.1.1	EuCoGe <sub>3</sub> . . . . .	32
3.1.2	EuRhGe <sub>3</sub> . . . . .	35
3.1.3	EuIrGe <sub>3</sub> . . . . .	36
3.1.4	Comparison of three compounds . . . . .	41
3.2	X-ray diffraction under pressure . . . . .	41
3.2.1	EuCoGe <sub>3</sub> . . . . .	43
3.2.2	EuRhGe <sub>3</sub> . . . . .	46
3.2.3	EuIrGe <sub>3</sub> . . . . .	49
3.2.4	Comparison of XRD under pressure . . . . .	52
3.3	Electric resistivity under pressure of EuIrGe <sub>3</sub> . . . . .	53
<b>4</b>	<b>Thesis summary and outlook</b>	<b>58</b>
4.1	Summary of this Thesis . . . . .	58
4.1.1	Pressure evolution of the electronic structure . . . . .	58
4.1.2	Pressure evolution of crystal structure . . . . .	59
4.1.3	Electric resistivity under pressure . . . . .	60
<b>A</b>	<b>Hydrostatic or quasi-hydrostatic pressure</b>	<b>62</b>
A.0.1	Ruby fluorescence spectra fitting . . . . .	63
<b>B</b>	<b>DFT calculations and technical details of pressure cell</b>	<b>65</b>
B.0.1	DFT calculation . . . . .	65
B.0.2	Technical details of pressure cell . . . . .	65
<b>C</b>	<b>Additional X-ray diffraction results</b>	<b>70</b>
C.0.1	Synchrotron vs lab XRD under pressure . . . . .	70
C.0.2	EOS fitting of pressure transmitting medium neon . . . . .	70
C.0.3	Different EOS fitting and quality of EOS Fit . . . . .	72
C.0.4	Powder XRD data processing . . . . .	73
C.0.5	EuIrGe <sub>3</sub> single crystal XRD under pressure . . . . .	73
C.0.6	EuRhGe <sub>3</sub> XRD under pressure with neon PTM . . . . .	74
C.0.7	XRD and DFT extracted atomic coordinates as function of pressure of EuTGe <sub>3</sub> compounds . . . . .	76
	<b>References</b>	<b>79</b>
	<b>Curriculum vitae</b>	<b>83</b>

# List of Figures

1.1	Kmetko smith diagram . . . . .	2
1.2	Doniach phase diagram . . . . .	4
1.3	Crystal structure . . . . .	6
1.4	Phase diagram for Ce/Yb and Eu compounds. . . . .	7
1.5	V-T Phase diagram for $\text{EuT}_2\text{X}_2$ . . . . .	8
1.6	Electric resistivity for $\text{EuTGe}_3$ compounds. . . . .	9
1.7	Magnetic susceptibility for $\text{EuTGe}_3$ . . . . .	9
1.8	$\text{EuTGe}_3$ electric resistivity under pressure. . . . .	11
2.1	Working principle of DAC. . . . .	14
2.2	Ruby fluorescence for pressure calibration. . . . .	16
2.3	Gold EOS for pressure calibration. . . . .	17
2.4	Lead Tc for Pressure calibration . . . . .	19
2.5	DAC design for electric resistivity. . . . .	20
2.6	SS304L stainless steel gasket testing. . . . .	21
2.7	MP35N stainless steel gasket testing. . . . .	21
2.8	Various steps of electric resistivity under pressure. . . . .	23
2.9	Schematic of transport under pressure. . . . .	24
2.10	Schematic for HERFD XAS. . . . .	25
2.11	Experimental layout of HERFD XAS. . . . .	26
2.12	Experimental setup for XRD and XAS under pressure. . . . .	28
2.13	Schematic representation of XRD. . . . .	29
3.1	$\text{EuCoGe}_3$ HERFD XAS under pressure. . . . .	32
3.2	$\text{EuCoGe}_3$ Eu L3 XAS fitting. . . . .	33
3.3	HERFD XAS along Ge and Co edge . . . . .	34
3.4	XES along Ge and Co edge. . . . .	34
3.5	$\text{EuRhGe}_3$ HERFD under pressure. . . . .	35
3.6	Eu L3 XAS fitting for $\text{EuRhGe}_3$ . . . . .	36
3.7	Eu L3 HERFD of $\text{EuIrGe}_3$ . . . . .	37
3.8	Eu L3 XAS fitting of $\text{EuIrGe}_3$ . . . . .	38
3.9	Ge K XAS $\text{EuIrGe}_3$ . . . . .	39
3.10	Ir L3 XAS $\text{EuIrGe}_3$ . . . . .	40
3.11	Mean Eu valence as function of pressure. . . . .	41

3.12	EuCoGe <sub>3</sub> XRD contour map . . . . .	43
3.13	Rietveld refinement fitting of EuCoGe <sub>3</sub> and EuRhGe <sub>3</sub> . . . . .	44
3.14	EuCoGe <sub>3</sub> anisotropy and EOS fitting . . . . .	45
3.15	EuCoGe <sub>3</sub> axial ratio as function of pressure. . . . .	46
3.16	EuRhGe <sub>3</sub> XRD contour map. . . . .	47
3.17	EOS fitting and anisotropy of EuRhGe <sub>3</sub> . . . . .	48
3.18	EuRhGe <sub>3</sub> axial ratio as function of pressure. . . . .	49
3.19	XRD contour map of EuIrGe <sub>3</sub> . . . . .	50
3.20	Rietveld refinement fitting for EuIrGe <sub>3</sub> . . . . .	51
3.21	EuIrGe <sub>3</sub> unit cell volume by SC/PXRD . . . . .	52
3.22	Anisotropic compressibility in EuTGe <sub>3</sub> system. . . . .	54
3.23	EuIrGe <sub>3</sub> electric resistivity at ambient pressure. . . . .	55
3.24	EuIrGe <sub>3</sub> electric resistivity under pressure. . . . .	56
3.25	EuIrGe <sub>3</sub> TN as function of pressure. . . . .	57
4.1	Pressure evolution of mean Eu valence of EuTGe <sub>3</sub> . . . . .	59
4.2	EuTGe <sub>3</sub> crystal structure under pressure. . . . .	60
4.3	P-T phase diagram of EuIrGe <sub>3</sub> . . . . .	61
A.1	Hydrostatic and non-hydrostatic pressure by ruby fluorescence. . . . .	63
A.2	Ruby fluorescence fitting. . . . .	64
B.1	DOS of EuTGe <sub>3</sub> under pressure. . . . .	66
B.2	Dioplas for XRD image processing cont. . . . .	67
B.3	Piston cylinder cell. . . . .	67
B.4	Gasket material testing. . . . .	68
C.1	Lab vs synchrotron XRD. . . . .	71
C.2	EOS fitting for neon under pressure. . . . .	71
C.3	Quality assessment of EOS fitting . . . . .	72
C.4	Dioplas for XRD image processing. . . . .	73
C.5	Dioplas for XRD image processing cont. . . . .	74
C.6	EuRhGe <sub>3</sub> XRD under pressure with neon PTM . . . . .	75
C.7	Anisotropic compressibility in EuRhGe <sub>3</sub> XRD with neon PTM . . . . .	75

# List of Tables

2.1	Experimental conditions for XAS, XRD and electric resistivity under pressure.	15
2.2	Analyzers, emission energies and Bragg angles for HERFD XAS under pressure.	27
3.1	XRD and DFT calculated lattice parameters of $\text{EuCoGe}_3$ .	46
3.2	XRD and DFT calculated lattice parameters of $\text{EuRhGe}_3$ .	48
3.3	XRD and DFT calculated lattice parameters of $\text{EuIrGe}_3$ .	50
3.4	Bulk modulus and its first pressure derivative of $\text{EuTGe}_3$ .	53
A.1	Ruby fluorescence spectra fitting by various methods.	64
B.1	Various gasket materials and their indentation thickness dependence on loads and diamond culet size.	68
C.1	Comparison between different EOS fitting methods for $\text{EuTGe}_3$ unit cell volume.	72
C.2	Single crystal XRD under pressure of $\text{EuIrGe}_3$ .	74
C.3	Atomic coordinates for $\text{EuCoGe}_3$ under pressure extracted from refinement of XRD data and DFT calculation.	76
C.4	Atomic coordinates for $\text{EuRhGe}_3$ under pressure extracted from refinement of XRD data and DFT calculation.	77
C.5	Atomic coordinates for $\text{EuIrGe}_3$ under pressure extracted from refinement of XRD data and DFT calculation.	78

# Chapter 1

## Introduction

Strongly correlated electron systems are materials where the interactions between electrons are so strong that conventional methods, like band theory, cannot accurately describe their properties. In these systems, electronic correlations are crucial in determining their behavior. Examples include high-temperature superconductors, Mott insulators, and heavy fermion materials. These materials often exhibit intriguing phenomena such as unconventional superconductivity, metal-insulator transitions, valence fluctuation, and exotic magnetic ordering, making them of great interest in both fundamental research and technological applications, such as high- $T_c$  superconductors [1] and magnetic storage devices [2]. With advancements in high-pressure techniques, there has been a significant increase in attention toward controlling and understanding the behavior of strongly correlated electron systems under high pressure over the past few decades.

### 1.1 $4f$ electron system

The  $4f$  electron system refers to a group of materials that contains lanthanide elements with partially filled  $4f$  orbitals which plays crucial role in their properties. The highly localized  $4f$  electrons lead to strong Coulomb interactions, and their ground state tends to obey Hund's rules due to relatively small crystalline electric field (CEF) [3]. The  $4f$  electron system shows a range of interesting physical phenomena, such as unconventional  $f$ -electron superconductivity [4; 5], and valence fluctuations [6]. It is generally believed that all these features largely originate in the strongly correlated  $4f$  electrons, and the materials containing such  $4f$  electrons manifest Janus-faced behavior (localized or itinerant) depending on the surrounding environment. As an example, the well-investigated  $\alpha - \gamma$  transition in Ce is considered a Mott transition, where the  $4f$  electron changes its behavior from being localized to becoming itinerant [7].

Many new phenomena occurs when magnetic ions are placed inside a metallic host. However, magnetic states can only survive when local Coulomb interactions suppress charge fluctuations, i.e., when valence electrons are localized. Fig 1.1 illustrates the Kmetko-Smith diagram, organizing the  $d$  and  $f$  elements of the periodic table according to the localization of the valence shell. This arrangement is particularly useful as it also correlates with the energy scaling of crucial interactions in correlated materials: the Coulomb interaction, which increases with increasing localization, the strength of the CEF, which decreases with increasing localization, and the spin-orbit coupling (SOC), which strongly increases with the principal quantum number ( $n$ ) and further with the atomic number ( $Z$ ). The increasing localization from the bottom left to the top right is accompanied by a crossover from itinerant electrons to localized magnetic moments, and particularly interesting phenomena occur in this crossover regime.

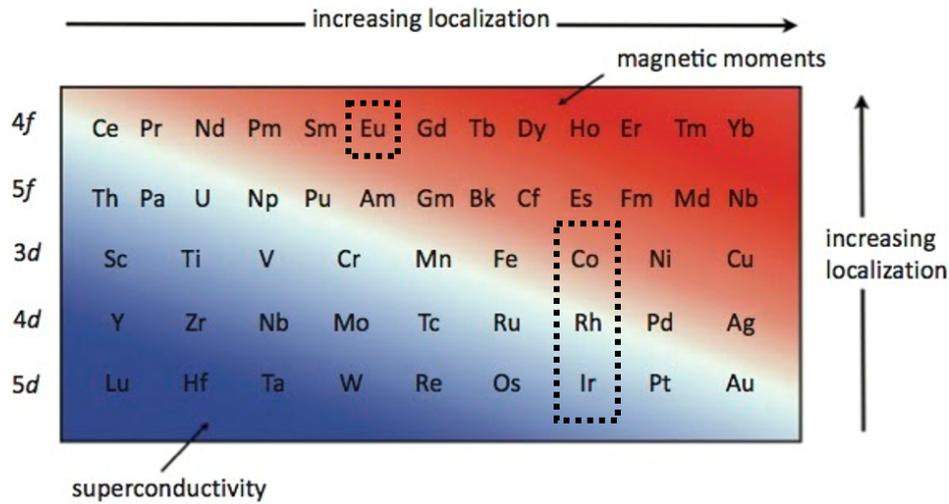


Figure 1.1: Kmetko-Smith diagram adapted from Ref.[8]. It shows a rearrangement of the  $d$  and  $f$  elements of the periodic table to visualize the trend of increasing localization in these ions, i.e.  $5d < 4d < 3d < 5f < 4f$ . The main elements that are involved in the thesis discussion, Eu, Co, Rh and Ir, are marked with boxes.

## 1.2 Kondo effect

The Kondo effect was first discovered as an anomalous temperature behavior of the electric resistance in dirty Au wires [9], and later also observed in other metals with dilute magnetic impurities [10]. The electric resistance of ordinary metals decreases with lowering temperature and reaches to a constant residual resistance near 0 K. However, the electric resistance of these dirty metals takes a minimum at a certain temperature and then increases at low temperatures.

The behavior remained a puzzle until Jun Kondo described it based on the  $s-d$  exchange model. The magnetic moment of the impurity behaves as a scattering center for conduction electrons. When the scattering probability of the conduction electrons is calculated to the second Born approximation, the intermediate states of the spin-flip scattering are affected by the Fermi sphere and give  $\propto JN(0)\log(D_0/k_B T)$  term in the electric resistivity. Here  $J$  denotes the magnitude of antiferromagnetic exchange interaction between localized (impurity) and conduction electrons, and  $N(0)$  and  $D_0$  represent the density of state at the Fermi energy ( $E_F$ ) and the conduction band width, respectively. Below the characteristic temperature, so-called Kondo temperature ( $T_K$ ),  $k_B T_K = D_0 \exp(-1/JN(0))$ , perturbation theory breaks down and the resistivity diverges for  $T \rightarrow 0$  K. Later, this problem was solved using self-consistent method by Nagaoka [11] and based on the singlet ground state for a localized spin using the  $s-d$  exchange model by Yosida [12]. With a lowering temperature below  $T_K$ , the localized electrons (impurity) start to couple antiferromagnetically with spin-polarized conduction electrons and screen the localized moments. This bound state is called the Kondo singlet.

### 1.3 RKKY interaction

Although the Ruderman-Kittel-Kasuya-Yosida (RKKY) interaction also originates from the interaction between localized (impurity) and conduction electrons as well the Kondo effect, it works as opposite to the Kondo effect and stabilizes the magnetically ordered ground state. A localized moment (impurity moment) induces spin polarizations among the conduction electrons. Assuming the conduction electrons maintain mobility, they traverse the lattice with spin density oscillating similarly to Friedel oscillations observed in the charge channel. In a dense system, this spin density interacts with other impurities, thereby giving rise to the RKKY exchange interaction

$$H_{RKKY} = \frac{2\alpha J^2 S_i S_j \cos(2k_F r_{ij} + \phi)}{r_{ij}^3}.$$

Here  $S_i$  and  $S_j$  represent the localized spin states at  $i$  and  $j$  sites with  $r_{ij}$  distance and  $\phi$  phase shift. The prefactor  $\alpha$  and the Fermi wave vector ( $k_F$ ) depend greatly on the electronic structure of the system. The two effects, the RKKY interaction favoring a magnetically ordered ground state and the Kondo effect favoring a non-magnetic singlet state, compete with each other. This is pictured by the so-called Doniach phase diagram [13].

## 1.4 Doniach phase diagram

The interplay between the RKKY interaction and the Kondo effect is expected to be the driving force for the emergence of many phenomena in strongly correlated  $4f$  electron systems. The Doniach phase diagram (Fig.1.2) phenomenologically describes the competition between the Kondo effect and the RKKY interaction as a function of the  $JN(0)$ .  $JN(0)$  can be controlled by applying a magnetic field, changing the chemical composition or external pressure. Doniach argued that there are two scales in the Kondo lattice, the single-ion Kondo temperature  $T_K$  and  $T_{\text{RKKY}}$ , given by  $T_K = D_0 e^{-\frac{1}{2N(0)J}}$ ,  $T_{\text{RKKY}} = J^2 N(0)$ . When  $JN(0)$  is small, then  $T_{\text{RKKY}}$  is the largest scale and an antiferromagnetic state is formed, but, when the  $JN(0)$  is large, the Kondo temperature is the largest scale so a dense Kondo lattice ground state becomes stable.

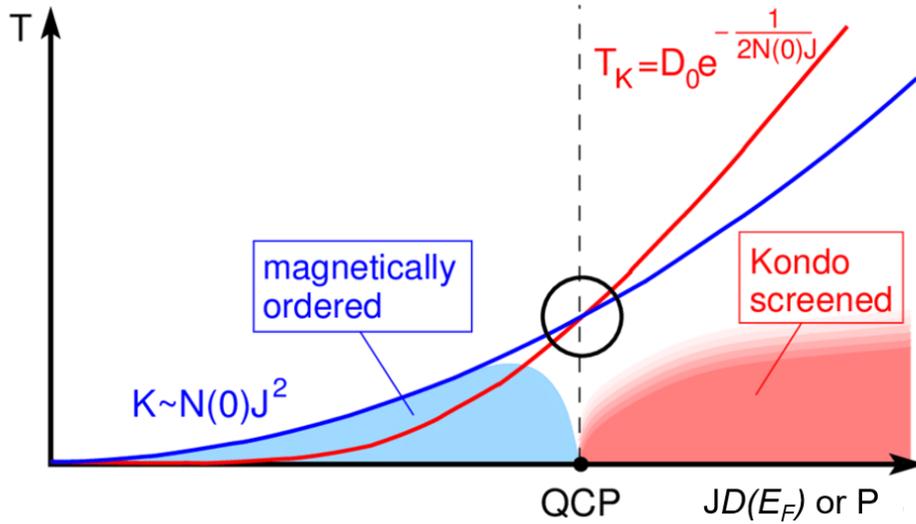


Figure 1.2: Doniach's phenomenological phase diagram for the phase transition between an RKKY-induced, magnetically ordered phase and the Kondo-screened, paramagnetic phase. The phase transition occurs when the RKKY coupling  $K$  of a local moment to all surrounding moments becomes equal to the Kondo singlet binding energy  $T_K$  (black circle). While the RKKY coupling is  $K \sim N(0)J_0^2$ , the Kondo energy  $T_K = D_0 \exp[-1/(2N(0)J_0)]$  is exponentially small in the bare, local spin exchange coupling  $J$ . Therefore, the RKKY coupling always dominates for small values of  $J_0$ . Adapted from Ref. [14].

When an external pressure (P) is applied on an antiferromagnetically ordered cerium-based compound, the Néel temperature ( $T_N$ ) increases with increasing pressure, and starts to decrease after threshold pressure. When higher pressure is applied,  $T_N$  starts to decrease slowly and then reaches zero at a critical pressure ( $P_c$ ). Namely, a quantum critical point (QCP) is experimentally defined as an electronic state where  $T_N \rightarrow 0$  for  $P \rightarrow P_c$ . In the potential quantum critical region, the heavy fermion state is formed at high pressures, and unconventional superconduc-

tivity, presumably caused by magnetic fluctuations, often appears at very low temperatures as observed in CeIn<sub>3</sub> and CePd<sub>2</sub>Si<sub>2</sub> [15].

Recently, heavy-fermionic superconductors have been discovered among compounds whose crystal structures do not possess inversion symmetry, (see Fig. 1.3). They have attracted much attention due to the possible coexistence of spin-singlet and -triplet Cooper channels initiated by antisymmetric spin-orbit interaction as well as strong correlations [16; 17]. Except for the previously discovered first non-centrosymmetric superconductor CePt<sub>3</sub>Si [18], the superconductivity in non-centrosymmetric compounds tends to emerge under pressure as observed in CeTX<sub>3</sub> ( $T = \text{Co, Rh, Ir}$ ;  $X = \text{Si, Ge}$ ) series [18; 19; 20; 21].

## 1.5 Valence fluctuation

Apart from pressure-induced superconductivity in  $4f$  electron systems, pressure-induced valence fluctuation has gained a lot of attention for decades. The most studied examples of valence fluctuations or instability of  $4f$  shell with pressure are Ce [22], Sm [23] and Tm [24] based monochalogenides.

Valence fluctuation is also defined as interconfiguration interaction, where the energy of two states is nearly degenerate, and electrons fluctuate between these states. Valence fluctuation is categorized into two parts: inhomogeneous and homogeneous valence fluctuation. In inhomogeneous valence fluctuation, atoms with differing static valence reside on different crystallographic sites, while in homogeneous valence fluctuation, the same non-integral valence is found on each atomic site. Inhomogeneous valence fluctuation compounds are referred to **mixed valence compounds** [25]; on the other hand, homogeneous valence fluctuation compounds are termed **intermediate valence compounds**. Rare-earth ( $4f$  electrons) are known to have more than one valence state. Valence fluctuation often occurs in lanthanide compounds in which the proximity of the  $4f$  level to the Fermi energy leads to instabilities of the charge configuration (valence) and/or of the magnetic moment.

## 1.6 Europium compounds

Most of the Eu-based compounds are, however, different from the other lanthanide compounds. Namely, the lanthanide ions are usually trivalent, though a divalent ( $\text{Eu}^{2+}$ ,  $4f^7$ ) electronic state is more favored than a trivalent ( $\text{Eu}^{3+}$ ,  $4f^6$ ) one in the Eu-based compounds. A large deviation from the linear interpolation of lattice parameters for the other rare-earth compounds with the same composition is an indication of the divalence of the Eu ion [27]. When an external pressure

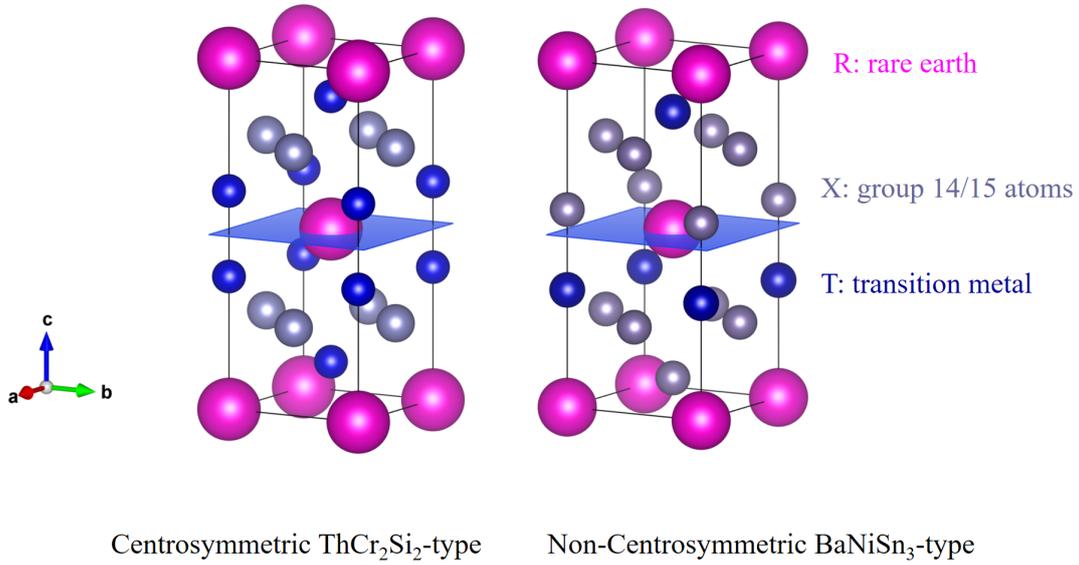


Figure 1.3:  $\text{ThCr}_2\text{Si}_2$ -type centrosymmetric  $\text{RT}_2\text{X}_2$  and  $\text{BaNiSn}_3$  type non-centro symmetric  $\text{RTX}_3$  crystal structures. The central plane is illustrated to demonstrate its non-centrosymmetry. These structures were visualized by using VESTA [26].

is applied, Ce compounds show second order phase transition from antiferromagnetic to non-magnetic ground state where  $T_N$  slowly decreases as function of pressure and reaches 0 K at the QCP as described in Fig.1.4 (a). However much different phase diagram was observed in case of Eu-compounds. In most of the reported Eu-compounds, Eu-ions favour a  $\text{Eu}^{2+}$  ( $J=7/2$ ) at ambient pressure with an antiferromagnetic ground state. When an external pressure is applied on Eu-compounds, the magnetic ordering temperature  $T_N$  increases as function of pressure up to threshold pressure and a sudden first order transition to non-magnetic  $\text{Eu}^{3+}$  was observed, as presented in Fig. 1.4.

Magnetic properties of Eu-compounds strongly depend on the Eu valence state. There are not many but some Eu-compounds with nonmagnetic  $\text{Eu}^{3+}$  ( $J=0$ ) at ambient pressure exist and exhibit the Van Vleck susceptibility, such as  $\text{EuCo}_2\text{Si}_2$  [30] and  $\text{EuPd}_3$  [31]. Since, the energy difference between  $\text{Eu}^{2+}$  and the nonmagnetic  $\text{Eu}^{3+}$  is not so large  $\sim 0.07$  eV in  $\text{EuCu}_2\text{Si}_2$  [32], Eu valence transitions controlled by temperature, external pressure, and chemical substitution have been reported in Eu-compounds. Since  $\text{Eu}^{3+}$  ionic radius is smaller than  $\text{Eu}^{2+}$  ions, the valence transition from  $\text{Eu}^{2+}$  to  $\text{Eu}^{3+}$  is stated as volume collapse model.

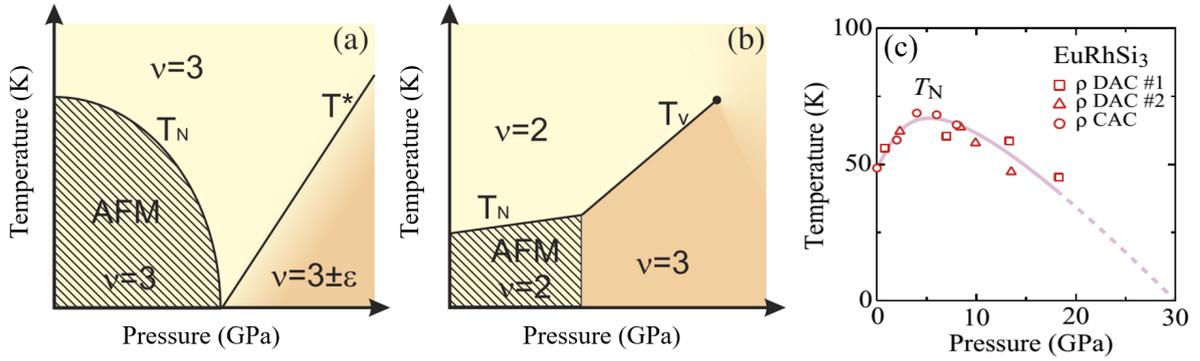


Figure 1.4: Typical phase diagram of (a) Ce compounds and (b) Eu compounds, adapted from Ref [28]. Here  $v = 2$  represents the divalent state,  $v = 3$  represents the trivalent state,  $T_N$  represents the Néel temperature,  $T_V$  is the valence transition temperature, and  $T^*$  is the coherence temperature. (c) An atypical pressure change of  $T_N$  reported in  $\text{EuRhSi}_3$  [29].

### 1.6.1 $\text{EuT}_2\text{X}_2$ (Eu-122)

Among ternary Eu-compounds,  $\text{EuT}_2\text{X}_2$  ( $T$ : transition metal,  $X =$  group 14/15 in periodic table) series with the  $\text{ThCr}_2\text{Si}_2$ -type structure (Eu-122 systems) has a wide variety and is most intensively studied. The crystal structure of Eu122 systems is built up with identical  $[\text{T}_2\text{X}_2]^{2-}$  layers separated by  $\text{A}^{2+}$  ions. Eu sits on 2a Wyckoff position with coordinates (0, 0, 0), T occupies the 4d position with coordinates (1/2, 0, 1/4), and X occupies the 4e position with coordinates (0, 0, z).

Many of Eu-122 systems possess  $\text{Eu}^{2+}$  ions and exhibit antiferromagnetic ordering at low temperature. Among them, pressure and temperature induced valence transitions from  $\text{Eu}^{2+}$  to  $\text{Eu}^{3+}$  were reported, for example in  $\text{EuRh}_2\text{Si}_2$  ( $\sim 2$  GPa at 170 K) [34], and  $\text{EuCo}_2\text{Ge}_2$  ( $\sim 3$  GPa at 50 K) [35]. The valence transition is realised at around 5 GPa in  $\text{EuNi}_2\text{Ge}_2$  even at room temperature. When the temperature is cooled down, the valence transition happens at pressure about 2 GPa at 34 K in  $\text{EuNi}_2\text{Ge}_2$  [36]. Applying pressure on such compounds increases  $T_N$ , then a sudden disappearance of magnetic moments and a valence cross-over happens at a critical pressure. These materials show the first order valence transition.

Along with valence transition, pressure-induced first-order/second-order isostructural transitions have been reported in ( $\text{EuT}_2\text{X}_2$ ), such as  $\text{EuCo}_2\text{P}_2$  ( $\sim 3$  GPa),  $\text{EuFe}_2\text{P}_2$  (2-9 GPa) [37],  $\text{EuCo}_2\text{As}_2$  ( $\sim 5$  GPa) [38], and  $\text{EuNi}_2\text{Ge}_2$  ( $\sim 5$  GPa) [39]. The Eu valence in those compounds is almost  $\text{Eu}^{2+}$  at ambient pressure. The lattice parameters abruptly change by applying pressure without changing  $I4/mmm$  symmetry in most cases. Across the isostructural phase transition from tetragonal to the so-called collapsed tetragonal phase, the  $a$ - and  $c$ -lattice parameters

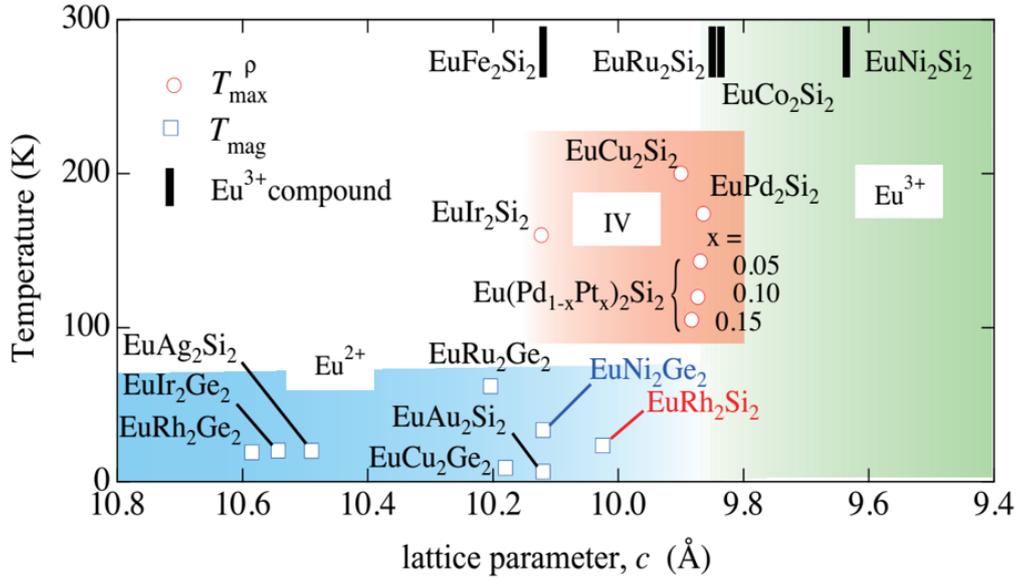


Figure 1.5: Electronic properties of  $\text{EuT}_2\text{X}_2$  with  $\text{ThCr}_2\text{Si}_2$ -type tetragonal structure as a function of the lattice parameter along the  $c$ -axis. Open square indicates magnetic ordering temperature, open circle indicates a temperature where the electrical resistivity shows broad maximum, and black bar indicates the  $c$ -axis lattice parameter of trivalent Eu compounds. Figure taken from [33].

greatly change as well as the unit cell volume and ( $c/a$ ) axial ratio.

In the case of  $\text{EuCo}_2\text{P}_2$ , the  $c$ -lattice parameter decreases by 12.3%, while the  $a$ -lattice parameter increase by 2.8% leading to an extreme collapse of the  $c/a$  ratio (-14.7%) after the first-order isostructural transition [40]. By applying the pressure, the change in the bonding nature of P-P (As-As) along the  $c$  axis is reported in  $\text{EuCo}_2\text{P}_2$  and  $\text{EuCo}_2\text{As}_2$  [37; 38] which contributes to the collapse tetragonal structure. In  $\text{EuT}_2\text{X}_2$  materials, the correlation between Eu valence and unit volume (lattice parameter  $c$ ) are presented in Fig.1.5.

### 1.6.2 $\text{EuTX}_3$ (Eu -113 )

Unlike the Eu-122 systems, much less studies have been reported among Eu-compounds with the  $\text{BaNiSn}_3$ -type structure ( $I4mm$ ), which is closely related to the  $\text{ThCr}_2\text{Si}_2$ -type structure (see Fig.1.3). Recently, a series of europium transition metal silicides/germanides,  $\text{EuTX}_3$  ( $T$ = transition metal,  $X$ =Si or Ge), with the  $\text{BaNiSn}_3$ -type structure were reported. In the crystallographic unit cell of  $\text{EuTX}_3$  systems, Eu atoms occupy the  $2a$  Wyckoff site, silicon/germanium atoms are located at two different Wyckoff positions  $2a$  and  $4b$ , while transition metal atoms occupy the  $2a$  site [41]. Magnetic susceptibility measurements [42; 43; 44] and Mössbauer spectroscopy [45; 46] revealed the presence of magnetic  $\text{Eu}^{2+}$  ions in each of the investigated

compounds. While all of them order antiferromagnetically (AFM) at similar temperatures, the magnetic structure formed by the localized Eu  $4f$  moments depends on the transition metal constituent. For example, in  $\text{EuRhGe}_3$  the AFM order sets in at  $T_N = 11.3$  K and the moments are confined in the  $ab$  plane, while they are aligned along the  $c$ -axis in  $\text{EuCoGe}_3$ ,  $\text{EuNiGe}_3$  and  $\text{EuIrGe}_3$  that order at  $T_N = 15.4, 13.5,$  and  $12.3$  K respectively [41; 42; 43].

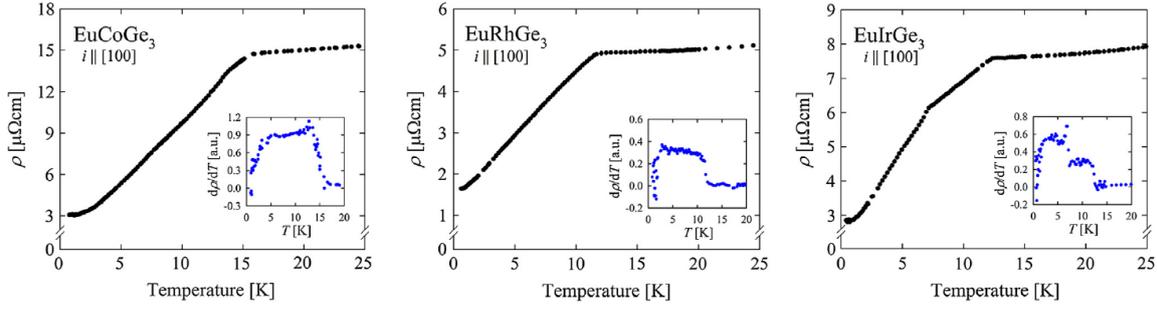


Figure 1.6: Low-temperature variations of the electric resistivity of  $\text{EuTGe}_3$  ( $T=\text{Co, Rh}$  and  $\text{Ir}$ ) single crystals taken from Ref.[41]. The inset shows the temperature derivative of the electric resistivity.

The magnetic ordering temperatures at low temperature in electric resistivity and magnetic susceptibility of  $\text{EuCoGe}_3$ ,  $\text{EuRhGe}_3$  and  $\text{EuIrGe}_3$  are presented in Fig.1.6 and Fig.1.7, respectively. Below  $T_N$ , successive magnetic phase transitions were observed at  $T'_N = 13.4$  K in  $\text{EuCoGe}_3$  and  $T'_N = 7.5$  K and  $T_N^* = 5.0$  K in  $\text{EuIrGe}_3$  [41; 44]. Very recently,  $\text{EuIrGe}_3$  was studied by neutron and resonant x-ray diffraction and complex magnetic phase transitions from an incommensurate longitudinal sinusoidal structure below  $T_N$  to a cycloidal structure below  $T'_N$ , then to a cycloidal structure rotated by  $45^\circ$  in-plane below  $T_N^*$  were revealed [47].

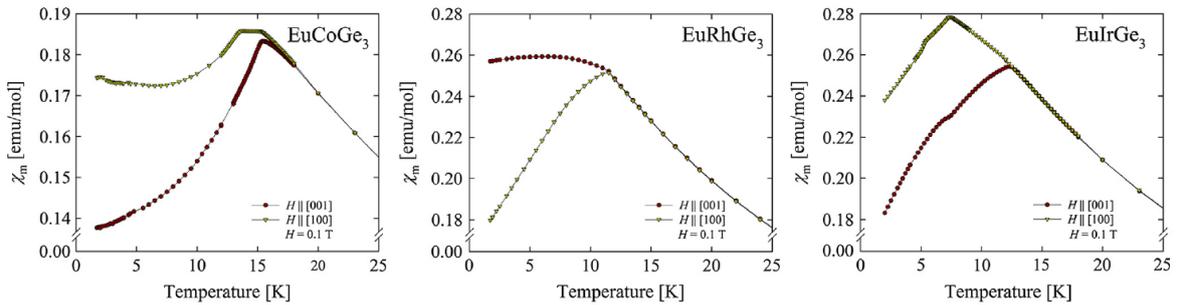


Figure 1.7: Low-temperature variations of the magnetic susceptibility of  $\text{EuTGe}_3$  ( $T=\text{Co, Rh}$  and  $\text{Ir}$ ) single crystals measured with magnetic field applied along and perpendicular to the crystallographic  $c$ -axis taken from Ref.[41].

In contrast with Eu-122 compounds, an atypical pressure response has been reported in  $\text{EuRhSi}_3$  [48; 29].  $\text{EuRhSi}_3$  exhibits antiferromagnetic ground state with almost divalent Eu

ions at ambient pressure. Applying pressure causes an increase of  $T_N$  up to 5–7 GPa, then at higher pressure  $T_N$  smoothly decreases in a similar manner of the Doniach-type phase diagram [48; 29], presented in Fig.1.3 (a). Pressure dependent electric resistivity measurements suggested a continuous change of the Eu valence without a first-order valence transition [29]. This behavior implies a potential presence of the QCP as well as the emergence of superconductivity in its vicinity.

Temperature-dependent electric resistivity measurements under pressure were reported on  $\text{EuCoGe}_3$ ,  $\text{EuNiGe}_3$ ,  $\text{EuRhGe}_3$ , and  $\text{EuIrGe}_3$  up to 8 GPa [49; 44]. The magnetic transition temperatures  $T_N$  and  $T'_N$  were found to increase with increasing pressure and no sign of any other phase transition was observed, as presented in Fig.1.8. Similar results were obtained from pressure-dependent ac calorimetry in  $\text{EuCoGe}_3$  up to 10.4 GPa, which additionally indicated a pressure-driven moderate effective mass enhancement [50]. So far, the emergence of pressure-induced superconductivity in these materials has not been reported. Hence, a much higher pressure is required to investigate a possibility of valence transition or potential pressure induced superconductivity in these compounds.

### **$\text{EuTGe}_3$ crystal synthesis**

Since the thesis concerns electronic and crystal structural studies of  $\text{Eu}(\text{Co}, \text{Rh}, \text{Ir})\text{Ge}_3$ , the synthesis method of those crystals utilized for the experiments is briefly mentioned here. High-quality single crystals of  $\text{EuCoGe}_3$ ,  $\text{EuRhGe}_3$  and  $\text{EuIrGe}_3$  were grown and characterized at the Institute of Low Temperature and Structure Research, Polish Academy of Science, Wroclaw Poland. The crystals were obtained by the metal flux method using liquid indium as solvent. The starting materials in growing  $\text{EuTGe}_3$  ternaries were high purity elements: Eu (99.9 at.%), T metals (99.999 at.%), Ge (99.999 at.%) and indium (purity 99.99 at.%) taken in the ratio of 1:1:3:20 with additional 5% of Eu to compensate possible weight losses due to evaporation and/or contamination by oxides. The syntheses were carried out in small alumina crucibles placed in quartz tubes. More details about crystal synthesis and characterization can be found in Ref. [51].

## **1.7 Aims of Research**

The study aims to reveal the pressure evolutions of Eu valence and crystal structure in  $\text{EuTGe}_3$  and to elucidate the different pressure responses among  $\text{EuTGe}_3$  with 3d, 4d, and 5d transition metal constituents with various experimental techniques. The study will advance the

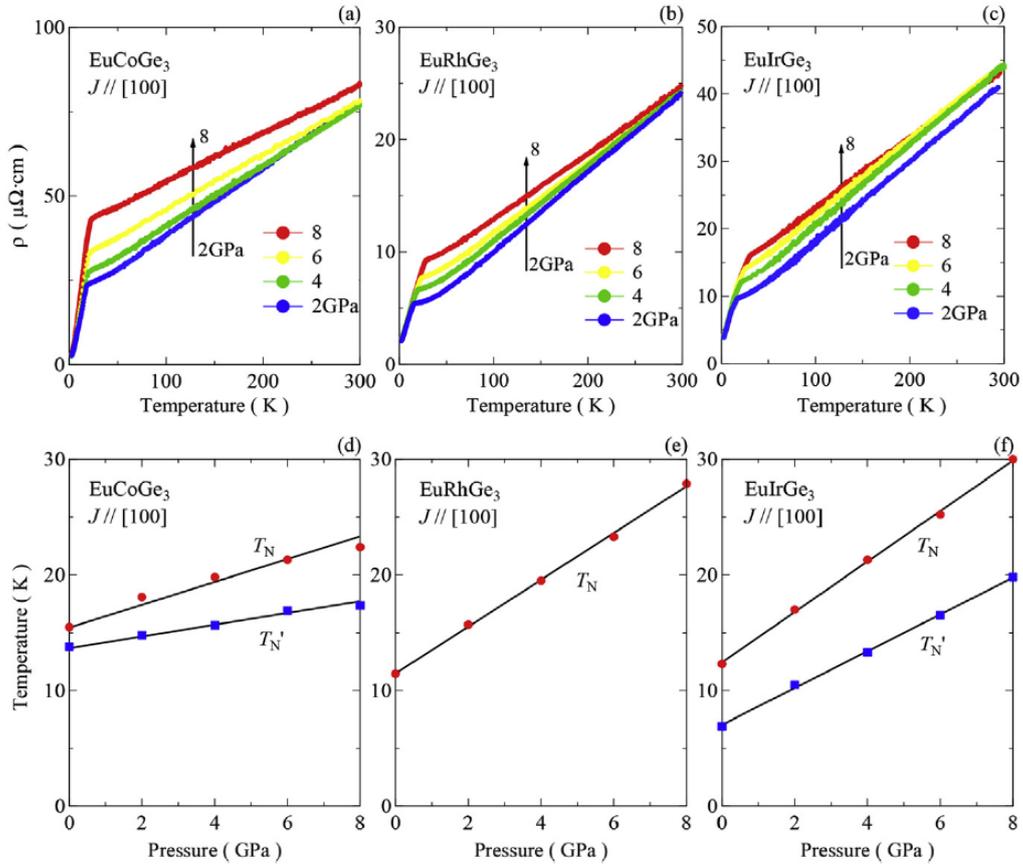


Figure 1.8: Temperature dependent electrical resistivity curve of (a)  $\text{EuCoGe}_3$ , (b)  $\text{EuRhGe}_3$ , and (c)  $\text{EuIrGe}_3$  under pressures. (d-f) magnetic transition temperatures as a function of pressure obtained from the resistivity curves above. These figures are taken from Ref.[44]

understanding of the pressure phase diagram of the  $\text{EuTGe}_3$  series and will enlighten differences/similarities between the Eu-122 system and Eu-113 systems. The electrical resistivity measurement under pressure aims to investigate potential pressure-induced superconductivity in  $\text{EuIrGe}_3$ .

## 1.8 Thesis outline

The pressure evolution of electronic and crystal structure of  $\text{EuTGe}_3$  was studied with various experimental techniques, and the effect of different transition metal constituents on pressure evolution of Eu valence was investigated. The P-T phase diagram of  $\text{EuIrGe}_3$  was expanded with the help of electric resistivity under pressure.

Chapter 2 consists of the experimental details of the high-pressure setup, including infor-

mation on the Diamond Anvil Cell, its working mechanism, and its use in various high pressure experiments. This chapter also covers the basics of experimental techniques used in the research.

In Chapter 3, the results of X-ray Absorption Spectroscopy (XAS) and X-ray Diffraction (XRD) under pressure are presented, along with a detailed explanation of data analysis methods. A comparison between pressure evolution of electronic structure and crystal structure of three compounds is provided. Electric resistivity under pressure of  $\text{EuIrGe}_3$  up to 15 GPa is presented, along with the proposed P-T phase diagram.

Chapter 4 contains the summary of the thesis, providing an overview of all the experimental results.

The main results which are presented in this thesis have been published in two research articles, and one article has been accepted for publication in **High Pressure Research**. These three research articles are:

1. Y. Utsumi, I. Batistić, V. Balédent, S. Shieh, **N. Dhami**, O. Bednarchuk, D. Kaczorowski, J. Ablett and J.-P. Rueff, *Electronic Structure* 3, 034002 (2021).
2. **N. Dhami**, V. Balédent, O. Bednarchuk, D. Kaczorowski, S. Shieh, J. Ablett, J.-P. Rueff, J. Itié, C. Kumar and Y. Utsumi, *Physical Review B* 107, 155119 (2023).
3. **N. Dhami**, V. Balédent, I. Batistić, O. Bednarchuk, D. Kaczorowski, J.P. Itié, C.M.N. Kumar, and Y. Utsumi, accepted for publication in, *High Pressure Research*.

# Chapter 2

## Experimental

Hydrostatic pressure can be generated by using pressure cells in laboratories. One of the most commonly used pressure cells for physical property measurements is the piston-cylinder cell. The advantages of the piston-cylinder cell are a large sample space and relatively easy handling. (The details of the piston-cylinder cell are presented in Appendix B.0.2.) However, the pressure range is limited to  $\sim 3$  GPa. When higher pressure is required, a Diamond Anvil Cell (DAC) can be utilized to achieve pressure up to  $\sim 100$  GPa.

The pressure evolution of electronic and crystal structures of  $\text{EuTGe}_3$  ( $T = \text{Co, Rh and Ir}$ ) and its pressure-temperature phase diagram were studied by using complementary experimental techniques. As mentioned in the introduction, the study required to reach very high pressure (up to 50 GPa). Therefore, a DAC was employed for high-pressure generation. This chapter aims to introduce the working principle of a DAC which was commonly used in three different types of experiments, the pressure calibration methods for each measurement, and the principles of X-ray absorption spectroscopy and X-ray diffraction.

Section 2.1 explains details about DAC including its working principle, gasket materials selection, preparation and pressure transmitting mediums. In section 2.2, pressure calibration methods used in different experiments are presented.

Electric resistivity measurements under pressure above a few GPa were especially challenging, and implementation of the transport DAC and achieving reliable measurements required enormous effort. Therefore, section 2.3 is dedicated to the DAC for electric resistivity measurements under pressure to explain its mechanism and a sample preparation procedure. In section 2.4, principles of HERFD XAS and experimental conditions for XAS under pressure are presented. Section 2.5 covers the principles of XRD and experimental conditions of XRD under pressure for synchrotron and lab XRD measurements.

## 2.1 Working Principle of DAC

The DAC is a widely used and versatile high-pressure device. The first design of the DAC was reported by Weir et al [52] in 1959 which could go up to 3 GPa. Since then the DAC has undergone continuous evolution in the succeeding decades.

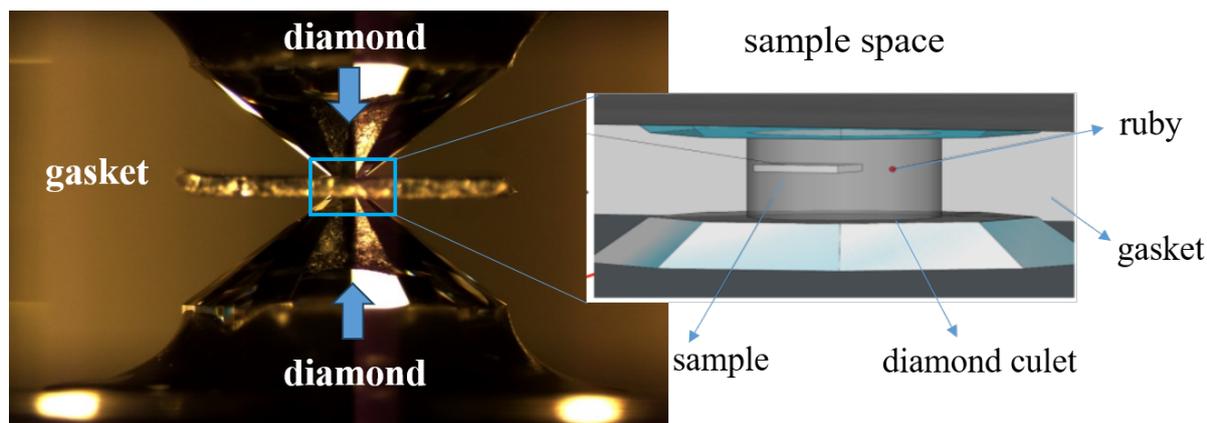


Figure 2.1: Side view of a diamond anvil cell. Two opposing diamonds attached on backing plates, and a gasket is pressed in between diamond culets. A magnified view of sample space with pressure indicator ruby in it.

Figure 2.1 presents the side view of DAC. The DAC comprises two opposing diamond anvils that compress a sample between them. Gem-quality diamonds, whether natural or synthetic, are attached to rigid backing plates made of tungsten carbide, hardened stainless steel, and/or beryllium copper. A pair of diamond anvils is aligned within a pressure cell, ensuring that their opposed faces (culets) are parallel and precisely overlapping. The pressure in a DAC is applied by screw or membrane mechanism.

The choice of diamond is due to its exceptional hardness and ability to withstand immense pressures without significant deformation. Diamond makes an ideal anvil for X-ray analyses; it has a low atomic number and therefore a very low absorption. The diamond culet shape plays an important role, with the most commonly used being the flat diamond culet. Various diamond anvil geometries have been proposed to generate higher pressure in the terapascal (TPa) range, including single/double-beveled anvil, toroidal anvil, and double-cup anvil designs [53].

### 2.1.1 Gasket and pressure transmitting mediums

A gasket in a DAC should have a small and well-defined sample space between the diamond anvils. The sample space is typically cylindrical or toroidal in shape to confine the sample and

pressure transmitting medium. The design of a gasket and its material are influenced by the desired pressure range, the nature of the sample (e.g., conductivity, reactivity), and the specific experimental requirements. Gaskets are typically made of materials such as stainless steel, rhenium, and other high-strength alloys. The relations among gasket thickness, pressure stability, and evolution of stress of gasket material were studied by Dunstan [54]. A pre-indentation of the gasket was suggested to increase the stability of pressure.

**Gasket materials:** The most frequently used material for gaskets are beryllium, stainless steel, tungsten, rhenium, Ni(Cr 39-41%)(Al 3-4%) and CuBe. Beryllium is transparent to x-ray with small absorption and can be used up to 50 GPa pressure. However, machining beryllium is dangerous and can cause terminal disease called Chronic Beryllium Disease. Rhenium and tungsten gasket are useful for high pressure range  $\sim 50$  GPa, and stainless steel gasket is used for lower pressure regions ( $\sim 30$  GPa).

**Pressure transmitting medium (PTM):** To ensure hydrostaticity in the DAC, the gasket sample space is usually filled with PTM, which is supposed to limit the pressure gradient and shear strains. Inevitably, the melting line of fluids eventually rises under pressure, leading to a solidification of PTMs at a certain pressure. Beyond this point, the pressure inside the sample space tends to be inhomogeneous, and both differential (mostly uni-axial) stress and shear stresses emerge. The commonly used PTM are He, Ne, Ar, Daphene oil, NaCl, etc.

Table 2.1 presents the different gasket materials, pressure gauge, and PTM used for the various experiments.

Table 2.1: Experiment type, gasket material, pressure gauge, and corresponding PTM. Note: For electric resistivity under pressure at room temperature, the pressure was detected with ruby. While at low temperature, the pressure in the DAC was calibrated with lead  $T_c$ .

Experiment type	Gasket material	Pressure gauge	PTM
HERFD XAS	beryllium	ruby fluorescence	Ne
Transmission mode XAS	rhenium	ruby fluorescence	4:1, Methanol:Ethanol
XRD	stainless steel/rhenium	gold EOS	Ne or He
Electric resistivity	stainless steel	lead $T_c$	Daphne 7373

## 2.2 Pressure calibration methods

Different pressure calibration / detection methods were used in various experiments according to convenience. Followings are the detailed descriptions of pressure calibration methods in different experiments.

### 2.2.1 Ruby fluorescence pressure gauge

The ruby fluorescence pressure detection method was used for HERFD XAS and electric resistivity under pressure at room temperature. Laser-induced ruby fluorescence R1 line is most commonly used as a pressure gauge for pressure determinations up to hundreds of GPa range (optical sensor). Ruby is chromium-doped corundum ( $\text{Al}_2\text{O}_3$ ). The  $\text{Cr}^{3+}$  ion is in an octahedral coordination with six surrounding oxygen ions. The R1 and R2 fluorescence lines (wavelength 694.2 and 692.81 nm, respectively) are separated by a crystal field splitting of the  ${}^2E$  level of the  $\text{Cr}^{3+}$  ions in a corundum ( $\text{Al}_2\text{O}_3$ ) lattice (Fig. 2.2 (a)).

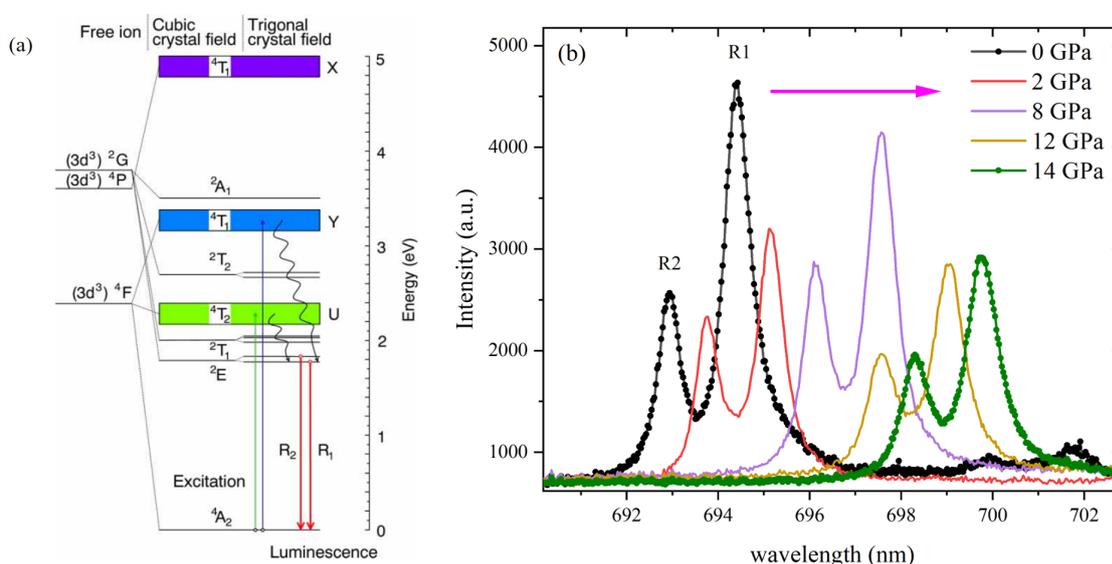


Figure 2.2: **(a)**: Excited states of  $\text{Cr}^{3+}$  in ruby, taken from [55]. In the weak crystal field limit, one starts from the free-ion multi-electron states. The states split due to the ligand field and interactions between terms. Optical absorption into the  ${}^4T_2$  and  ${}^2T_2$  levels (the U and Y bands) and sharp R-line luminescence originating from the  ${}^2E$  level are indicated. **(b)**: Ruby fluorescence spectra as function of pressure. R1 and R2 peaks show shift to higher wavelength (low energy) with increasing pressure. These experiments were performed at the institute of physics, Zagreb.

A linear red shift of the ruby fluorescence R1 line ( ${}^2E_g \rightarrow {}^4A_{2g}$  emission following  ${}^4A_{2g} \rightarrow {}^4T_{2g}$  or  ${}^4T_{1g}$  excitation) as a function of pressure up to 2.3 GPa was first showed in 1972 by Forman et al. [56]. The linear red shifts of ruby fluorescence spectra at various pressure are presented in Fig. 2.2 (b). The ruby fluorescence under pressure at low temperatures was also studied [57], which showed the decrease of intensity of R1 and R2 peaks with decreasing temperature. While the intensity of N lines originating from exchange-coupled Cr ion pairs

is enhanced at low temperatures, which is proposed as an alternative scale for pressure at low temperatures.

A number of empirical calibration curves of the R1 fluorescence shift at high-pressures and temperatures have been proposed for the ruby pressure scale. The pressure calibration by ruby fluorescence was done by following equation;

$$P(V) = a \left[ \left( \frac{\lambda - \lambda_0}{\lambda} \right) + b \left( \frac{\lambda - \lambda_0}{\lambda} \right)^2 \right] \quad (2.1)$$

with  $a = 1798$  and  $b = 8.57$  [58]. The shift of the R1 and R2 lines ( $\lambda_0 = 694.34$  nm and 692.81 nm are R1 and R2 peaks of the zero-pressure wavelengths at 298 K, respectively.) The pressure calculation in case of hydrostatic and non-hydrostatic pressure is presented in Appendix ??.

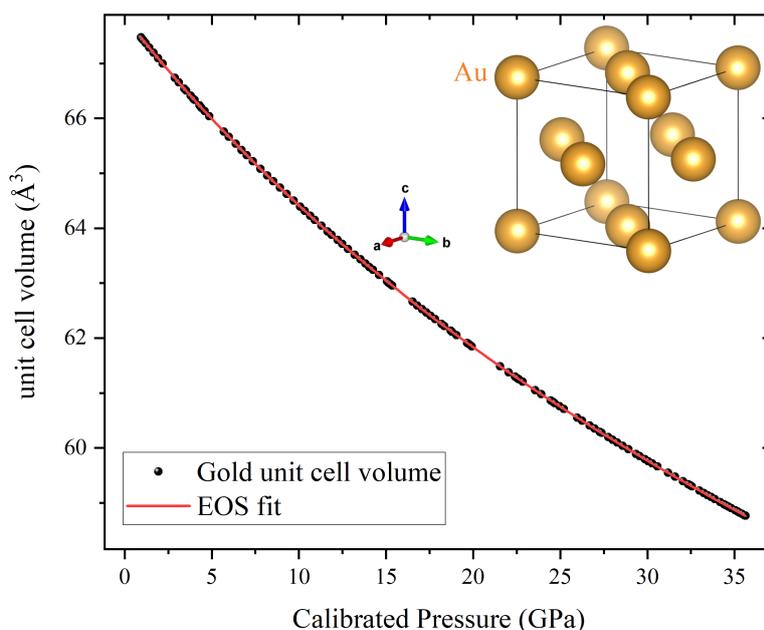


Figure 2.3: Unit cell volume of gold and EOS fitting as a function of calibrated pressure. Inset shows the crystal structure of gold (Fm-3m, 225) drawn by VESTA [26]. These experiments were performed at the Soleil synchrotron, France.

### 2.2.2 Gold equation of state

For XRD experiments under pressure, a small amount of gold powder was loaded with sample in the DAC as a pressure reference material (diffraction sensor). XRD diffractograms at various

loads (load on pressure cell) for gold were collected. The unit cell volume of gold at various pressures is presented in Fig. 2.3. The pressures were determined by using the 3<sup>rd</sup> order Birch Murnaghan equation. The 3<sup>rd</sup> order Birch Murnaghan equation below was used for EOS fitting [59]:

$$P(V) = \frac{3B_0}{2} \left[ \left( \frac{V_0}{V} \right)^{7/3} - \left( \frac{V_0}{V} \right)^{5/3} \right] \left\{ 1 + \frac{3}{4}(B'_0 - 4) \left[ \left( \frac{V_0}{V} \right)^{2/3} - 1 \right] \right\},$$

Here,  $B_0$  and  $B'_0$  denote the bulk modulus at 0 GPa and the first pressure derivative of the bulk modulus, respectively.

$$B_0 = -V \left( \frac{\partial P}{\partial V} \right)_{P=0} \quad \& \quad B'_0 = \left( \frac{\partial B}{\partial P} \right)_{P=0}.$$

The unit cell volume at 0 GPa  $V_0 = 67.847 \text{ \AA}^3$ , bulk modulus  $B_0 = 167 (\pm 11) \text{ GPa}$ , and  $B'_0 = 5.5 (\pm 0.8)$  were taken from [60] and used for calibration.

### 2.2.3 Lead (Pb) superconducting transition temperature

Superconducting transition temperature ( $T_c$ ) is very sensitive to external pressure, which makes it an excellent candidate for pressure gauge. The most commonly used pressure gauges are lead (Pb,  $T_c = 7.2 \text{ K}$ ) and tin (Sn,  $T_c = 3.7 \text{ K}$ ). The superconducting transition  $T_c$  decreases with increase of pressure in lead as presented in Fig 2.4 (a).

For electric resistivity measurements under pressure, when the pressure cell is in the temperature range of liquid helium, lead  $T_c$  is ideal for pressure gauge. Since parts of a DAC are made of metals, DAC undergoes thermal contractions during low-temperature experiments. Especially in BeCu DAC for electric resistivity measurement, the thermal contraction tends to deviate pressure at low temperature from the pressure at room temperature determined by ruby fluorescence. This deviation was observed in the pressure range ( $\geq 5 \text{ GPa}$ ), and value was determined to be around 1 GPa, as presented in Fig. 2.4 (b).

Due to the limited sample space in the DAC and mandatory electrodes for electric resistance measurements, a sample and the pressure reference lead were measured separately. Note that during the measurement of lead, experimental conditions (disc spring washer stacking, gasket material and size and pressure medium) were kept the same as the electric resistivity measurement of the sample. The pressure calibration was performed by using following equation: [61]

$$T_c(P) = T_c(0) - (0.365 \pm 0.003)P,$$

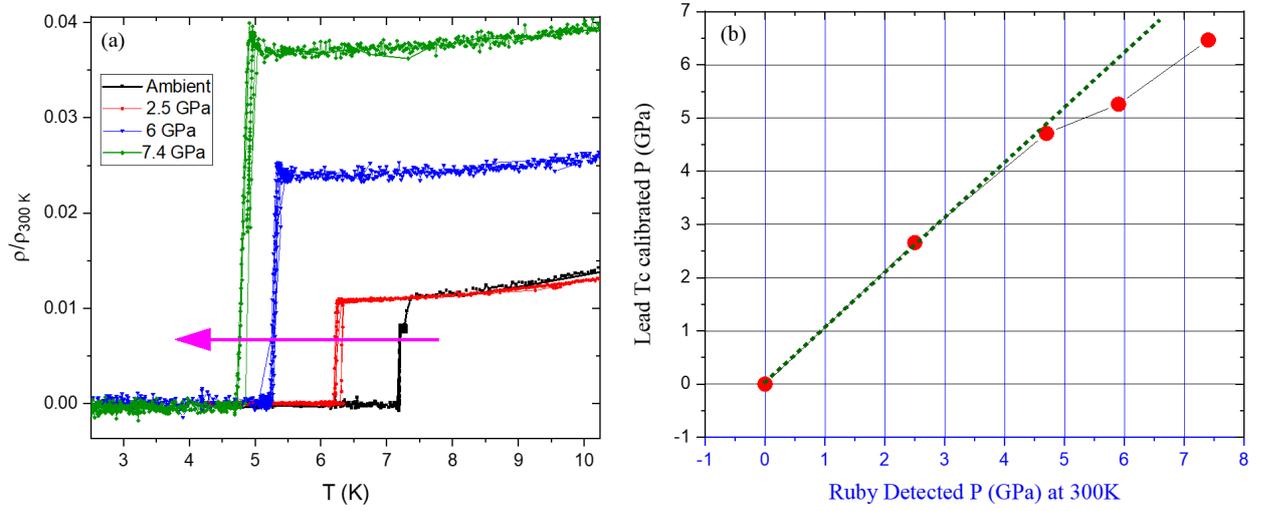


Figure 2.4: **(a)**: Normalized electric resistivity curves of lead at selected pressure. Effect of increase in pressure on  $T_c$  of lead can be seen as a shift towards low temperatures. **(b)**: The obtained pressures from lead  $T_c$  and the pressure determined by ruby fluorescence at 300K. These experiments were performed at the institute of physics, Zagreb.

where  $T_c(0)$  is the superconducting transition temperature of lead at 0 GPa and  $T_c(P)$  is transition temperature at respective pressure.

## 2.3 Electric resistivity under pressure

Electric resistivity measurements under pressure come with additional complexity in the picture due to a presence of wires/leads for resistivity measurements. It is challenging to introduce electric leads into a sample space, especially when a metal gasket is used. To overcome these challenges various designs were proposed, as an integrated microcircuit on a diamond [62], using focused ion beam ultrathin lithographic deposited Pt-based leads on diamond culet [63]. A convenient idea is coating a thin layer of insulation on top of metallic gasket, i.e. alumina ( $\text{Al}_2\text{O}_3$ ) and boron nitride (BN), to avoid short circuit between wires and metallic gasket.

To investigate a potential pressure induced superconductivity of  $\text{EuIrGe}_3$ , electric resistivity under pressure was performed using diamond anvil cell up to 15 GPa. To observe pressure at low temperature, a pressure reference sample was desired to be loaded in the DAC with the sample. However, due to small sample space ( $\sim 300 \mu\text{m}$  diameter) only a ruby ball (5-50  $\mu\text{m}$ )

was loaded with the sample. Then, the pressure inside DAC at low temperatures was calibrated separately as presented in the previous section.

### 2.3.1 DAC Design

The DAC used for the electric resistivity measurements under pressure was made of standard BeCu alloy. The DAC was designed to be a compact size, to be compatible with the cryostats and PPMS, and to reduce temperature gradient. The DAC has the outer diameter of 25 mm, the height of 40 mm, and the piston diameter of 10 mm. For electric resistivity measurements of  $\text{EuIrGe}_3$ , diamond anvils with culet diameters of either 1.1 mm or 0.9 mm were used. The BeCu DAC for the electric resistivity measurement is presented in Fig. 2.5.

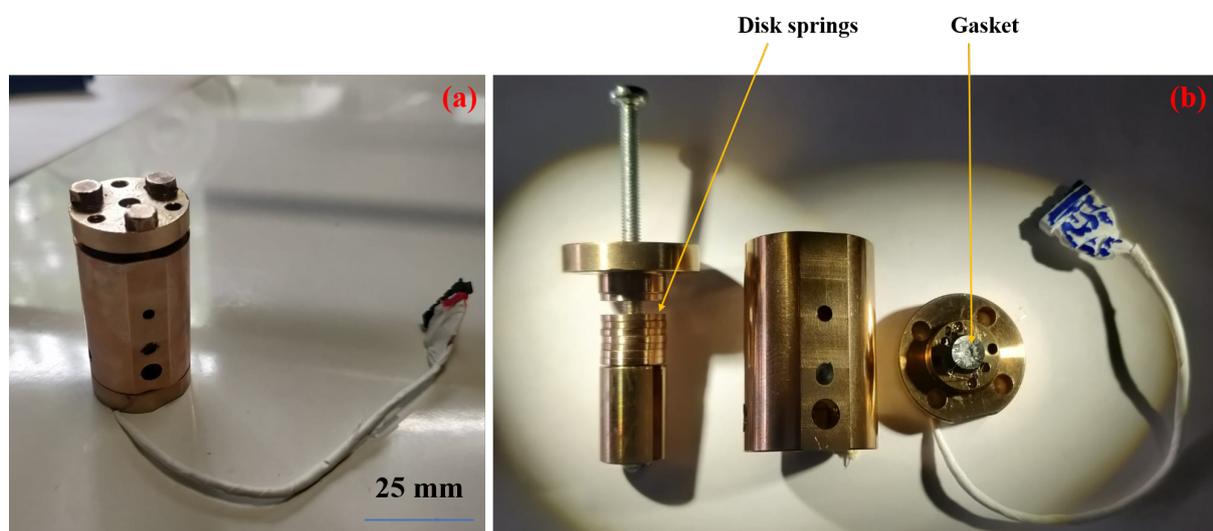


Figure 2.5: The BeCu DAC for electric resistivity measurements under pressure. (a): Assembled DAC. (b): Different components of the DAC, disk springs, piston, gasket, and diamond anvils.

### 2.3.2 Gasket material selection

To select an optimal gasket material for electric resistivity measurements in a pressure range up to 15 GPa, the stability and hardness of various materials were investigated. A variety of stainless steel materials were checked for stability and hardness up to the required pressure range (See appendix). The deformation of sample space under pressure was investigated in a few selected stainless steel gaskets (MP35N, SS304L, hardened stainless steel sheets of various thickness, and inox). The effect of pressure on the sample space was monitored as deformations of shape and size of sample space. Gaskets were made of hardend stainless steel disks and were

purchased from the Almax easylab. Fig. 2.6 and Fig. 2.7 show the changes of sample space within gaskets made of SS304L and MP35N, respectively.

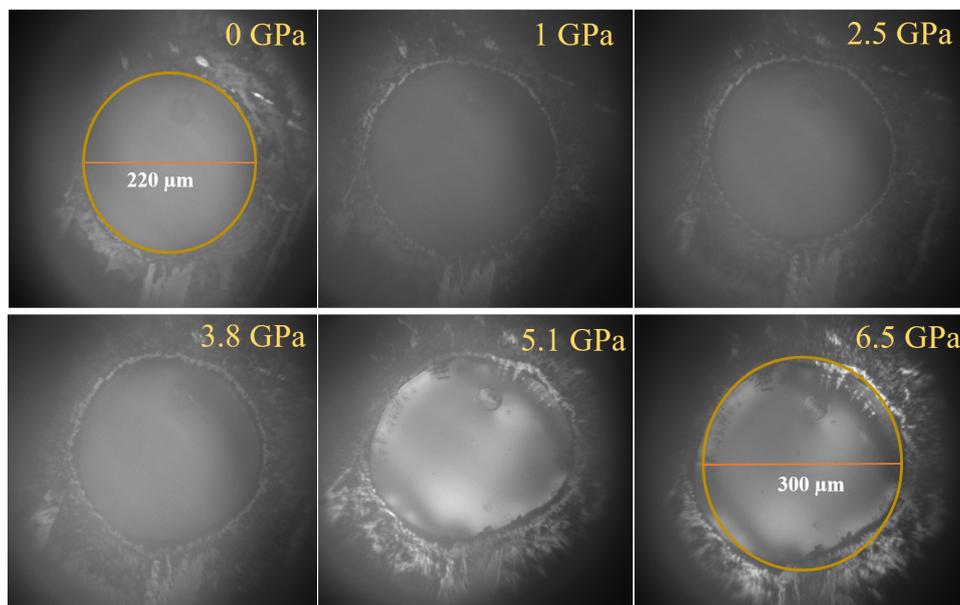


Figure 2.6: A deformation process of stainless steel gasket (SS304L). The sample space starts to expand with increasing pressure and its shape departs from the circle around 5 GPa.

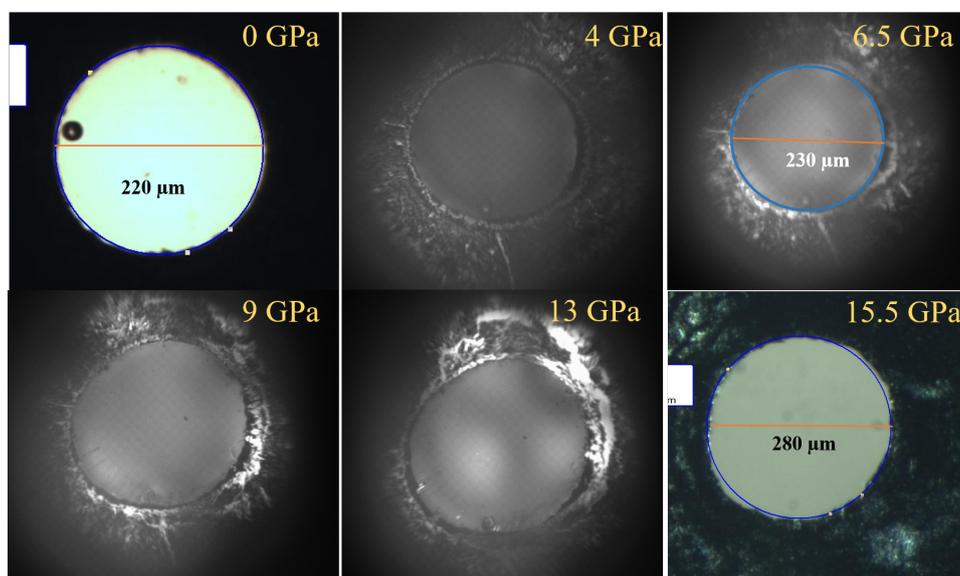


Figure 2.7: The deformation process of the MP35N gasket. Sample space starts to deform around 13 GPa.

During the application of pressure in the DAC, changes in the sample space diameter are critical factors that can lead to experimental failure. When the sample space diameter is  $\leq$

1/3 of the culet diameter, the sample space tends to collapse. Conversely, when the sample space diameter is  $\geq 1/3$  of the culet diameter, the sample space tends to expand with increasing pressure (Based on the MP35N stainless steel gasket with a 0.75 mm culet diamond). In the former case, experiments may fail due to non-homogeneous pressure distribution or sample crushing caused by the gasket, while in the latter case, diamonds may come into contact and might break. Crushing samples can be avoided by choosing small samples, though the latter case might cause irreparable damage to the diamond anvils. Hence, the gasket hole was kept less than one-third of the culet diameter for the measurements.

### 2.3.3 Preparation

Gaskets made of MP35N with a thickness of 200  $\mu\text{m}$  were pre-indented to 70  $\mu\text{m}$ . In the center of the indented area of the gasket, a sample space was drilled by a spark erosion machine. The optimal size of the sample space should be  $\sim 30\%$  of the diamond's culet. Various steps of experimental preparation are presented in Fig. 2.8.

Stycast 2650 with  $\alpha\text{-Al}_2\text{O}_3$  in a ratio of 1:4 (Stycast: $\text{Al}_2\text{O}_3$ ) was applied to the gasket using a 10-micron tungsten needle. Then, the gasket was heated on a hot plate for 1 hour at 90-100°C. Subsequently, the gasket was loaded into the DAC and pressed to a load of 400/450 Kg to flatten the insulation and make it slightly thinner. Besides providing insulation, the insulation layer increases the thickness of the sample space. The optimal insulation thickness should be 25% of the thickness of the indented gasket. Having thicker insulation increases the risk of the insulation entering the sample space and interferes with the measurement. The durability of the insulation was checked down to liquid helium temperature, and no reactions to the hydrostatic medium over time were confirmed.

### 2.3.4 Sample loading in DAC

After insulating gasket, the sample was loaded into the DAC, and then flattened platinum wires were glued onto the gasket for outer connections. The direct electric connections to the sample were prepared with 12  $\mu\text{m}$  diameter gold wires. Daphne oil 7373 was used as the pressure medium, and the ruby fluorescence technique was employed to determine pressure at room temperature. To achieve accurate pressure readings, ruby fluorescence was measured both before and after each temperature cycle of electric resistivity measurements. The pressure in the cell was generated by using a hydraulic press and manually tightening the three screws on top of the DAC, (see Fig 2.5).

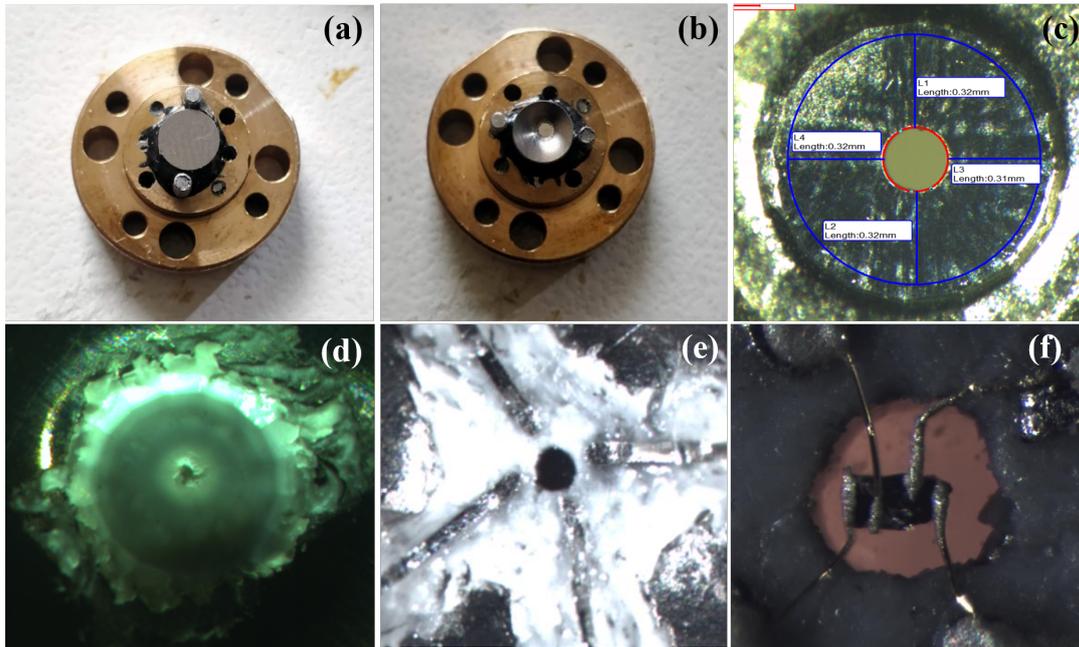


Figure 2.8: Preparation steps of electric resistivity measurements under pressure. (a) Placing the gasket on the bottom diamond. (b) Indenting the gasket with a certain load (it should be slightly higher than the expected load to generate the required pressure). (c) Drilling the sample space. (d) Placing insulation and flattening it. (e) Removing excess insulation from the sample space and positioning the outer platinum wires. (f) Loading the sample and connecting it to the outer, thicker platinum wires ( $50\ \mu\text{m}$  diameter) using a small amount of room temperature silver paste. (This involves mechanical contact between sample wires and Pt wires, so a very small amount of silver paste is recommended to avoid any short circuits.)

### 2.3.5 Measurement setup and conditions

The four-probe DC resistivity measurement technique was used to measure the electric resistivity. Small crystals of  $\text{EuIrGe}_3$  were extracted from a larger and characterized single crystal of  $\text{EuIrGe}_3$ . The sample size was too small to determine its orientation, thus, the direction of the current was not defined. The DAC was cooled down to 1.5 K at a rate of 1K/min, while heating up to room temperature was at a rate of 0.2K/min until reaching the  $T_N$ , and then at a rate of 0.3K/min for higher temperatures.

## 2.4 X-ray absorption spectroscopy under pressure

Pressure dependent HERFD-XAS was performed on  $\text{EuTGe}_3$  ( $T = \text{Co, Rh, and Ir}$ ) at various absorption edges to study the pressure evolutions of the Eu valence and charge transfers among

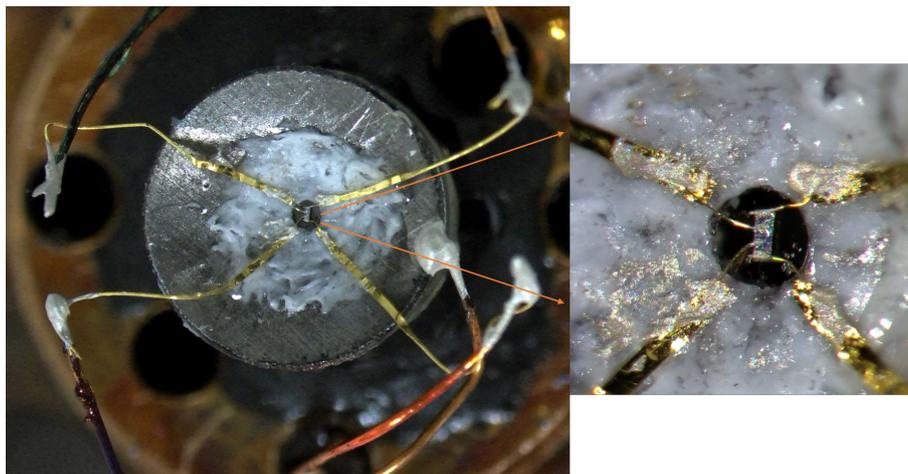


Figure 2.9: **Left:** Sample connections for electric resistivity measurement under pressure by four probe method. The outer wires are made of the gold with  $50\ \mu\text{m}$  thickness. **Right:** The magnified view of the sample space.

different elements.

### 2.4.1 Principle of HERFD XAS

The High-Energy-Resolved Fluorescence Detected (HERFD) X-ray Absorption Spectroscopy (XAS), with its atomic and orbital selectivity, is a spectroscopic probe that is quite useful for its richness of information [64]. X-ray absorption near edge spectra (XANES) provide element-selective information about the oxidation state, coordination, and spin state. HERFD XAS is a bulk sensitive photon-in photon-out process. Fig. 2.10 presents the schematic explanation of HERFD XAS process. When one uses a high energy photon, the core-level electrons are excited into the unoccupied states, and then the electron from outer shells relax into the core holes while emitting fluorescence light. The measurement method by varying incident photon energy and monitoring the fluorescence signals is called Fluorescence Yield. Here in these experiments, only specific fluorescence signals were recorded (partial fluorescence yield) to reduce the lifetime broadening due to deep core hole. It is a powerful tool to overcome the limited energy resolution of conventional XAS and to probe the detailed spectral feature near the edge.

The RXES (Resonant X-ray Emission Spectroscopy) process consists of the absorption of an incident photon  $\hbar\omega_1$ , which provokes the transition of a core electron to empty states followed by the emission of a secondary photon  $\hbar\omega_2$  upon recombination of another electron to the primary vacancy. To illustrate the narrowing effects in RXES, the case where the intermediate

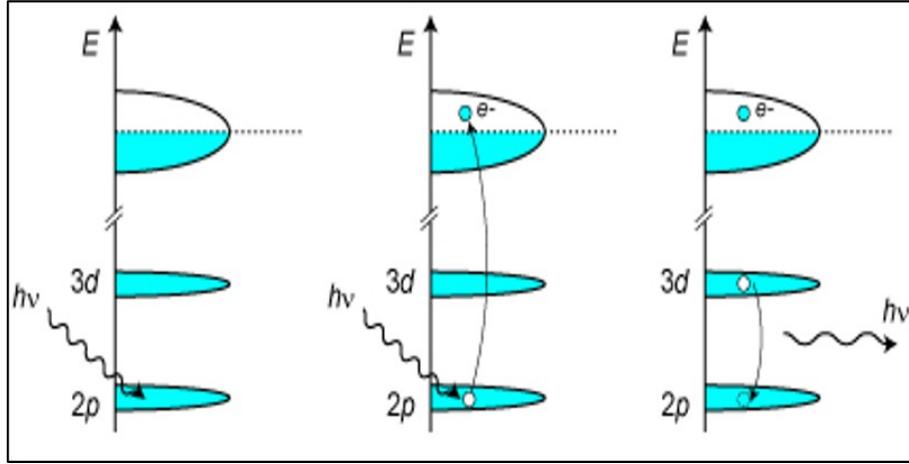


Figure 2.10: Schematic of Eu  $L_3$  HERFD XAS - High energy photon is exciting core electron to the unoccupied states. Then one electron from 3d level relaxes into the 2p core hole emitting photon with energy of  $h\nu'$ . This fluorescence signal is detected in HERFD XAS.

states are delocalized states with little overlap with the core-hole wave function was considered. Omitting interference effects, the cross-section then reads,

$$\frac{d^2\sigma}{d\Omega d\hbar\omega_2} = \sum_f \sum_i \int d\varepsilon \eta(\varepsilon) \frac{\langle f|T_2|i\rangle^2 \langle i|T_1|g\rangle^2}{(E_g - E_i - \varepsilon + \hbar\omega_1)^2 + \Gamma_i^2/4} \times \frac{\Gamma_f/2\pi}{(E_g - E_f - \varepsilon + \hbar\omega_1 - \hbar\omega_2)^2 + \Gamma_f^2/4}, \quad (2.2)$$

where  $T_1$  and  $T_2$  are the transition operators for the incident and emitted photons and  $\eta(\varepsilon)$  is density of unoccupied states. In this simplified form, the cross section merely reduces to a product of two Lorentzian functions of width proportional to  $\Gamma_i$  and  $\Gamma_f$  and centered at two different energies, respectively function of  $\omega_1$  and  $\omega_1 - \omega_2$ .

Partial fluorescence yield (PFY) mode is interesting because it resembles a standard x-ray absorption (or total fluorescence yield (TFY)) spectrum but with better resolution. The sharpening effect results from the absence of a deep core-hole in the final state. As opposed to measurements in the TFY mode however, the PFY spectra is not strictly equivalent to an absorption process, since it depends on the choice of the emitted energy. Multiplet effects in the RXES final state can also distort the PFY lineshape [64]. In the PFY mode, the lifetime broadening  $\Gamma_{PFY}$  can be approximated by:

$$\frac{1}{\Gamma_{PFY}^2} = \frac{1}{\Gamma_i^2} + \frac{1}{\Gamma_f^2} \quad (2.3)$$

In general, the lifetime broadening of the final state is considerably smaller than that of

core excited state ( $\Gamma_f \ll \Gamma_i$ ), thus giving the possibility of performing x-ray absorption spectroscopy below the natural width of the core excited state.

The HERFD, makes possible to overcome some of the main limitations of conventional XAS experiments. This technique consists of measuring the X-ray absorption spectrum via monitoring the intensity of a fluorescence line corresponding to a specific excited state decay process using a narrow energy resolution. HERFD method suppresses  $2p$  or  $1s$  core-hole life-time broadening owing to the resonant inelastic x-ray scattering process.

## 2.4.2 Experimental conditions of HERFD XAS under pressure

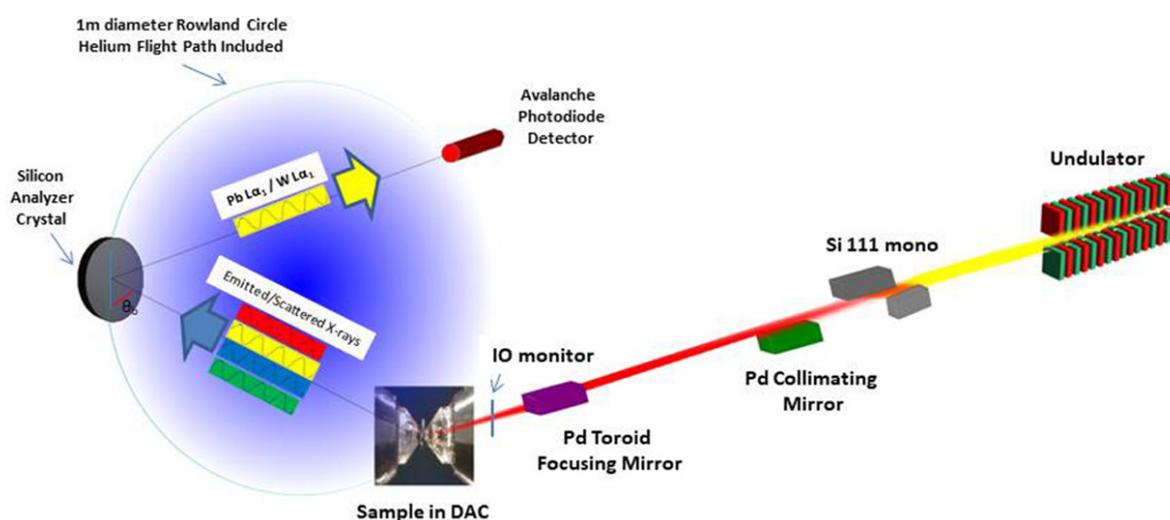


Figure 2.11: Experimental layout of HERFD XAS: The undulator x-ray radiation is monochromatized by a Si(111) monochromator, collimated by a Pd mirror, and subsequently focused at the sample in a diamond-anvil cell, by a toroidal mirror. W and Pb  $L_{\alpha 1}$  fluorescence photons emitted along the entire sample length are discriminated by the silicon analyzer and collected by an avalanche photodiode. The sample, analyzer, and detector are all situated on a 1m diameter Rowland circle in the vertical scattering plane. The incident x-ray intensity (IO) is monitored just upstream from the sample position. Figure adapted from [65].

The HERFD XAS under pressure was performed at GALAXIES beamline of Soleil synchrotron [66; 67]. The GALAXIES beamline is dedicated to inelastic x-ray scattering (IXS) and Hard X-ray PhotoEmission Spectroscopy (HAXPES). The beamline is optimized to operate in the 2.3 - 12 keV energy range with high resolution and micro beam. The incident synchrotron beam was monochromatized using a Si(111) double-crystal monochromator fol-

lowed by a Pd-coated spherical collimating mirror [65], as presented in Fig 2.11. The HERFD near-edge XAS spectra were observed by varying photon energy across the Eu  $L_3$ , Co  $K$ , Ir  $L_3$  and Ge  $K$  edges and recorded using a silicon drift detector. Each fluorescence line was selected by changing the Bragg angle of the single crystal analyzer, as presented in table 2.2.

The samples were mounted in a DAC with Ne gas as a pressure transmitting medium (PTM) and a ruby as a pressure indicator [68]. A high purity beryllium gaskets were used through which the incident and fluorescence x-rays traverse to measure the Eu  $L_{\alpha 1}$ , Co  $K_{\beta 1}$ , Ir  $L_{\alpha 1}$  and Ge  $K_{\alpha 1}$  emissions. The XAS under pressure experiment was performed with in-plane scattering mode, schematic is presented in Fig 2.12(a). The pressure was applied by manually tightening a set of 4 screws on the DAC. For an accurate pressure calibration, the ruby fluorescence signal was measured before and after the measurement of XAS spectra at each pressure.

Table 2.2: Emission line energies, analyzers and Bragg angles for various elements for HERFD experiments.

Emission line	Energy (eV)	Analyzer	Bragg angle (deg)
Eu- $L_{\alpha 1}$	5846	Ge(333)	77°
Co- $K_{\beta 1}$	7649	Ge(444)	84°
Ir- $L_{\alpha 1}$	9174	Si(800)	84°
Ge- $K_{\alpha 1}$	9886	Ge(555)	74°

### 2.4.3 Transmission mode XAS

XAS under pressure by using a transmission mode was performed at ODE (Optique Dispersive EXAFS) beamline at Soleil Synchrotron. The main advantages of Dispersive XAS are the focusing optics, the short acquisition time (few  $\mu$ s) and the great stability during the measurements due to the absence of any mechanical movement.

The experiment was performed on single crystals and powders of EuIrGe<sub>3</sub> at room temperature and 4 K using a cryostat. A single crystal of EuIrGe<sub>3</sub> was fractured, and a thin sample (approximately 20  $\mu$ m) was loaded into a rhenium gasket with 150  $\mu$ m sample space. A gas membrane DAC with 250  $\mu$ m culet diameter were used. A 4:1 mixture of methanol to ethanol PTM was used. EuIrGe<sub>3</sub> XAS spectra along the Eu  $L_3$ , Ir  $L_3$  and Ge  $K$  edge up to 50 GPa were recorded with CCD detector. Pressure was measured with ruby fluorescence method before and after the measurement of XAS spectra at each pressure.

Experimental layout of transmission mode XAS is presented in Fig. 2.12 (b). The X-rays are passing through diamond, absorption due to diamonds of various thickness and its comparison with Be gasket is presented in Fig. 2.12 (c). The absorption length ( $\mu$ t) is defined

as  $\mu t = -\ln(I/I_0)$ , where  $\mu$  is the absorption coefficient,  $t$  the thickness of the material along the x-ray path,  $I_0$  and  $I$  are intensities of the incident and transmitted x-rays, respectively [69].

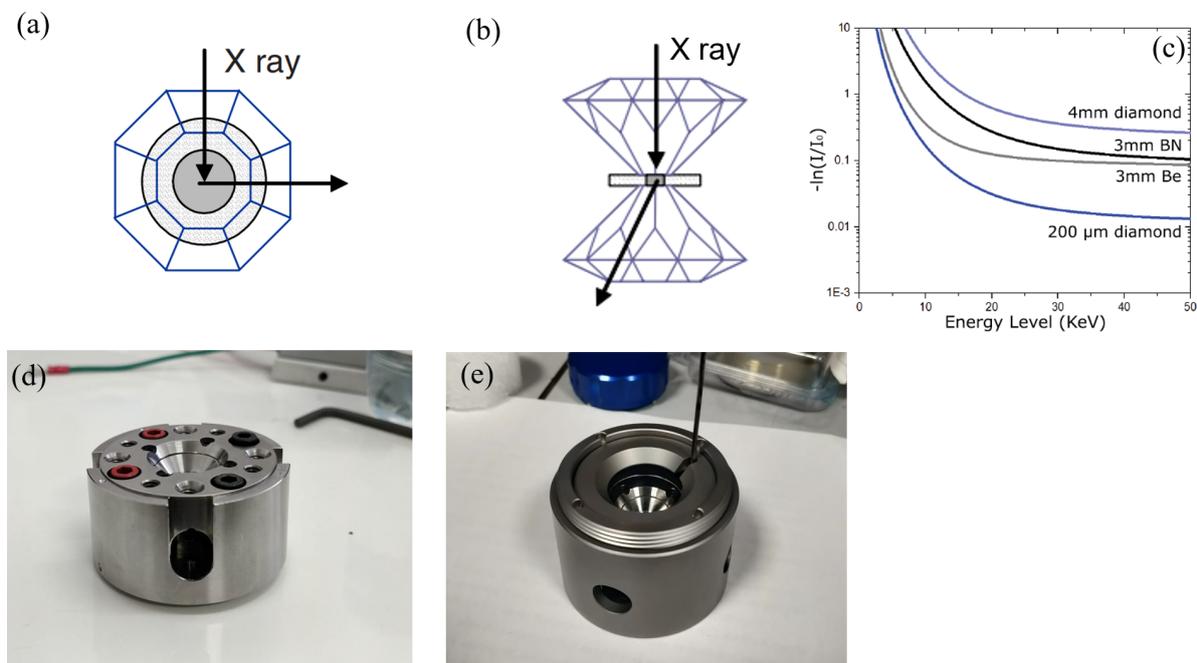


Figure 2.12: DACs used for XAS and XRD under pressure. **(a)** In-plane scattering mode for HERFD XAS experiment. **(b)** Full transmission mode for XAS and XRD experiment. **(c)** X-ray absorption length of commonly used materials in DAC as a function of energy. **(d)** Mechanical screw based DAC used for HERFD XAS under pressure. **(e)** Gas membrane DAC used for XRD and transmission XAS experiments under pressure. Its main originality is that the force on the piston is generated by pressurized helium, which pushes an annular membrane [70].

## 2.5 X-ray diffraction under pressure

X-ray diffraction (XRD) is an analytical process that provides information about crystal structure of a material. The crystal structure of a material can undergo significant changes when subjected to high pressures. Under pressure, the interatomic distances, angles, and arrangements within the crystal lattice can be altered, leading to phase transitions and the emergence of new crystal structures. The response of a material's crystal structure to pressure provides valuable insights into its behavior and properties under extreme conditions. Powder XRD as a function of pressure was performed on  $\text{EuTGe}_3$  ( $T = \text{Co, Rh and Ir}$ ) to study the crystal structure evolution with pressure. An image of gas membrane DAC used for XRD under pressure is presented in Fig. 2.12 (e).

### 2.5.1 Principles of X-ray Diffraction

XRD is the most widely used technique for characterizing crystal structures of materials. Effectively, a crystal is composed of many identical unit cells that are stacked together in a repeating array, and each of those unit cells contains atoms or molecules that are arranged in a way that can be mathematically described. The diffraction process is described by well known Bragg's law, given by:

$$n\lambda = 2d_{hkl}\sin\theta. \quad (2.4)$$

Here  $d_{hkl}$  is the distance between the parallel lattice planes with Miller indices (hkl),  $\theta$  is the angle between the lattice planes and X-rays of wavelength  $\lambda$ , and  $n$  is an integer number. When Bragg's condition is satisfied an intensity maximum occurs due to constructive interference of the scattered beam, as illustrated in Fig 2.13.

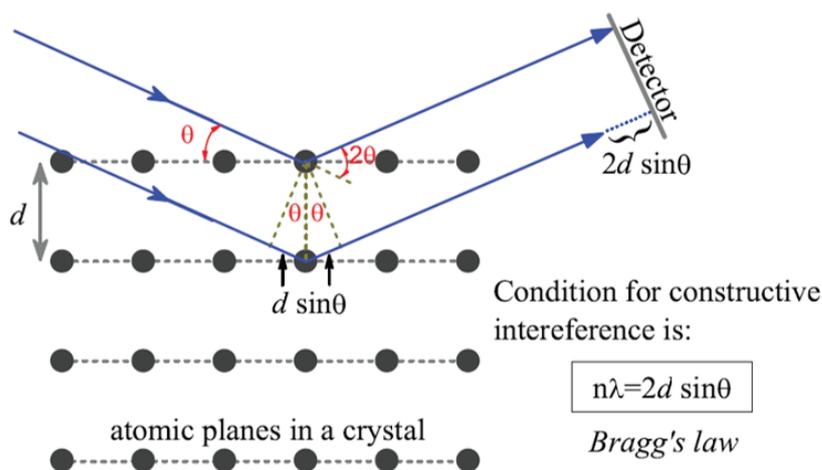


Figure 2.13: Schematic representation of Bragg's law conditions.

The purpose of a diffraction experiment is in essence the determination of the spatial arrangement of atoms in a crystal. This spatial arrangement can either be matched with those found in a database of known crystal structures (phase identification) or refined entirely (structure solution). After obtaining the arrangement of atoms, X-ray diffraction becomes a powerful tool to determine crystal orientation and identify any deviations from the ideal atomic arrangement, such as crystal deformation. This capability makes it an effective method for measuring grain orientation, strain, and defect density in a sample.

### 2.5.2 Experimental conditions of XRD under pressure

The single crystal of  $\text{EuTGe}_3$  were grinded into powder with the help of mortar and pestle within ethanol. After a few minutes, the largest grains sank to the bottom of the mortar, and the ethanol on the surface contained only the smallest grains. This ethanol is then recovered using a syringe and deposited onto a glass slide to dry. The fine powder is then collected and placed into the cell. The powder XRD (P-XRD) under pressure was performed at PSICHE beamline at Soleil synchrotron. PSICHE beamline is dedicated to x-ray diffraction under extreme conditions (pressure-temperature) and tomography at high energy (20-120 keV) [71]. The photon energy of 33 keV ( $\lambda = 0.3738 \text{ \AA}$ ) was used for P-XRD. A gas membrane DAC with  $100^\circ$  opening angle, diamond culet size  $300 \mu\text{m}$ , gasket around  $25\text{-}30 \mu\text{m}$  thickness and sample space diameter of  $150 \mu\text{m}$  were used in the experiments. Inox gasket and neon PTM was used for  $\text{EuCoGe}_3$  P-XRD under pressure. Rhenium gasket and helium (neon) PTM were used for  $\text{EuRhGe}_3$  ( $\text{EuIrGe}_3$ ) P-XRD under pressure. The recorded 2D diffraction images were integrated using Dioptas program [72]. The XRD under pressure experiments were performed in full transmission mode as presented in Fig 2.12(b).

To investigate the possibility of structural transition under pressure, single crystal XRD (SC-XRD) on  $\text{EuIrGe}_3$  was performed at CRISTAL Beamline Soleil synchrotron. Photon energy 29.7963 keV ( $\lambda = 0.4161 \text{ \AA}$ ) was used and 2D diffraction images were collected for few selected pressures. A small single crystal of  $\text{EuIrGe}_3$  was loaded in rhenium gasket with helium PTM. A gas membrane DAC with a  $90^\circ$  opening angle was used. Data was collected along x-ray beam direction with  $\Phi \pm 33.7^\circ$ , and azimuthal direction  $\chi = 0, -45^\circ$  and  $45^\circ$ . In total, 90 image files (30 at each  $\chi$ ) were combined to make one final output image file. The data reduction was performed with CrysAlis Pro [73] and structure solution was performed with Jana2020 [74].

Preliminary P-XRD experiment under pressure of  $\text{EuRhGe}_3$  was conducted in the XRD laboratory at LPS Orsay. A microfocus X-ray tube with a molybdenum anode, double collimating optics, and a MAR345 detector were utilized. The beam size was  $100 \mu\text{m}$  (circular) FWHM, with no contamination from  $k_\beta$ , thus only  $K_\alpha(1 \text{ and } 2)$  peaks. XRD under pressure of  $\text{EuRhGe}_3$  up to 15 GPa was performed. A comparison between data quality between synchrotron and lab data is presented in Appendix C.0.1.

# Chapter 3

## Results

This chapter contains the results of  $\text{Eu}T\text{Ge}_3$  ( $T = \text{Co}, \text{Rh}, \text{and Ir}$ ) obtained by utilizing multiple experimental techniques. In the section 3.1, the experimental results of pressure dependent HERFD XAS and their fitting analyses are presented. The pressure evolution of the mean Eu valence was obtained for each compound. Pressure-induced electronic structure changes and their difference among three compounds are discussed here.

In section 3.2, powder X-ray Diffraction (XRD) results under pressure are presented. Pressure evolutions of the crystal structure for each compound were determined by Rietveld refinement. By the equation of state fitting analyses, the bulk modulus and the pressure derivative of the bulk modulus of each compound were obtained from the experimental data. Differences/similarities in the pressure dependent structural changes among three compounds are discussed here.

In section 3.3, electrical resistivity measurements of  $\text{EuIrGe}_3$  under pressure are presented. By tracking a shift of the magnetic transition temperature ( $T_N$ ) as a function of pressure, pressure-temperature phase diagrams of  $\text{EuIrGe}_3$  is proposed here.

### 3.1 X-ray absorption spectroscopy under pressure

To investigate the pressure evolution of electronic structure of  $\text{EuCoGe}_3$ ,  $\text{EuRhGe}_3$  and  $\text{EuIrGe}_3$ , HERFD XAS under pressure was performed.

Firstly, the experimental results of each compound are presented in the following subsections. Secondly, a comparison among three compounds is presented to discuss the difference in pressure response arising from different natures of transition metals.

### 3.1.1 EuCoGe<sub>3</sub>

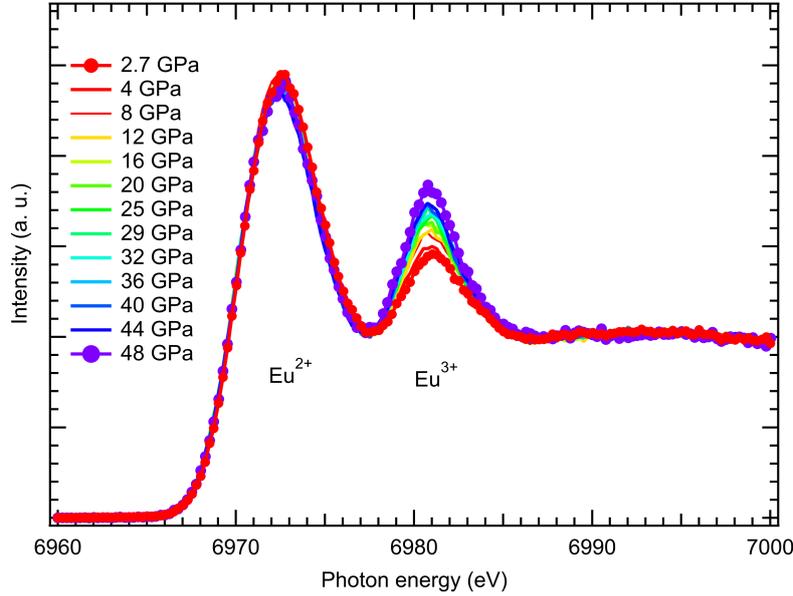


Figure 3.1: (a) The Eu  $L_3$  HERFD XAS spectra of EuCoGe<sub>3</sub> as function of pressure. The spectra are normalized at higher energy end after subtracting the constant background below the edge.

Figure 3.1 (a) shows the pressure-dependent Eu  $L_3$  HERFD XAS spectra of EuCoGe<sub>3</sub> measured at room temperature. The spectra were obtained by scanning the incident x-ray energy through the Eu  $L_3$  absorption edge while recording the scattered intensity of the Eu  $L_{\alpha 1}$  fluorescence energy. The HERFD spectra resembles to a standard XAS spectrum, though the spectral shape is sharper due to the absence of a deep  $2p$  core hole in the final state. The Eu  $L_3$  HERFD spectra exhibit a prominent peak at 6972 eV and a broad peak centered at 6981 eV corresponding to Eu<sup>2+</sup> ( $2p^6 4f^7 \rightarrow 2p^5 4f^7 + \epsilon d(s) \rightarrow 2p^6 3d^9 4f^7$ ) and Eu<sup>3+</sup> ( $2p^6 4f^6 \rightarrow 2p^5 4f^6 + \epsilon d(s) \rightarrow 2p^6 3d^9 4f^6$ ) components, respectively. Although the transition process does not directly include the  $4f$  states, the Eu<sup>2+</sup> and Eu<sup>3+</sup> peaks in the Eu  $L_3$  HERFD spectra are well separated and they are sensitive to the change of the Eu valence due to strong Coulomb interaction between the  $3d$  core hole and the final state  $4f$  electron.

Figure 3.2 shows fitting of the Eu  $L_3$  HERFD XAS spectra at 2.7 GPa (lowest pressure) and 48 GPa (highest pressure). In order to obtain the mean Eu valence, the Eu HERFD spectra are fitted with three Gaussian functions corresponding to Eu<sup>2+</sup>, Eu<sup>3+</sup> and a satellite peak, and two arctangent backgrounds for the Eu<sup>2+</sup> and Eu<sup>3+</sup> peaks. The arctangent background is to simulate the atomic part of the edge jump to the continuum. This would normally be a step function that is broadened by the lifetime effect and experimental resolution [75]. Since there was no energy

shift in the peak positions of  $\text{Eu}^{2+}$  and  $\text{Eu}^{3+}$  components with increasing pressure, the peak positions were kept constant during the fitting analysis. The mean Eu valence ( $\nu$ ) was obtained using the following formula:

$$\nu = 2 + \frac{I^{3+}}{I^{2+} + I^{3+}}. \quad (3.1)$$

Here  $I^{2+}$  and  $I^{3+}$  denote the integrated spectral intensities of  $\text{Eu}^{2+}$  and  $\text{Eu}^{3+}$  peaks respectively, extracted from the fitting. There is no signal of the quadrupolar  $2p \rightarrow 4f$  transition in the pre-edge region. Note that the intensity of the satellite peak was not included in the Eu valence estimation.

By increasing pressure, the mean Eu valence of  $\text{EuCoGe}_3$  continuously increases from  $2.2 \pm 0.02$  at 2 GPa to  $2.31 \pm 0.02$  at 48 GPa. The obtained mean Eu valence as function of pressure is presented in Fig 3.11 together with  $\text{EuRhGe}_3$  and  $\text{EuIrGe}_3$ .

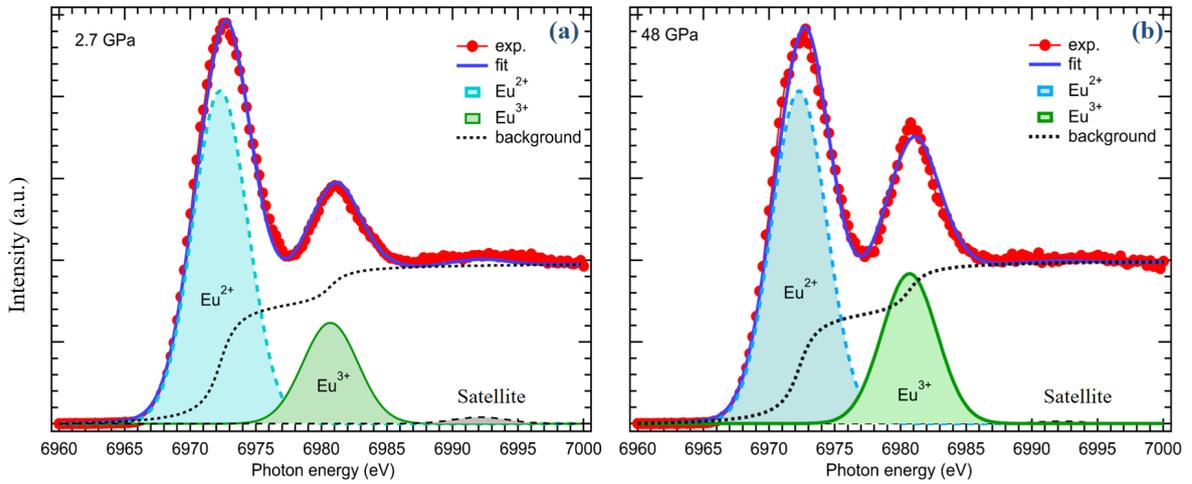


Figure 3.2: Examples of the fitting  $\text{Eu } L_3$  HERFD spectra of  $\text{EuCoGe}_3$  at 2.7 GPa (a) and 48 GPa (b) to extract  $\text{Eu}^{2+}$  and  $\text{Eu}^{3+}$  components.

The pressure dependent HERFD XAS spectra were also measured at Co  $K$  and Ge  $K$  edges. Figure 3.3 (a) and (b) shows the HERFD spectra of the Co  $K$  and Ge  $K$  edges. After subtracting a constant background below the edges, the spectra were normalized over the higher energy end. The Co  $K$  edge spectra show pre-edge shoulder structures at 7710 eV and 7720 eV and the main peak at 7729 eV which corresponds to the Co  $1s \rightarrow 4p$  dipolar transition. The pre-edge structures were reported for Co foil [76] and Co-bearing oxides [77]. The pre-edge shoulder at 7710 eV can be attributed to the Co  $1s \rightarrow 3d$  direct quadrupolar transition and the dipolar transition to  $d-p$  hybridized state [77; 76].

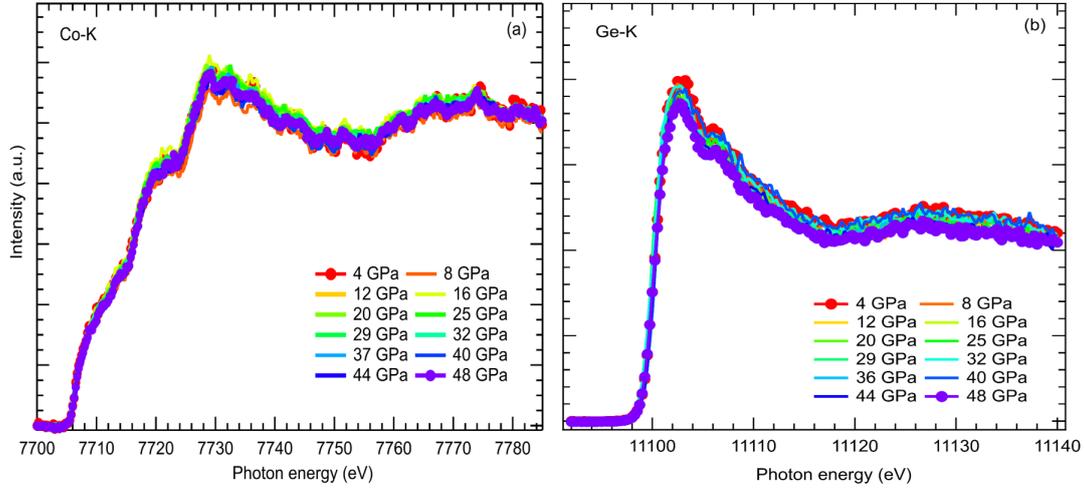


Figure 3.3: HERFD XAS results for  $\text{EuCoGe}_3$  along Co  $K$  and Ge  $K$  edge as function of pressure. Spectras are normalized on high energy end after removing the constant background.

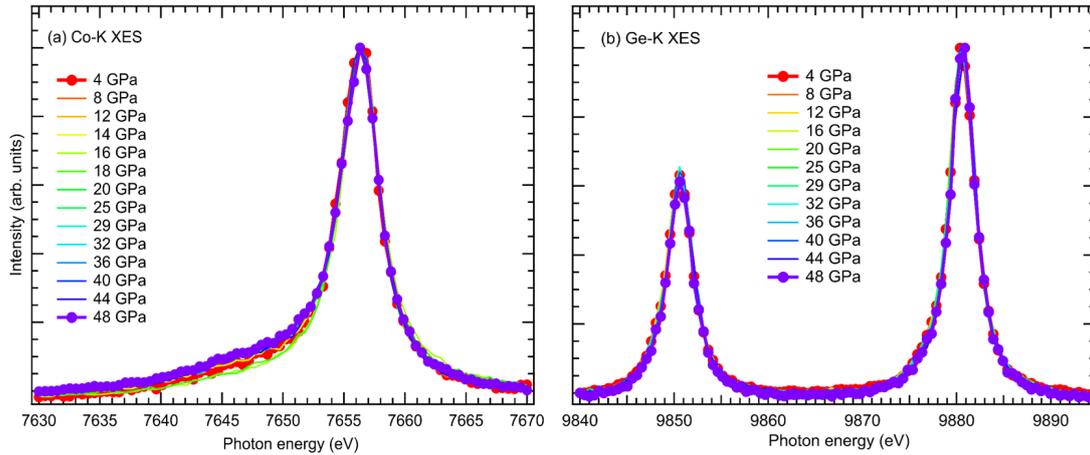


Figure 3.4: (a) Co  $K_{\beta}$  and (b) Ge  $K_{\alpha}$  emission spectra of  $\text{EuCoGe}_3$  as function of pressure.

The following pre-edge structure at 7720 eV could be due to a shakedown process of ligand to metal charge transfer [78]. The broad satellite peak far above the edge centered at 7775 eV may originate from extended x-ray absorption fine structure oscillations. The Ge  $K$  edge spectra have a main peak at 11102 eV and a shoulder peak at 11106 eV. The spectral shape is similar to the Ge  $K$  XAS spectrum of  $\text{CeCoGe}_3$  which is isostructural to  $\text{EuCoGe}_3$ . Following the interpretation of the Ge  $K$  XAS spectrum of  $\text{CeCoGe}_3$  [79], the prominent peak at 11102 eV and the shoulder peak at 11106 eV are considered to originate from Ge atoms in the Wyckoff

positions  $4b$  and  $2a$ , respectively. Within the experimental resolution, neither Co  $K$  nor Ge  $K$  edge spectra show any remarkable changes with pressure. In order to elucidate a slight change by pressure, the Co  $K_{\beta}$  and Ge  $K_{\alpha}$  x-ray emission spectra were also observed. However, no reasonable changes have been detected as presented in Fig 3.4. The Co  $K_{\beta}$  and Ge  $K_{\alpha}$  emission spectra were recorded at incident photon energies of 8209 and 11603 eV, respectively. The Co  $K_{\beta}$  emission spectrum represents the main peak located at 7656 eV corresponding to the  $K_{\beta_{1,3}}$  line. The satellite peak between 7645 eV and 7650 eV corresponds to the  $K_{\beta'}$  line. The intensity of the satellite peak changes slightly but no systematic change as a function of pressure is observed. In the Ge  $K_{\alpha}$  emission spectra, two peaks were observed. The first peak at 9850 eV corresponds to  $K_{\alpha_2}$  line and the second peak at 30 eV higher at 9880 eV, corresponds to  $K_{\alpha_1}$  line. Similar to the HERFD spectra, no considerable changes were observed within experimental resolution as a function of pressure. The results indicate that the increase of the mean Eu valence under pressure is due to intra-atomic charge transfer from Eu  $4f$  to  $5d$ , and negligible contributions from Ge and Co ions.

### 3.1.2 EuRhGe<sub>3</sub>

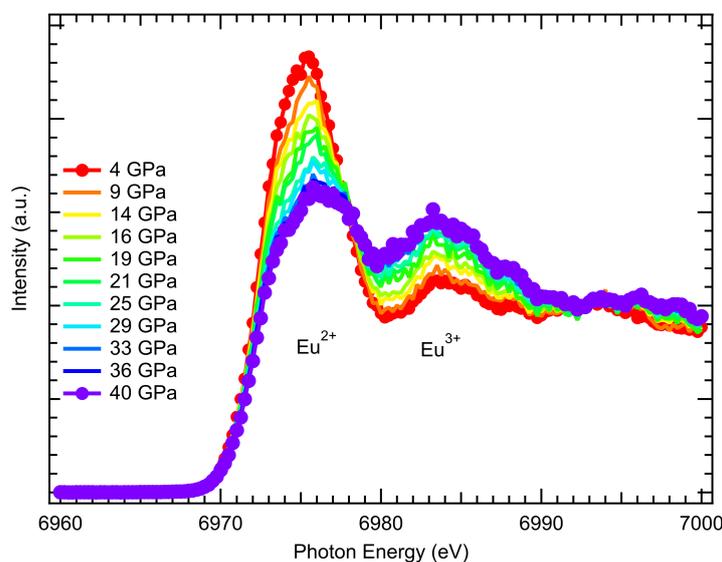


Figure 3.5: HERFD XAS results for EuRhGe<sub>3</sub> along Eu  $L_3$  edge as function of pressure.

Pressure dependent HERFD XAS spectra of EuRhGe<sub>3</sub> were measured up to 40 GPa at room temperature and presented in Fig 3.5. The Eu  $L_3$  HERFD spectra exhibit a prominent peak at 6975 eV and a broad peak centered at 6984 eV corresponding to Eu<sup>2+</sup> and Eu<sup>3+</sup> components, respectively. The HERFD XAS spectrum shows an intensity shift from Eu<sup>2+</sup> to Eu<sup>3+</sup> with

increasing pressure. A broad satellite peak was observed around 20 eV above the main line. This feature has been reported in other Eu compounds and considered to be related to the intralayer and interlayer electronic states in a layered system [80]. The Eu  $L_3$  HERFD XAS spectra was fitted with three Gaussian functions corresponding to  $\text{Eu}^{2+}$ ,  $\text{Eu}^{3+}$  and a satellite peak, and two arctangent backgrounds for the  $\text{Eu}^{2+}$  and  $\text{Eu}^{3+}$  peaks. The  $\text{Eu}^{2+}$  peak shifts toward higher energy, while the  $\text{Eu}^{3+}$  peak shifts toward lower energy with increasing pressure. The satellite peak also shifts towards higher energy with reduced spectral intensity. The peak positions determined by the fitting of  $\text{Eu}^{2+}$  and  $\text{Eu}^{3+}$  are 6974.8 eV and 6983.5 eV at 4 GPa and 6975.3 eV and 6983.3 eV at 40 GPa. The fittings of Eu  $L_3$  HERFD XAS spectra at 4 GPa and 40 GPa are presented in Fig 3.6.

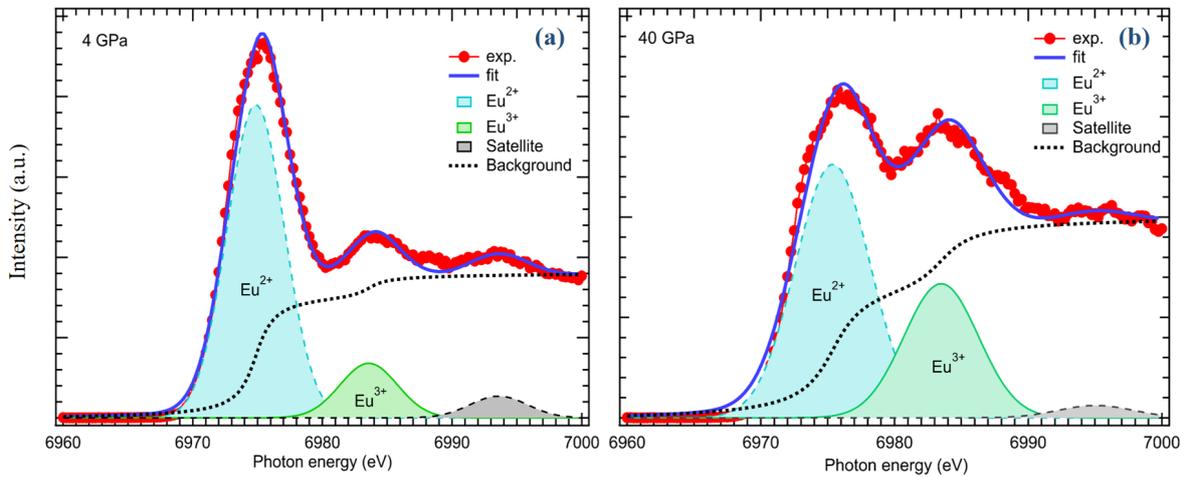


Figure 3.6: Examples of the fitting Eu  $L_3$  HERFD XAS spectra at 4 GPa (a) and 40 GPa (b) to extract  $\text{Eu}^{2+}$  and  $\text{Eu}^{3+}$  components.

The mean Eu valence ( $v$ ) obtained at ambient pressure is  $2.13 \pm 0.02$ , and increases to  $2.4 \pm 0.02$  around 40 GPa. With increasing pressure up to 20 GPa,  $v$  linearly increases, and it shows a tendency toward saturation at higher pressure as presented in Fig. 3.11.

More details about the pressure evolution of electronic structure and analysis by a full multiplet configuration interaction calculation based on the Single Impurity Anderson Model is presented in Ref.[81].

### 3.1.3 $\text{EuIrGe}_3$

Pressure dependent XAS spectra of  $\text{EuIrGe}_3$  were recorded by using powder sample. The XAS experiments were performed with both HERFD and transmission methods at room temperature.

Additionally, the pressure-dependent Eu  $L_3$  XAS spectra of EuIrGe<sub>3</sub> were recorded at 4 K.

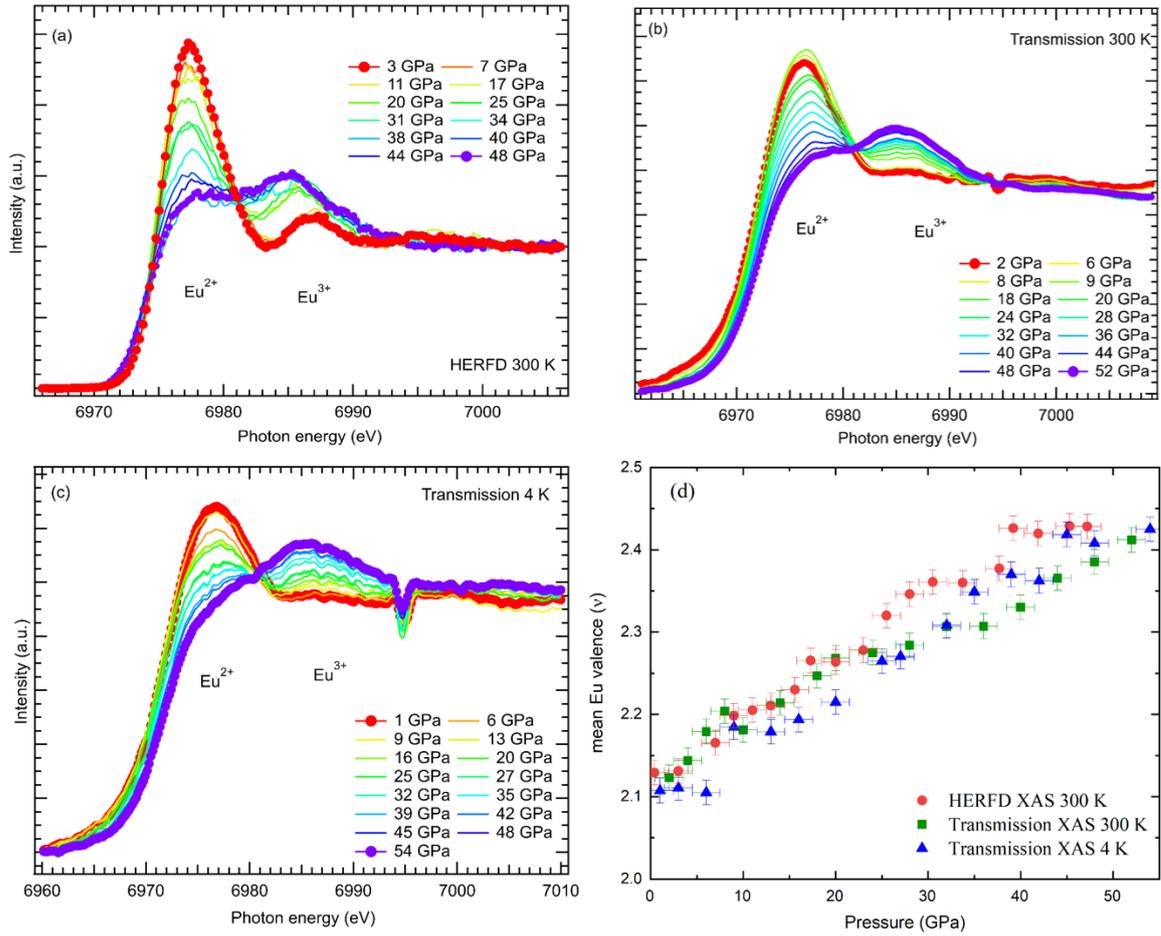


Figure 3.7: The Eu  $L_3$  XAS spectra of powder EuIrGe<sub>3</sub> as function of pressure. (a) HERFD XAS at 300 K, spectra are normalized on higher energy end after subtracting constant background below the edge. (b) Transmission XAS at 300 K, a glitch due to optics is visible at 6995 eV, (c) Transmission XAS at 4 K. (d) The mean Eu valence as function of pressure obtained from all three experiments.

The Eu  $L_3$  HERFD XAS spectra of EuIrGe<sub>3</sub> exhibit two prominent peaks at 6975 eV and 6985 eV corresponding to Eu<sup>2+</sup> and Eu<sup>3+</sup> components, respectively. With an increase in pressure, the intensity of the Eu<sup>2+</sup> peak decreases, while that of Eu<sup>3+</sup> increases, similar to the observations in EuRhGe<sub>3</sub>. Energy shifts of the peaks with increasing pressure were also noted as were observed in EuRhGe<sub>3</sub>. The Eu<sup>2+</sup> peak shifts toward higher energy, while the Eu<sup>3+</sup> peak shifts toward lower energy with increasing pressure. The mean Eu valence ( $\nu$ ) was obtained by the fitting of the Eu  $L_3$  HERFD spectra using the same fitting procedure applied to EuCoGe<sub>3</sub> and EuRhGe<sub>3</sub>. Examples of the Eu  $L_3$  HERFD XAS fitting (see Fig. 3.8 (a), (b)) and the obtained  $\nu$  as function of pressure are presented in Fig. 3.7(d). The obtained  $\nu$  at 3 GPa is 2.13,

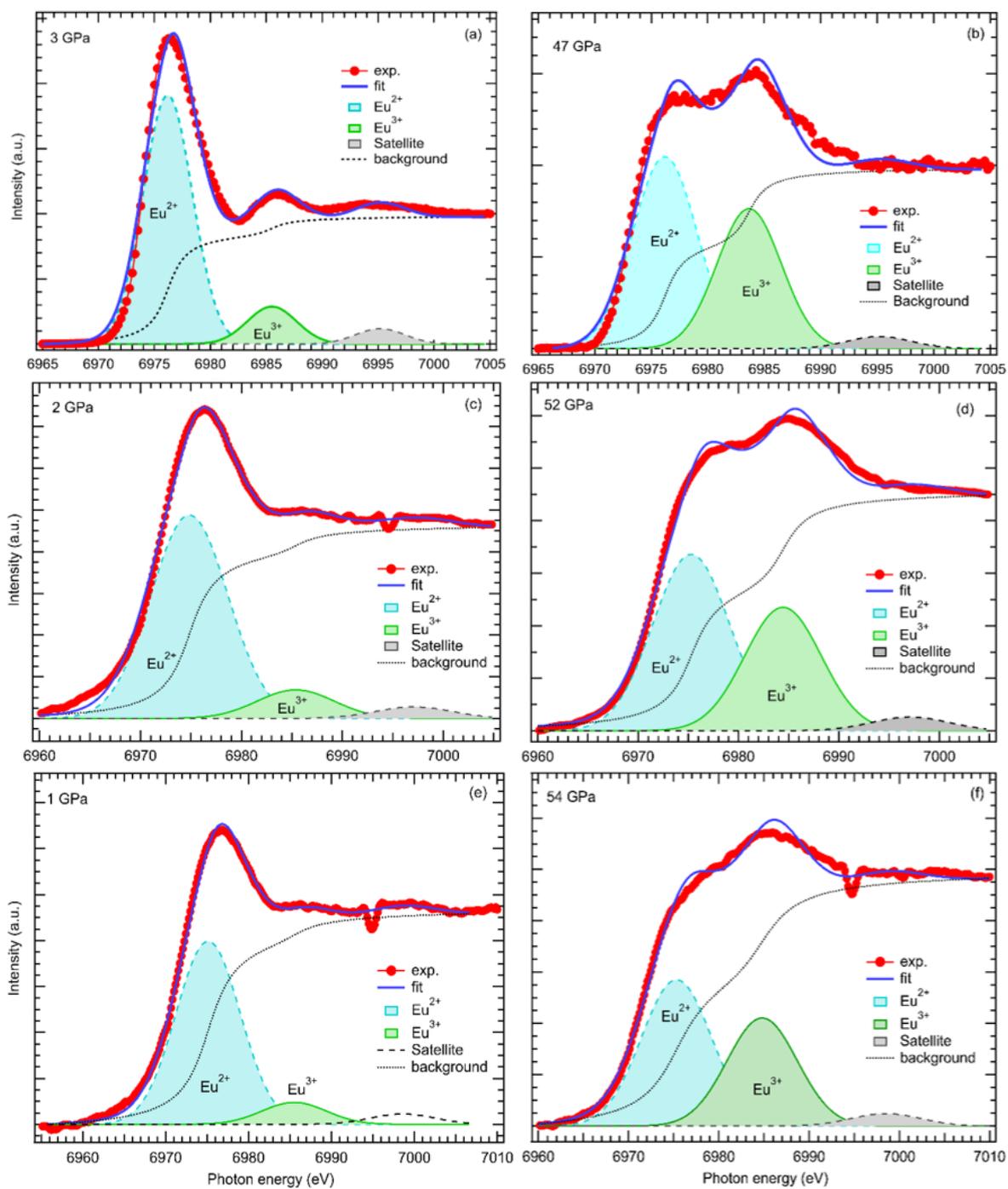


Figure 3.8: The fittings of the Eu  $L_3$  XAS spectra of  $\text{EuIrGe}_3$  at selected pressures in (a, b) HERFD XAS at 300 K, (c, d) Transmission XAS at 300 K, and (e, f) Transmission XAS at 4 K.

with increasing pressure  $v$  increases to 2.45 around 48 GPa.

The Eu  $L_3$  XAS spectra of  $\text{EuIrGe}_3$  in transmission mode at 300 K and 4 K exhibit peaks

corresponding to  $\text{Eu}^{2+}$  and  $\text{Eu}^{3+}$  at 6976 eV and 6986 eV, respectively. However, the peak widths of  $\text{Eu}^{2+}$  and  $\text{Eu}^{3+}$  are larger than those observed in HERFD XAS spectra, due to a deep 2p core hole in final state, as presented in Fig. 3.8. The background subtraction and data normalization of the spectra were performed using the XAS data processing program Athena [82]. A constant background was subtracted (-40 to -20 eV) below the absorption edge, and normalization was performed (30 to 60 eV) above the edge. With increasing pressure, the intensity of the  $\text{Eu}^{2+}$  peak decreases, while the intensity of the  $\text{Eu}^{3+}$  peak increases. The mean Eu valence was obtained using the same method as in HERFD XAS, as shown in Fig. 3.8 (c), (d), (e), and (f). The pressure evolution of  $\nu$  obtained in HERFD and transmission XAS at 4 K and 300 K is presented in Fig. 3.7(d).

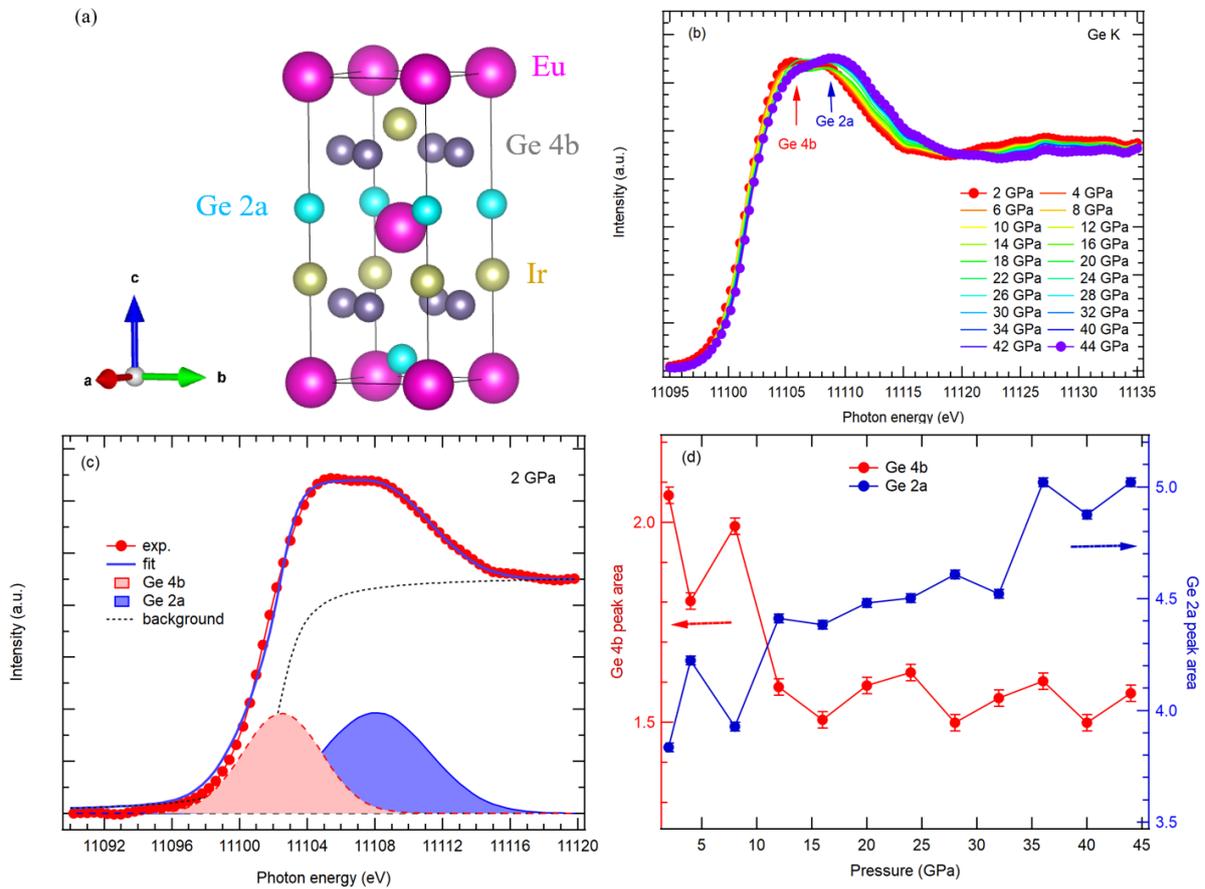


Figure 3.9: (a) Unit cell of  $\text{EuIrGe}_3$ . Ge ions occupy the 2a and 4b Wyckoff positions. (b) Pressure dependent Ge  $K$  XAS of  $\text{EuIrGe}_3$  in transmission mode at 300 K. (c) Spectra fitting of Ge  $K$  XAS and (d) spectral areas of the Ge 4b to Ge 2a peaks as a function of pressure.

The pressure dependent XAS spectra in transmission mode were also measured at Ge  $K$  and Ir  $L_3$  edge of  $\text{EuIrGe}_3$  up to 40 GPa. Within the unit cell of  $\text{EuIrGe}_3$ , Ge atoms occupy Wyckoff

positions 2a with  $4mm$  symmetry and 4b with  $2mm$  symmetry, as presented in Fig. 3.9 (a). The pressure dependent Ge  $K$  XAS spectra of  $\text{EuIrGe}_3$  is presented in Fig. 3.9 (b). Following the peak assignment in  $\text{EuCoGe}_3$ , the peaks at 11102 eV and 11108 eV corresponds to the signals from Ge atoms in 4b and 2a positions, respectively. The Ge  $K$  edge spectras are fitted with two Gaussian functions corresponding to the 4b and 2a peaks, and one step arctangent background. A example of fitting at 2 GPa is presented in Fig. 3.9 (c). With an increase in pressure the spectral intensity shift from the 4b peak to the 2a peak. The area of the Ge 4b peak decreases, while that of Ge 2a peak increases with increasing pressure, as illustrated in Fig. 3.9 (d).

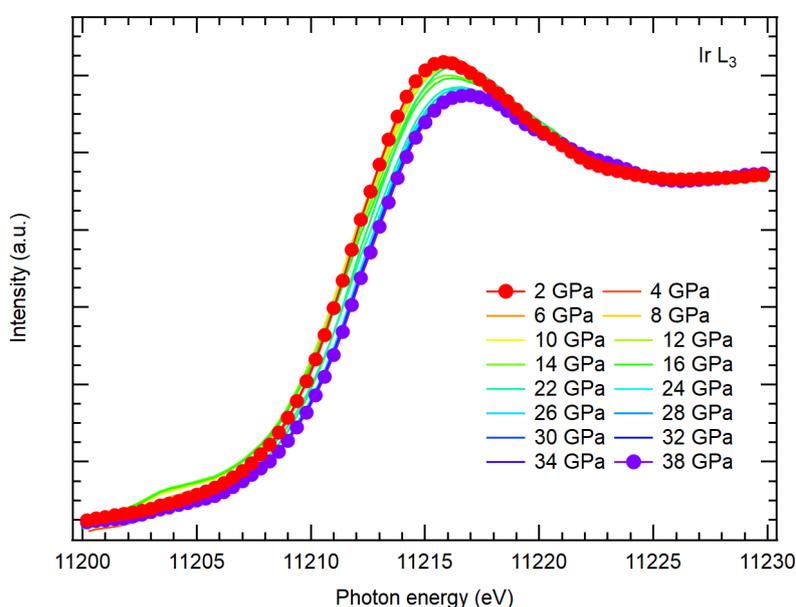


Figure 3.10: Pressure dependent Ir  $L_3$  edge XAS spectra of  $\text{EuIrGe}_3$  in transmission mode at 300 K.

The pressure dependent Ir  $L_3$  XAS spectra of  $\text{EuIrGe}_3$  is presented in Fig. 3.10. The Ir  $L_3$  XAS spectra show main peak at 11215 eV, which represents the excitation of Ir  $2p$  core-level electrons to the unoccupied states. The Ir  $L_3$  absorption edge tends to shift towards higher energy with increasing pressure. A shift of 1 eV was observed, from 11215 eV at 2 GPa to 11216 eV around 40 GPa. A similar shift in Ir  $L_3$  edge XAS as function of pressure was observed in Iridium metal [83].

Unlike the pressure responses of  $\text{EuCoGe}_3$ , both Ge and Ir XAS spectra exhibit changes along with the increase of mean Eu valence by increasing pressure. Those experimental facts imply that the large pressure change of the Eu valence in  $\text{EuIrGe}_3$  is influenced by the changes in the Ge and Ir electronic states.

### 3.1.4 Comparison of three compounds

At ambient pressure, all three compounds show the mean Eu valence close to  $v \sim 2.1$ , that are consistent with the values obtained by hard x-ray photoemission spectroscopy in Ref. [84]. Figure 3.11 shows the mean Eu valence of three compounds as a function of pressure obtained by HERFD XAS. The mean Eu valence continuously increases in all three compounds by applying pressure. However, no pressure-induced first-order valence transition was observed in any of them.

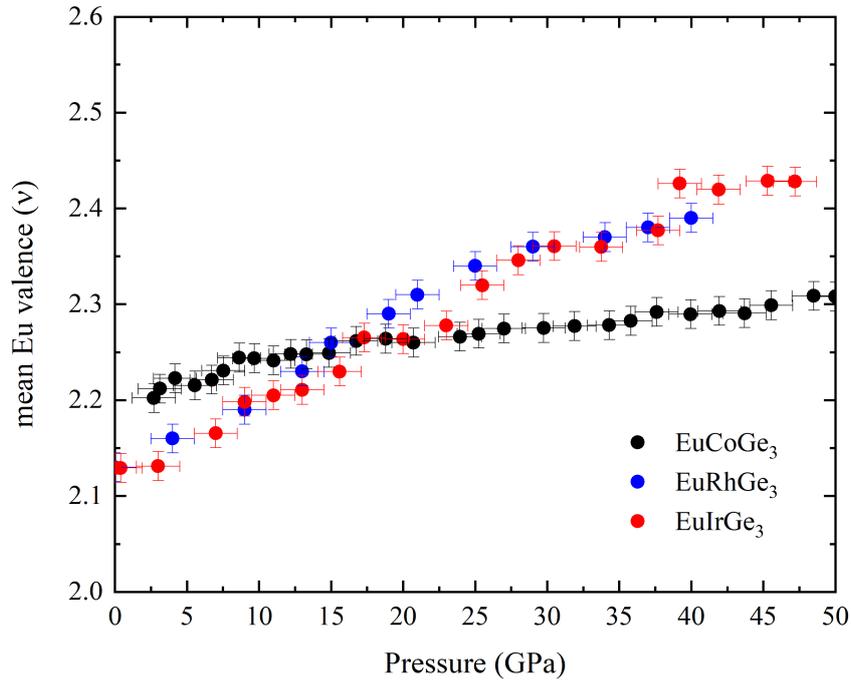


Figure 3.11: Mean Eu valence as function of pressure for all three compounds at 300 K.

The mean Eu valence changes from  $v \sim 2.2$  to 2.30 in  $\text{EuCoGe}_3$ ,  $\sim 2.40$  in  $\text{EuRhGe}_3$  and  $\sim 2.43$  in  $\text{EuIrGe}_3$  around 40 GPa. The rate of valence change ( $dv/dP$ ) in  $\text{EuCoGe}_3$  is around 0.0023/GPa, 0.0065/GPa in  $\text{EuRhGe}_3$ , and 0.0069/GPa in  $\text{EuIrGe}_3$ . The different nature of transition metal d orbitals, with 3d being localized and 5d being delocalized in  $\text{EuTGe}_3$  (See Appendix, B.0.1), could be a possible reason for the difference in pressure evolution of the mean Eu valence.

## 3.2 X-ray diffraction under pressure

To correlate the pressure evolution of the electronic structure with crystal structure and investigate the possibility of pressure-induced structural transition, XRD under pressure was per-

formed on  $\text{EuCoGe}_3$ ,  $\text{EuRhGe}_3$ , and  $\text{EuIrGe}_3$ . Rietveld refinement was performed to extract the unit cell volume and crystal structure at various pressures and compared with the DFT calculated structure. To understand the elastic properties of these crystals, EOS fitting was performed. The pressure evolutions of crystal structures are compared among three compounds with different transition metal constitutions.

### **Rietveld refinement**

In the Rietveld method, least-squares refinements are performed until the best fit is achieved between the observed powder diffraction pattern and the calculated pattern. This calculation is based on simultaneously refined models for the crystal and/or magnetic structures, diffraction optics effects, instrumental factors, and other specimen characteristics such as lattice parameters that can be modeled. A key aspect of the method is the feedback loop between improving the knowledge of the structure and the allocation of observed intensity to partially overlapping individual Bragg reflections.

The Rietveld refinement was performed with Profex program [85]. The sequential refinement method was employed due to the collection of highly dense XRD data, with some data having pressure step of 0.1 GPa.

### **DFT calculated crystal structure**

The pressure evolutions of the crystal structure of  $\text{EuCoGe}_3$ ,  $\text{EuRhGe}_3$ , and  $\text{EuIrGe}_3$  were also studied theoretically by using the Quantum ESPRESSO DFT package [86; 87]. In DFT calculations, pseudopotentials from pslibrary 1.0.0 [88] was used, with the Perdew Burke–Ernzerhof exchange-correlation functional appropriate for solids [89; 90]. The kinetic energy cutoff for wavefunctions was 150 Ry, while for the charge density and potential was 700 Ry. The Brillouin sampling was  $16 \times 16 \times 8$  (no offset), with the Marzari–Vanderbilt Fermi surface smearing [91]. To take into account the antiferromagnetic ordering on Eu, the simplified formulation of DFT+U proposed by Dudarev [92] was applied. The Hubbard interaction  $U$  for Eu was assumed to be 3.8 eV to match the Eu  $4f$  peak in the valence band spectrum by photoelectron spectroscopy measurement [84]. This  $U$  value was kept constant for all pressure calculations. The calculated density of state (DOS) of  $\text{EuTGe}_3$  at selected pressures is presented in Appendix B.0.1. The DFT calculations were performed by Prof. Ivo Batistić.

### Equation of State fitting

In order to study the elastic properties of  $\text{EuTGe}_3$ , equation of state (EOS) fitting by using EOSFit7c software [93] was performed. The 3<sup>rd</sup> order Birch Murnaghan equation for EOS fitting [59] shown below;

$$P(V) = \frac{3B_0}{2} \left[ \left( \frac{V_0}{V} \right)^{7/3} - \left( \frac{V_0}{V} \right)^{5/3} \right] \left\{ 1 + \frac{3}{4}(B'_0 - 4) \left[ \left( \frac{V_0}{V} \right)^{2/3} - 1 \right] \right\}. \quad (3.2)$$

Here,  $B_0$  and  $B'_0$  denote the bulk modulus at 0 GPa and its first pressure derivative, respectively. The  $V_0$  is unit cell volume at 0 GPa. The DFT and XRD extracted Bulk modulus and its first pressure derivative are presented in table 3.4 for all three compounds. The 3<sup>rd</sup> order Birch Murnaghan EOS fitting was also compared with Vinet EOS and results are in good agreement, (See Appendix C.0.1). The visual assessment of EOS fitting is also provided as F-f (Normalized pressure  $\mathbf{F}$  vs Eulerian strain  $\mathbf{f}$ ) plots and ellipse of confidence is also provided in Appendix C.0.1.

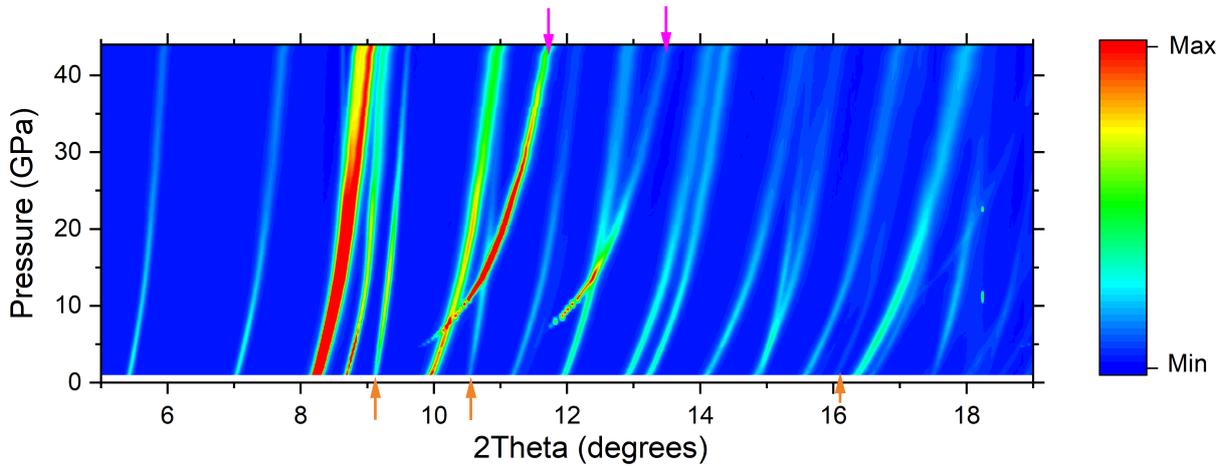


Figure 3.12: Contour map of synchrotron x-ray diffraction intensities collected in the pressure range 1–45 GPa, for  $\text{EuCoGe}_3$  (main phase), gold (standard material), and neon (pressure medium). The magenta arrows (top) and the yellow arrows (bottom) of the contour map represent the main peak positions of neon and gold respectively.

### 3.2.1 $\text{EuCoGe}_3$

Synchrotron powder XRD under pressure of  $\text{EuCoGe}_3$  was performed up to 45 GPa. Pressure evolution of XRD peaks is presented in contour diagram Fig 3.12. The pressure evolution of Bragg peak positions indicates three different phases,  $\text{EuCoGe}_3$  (main phase), gold (standard

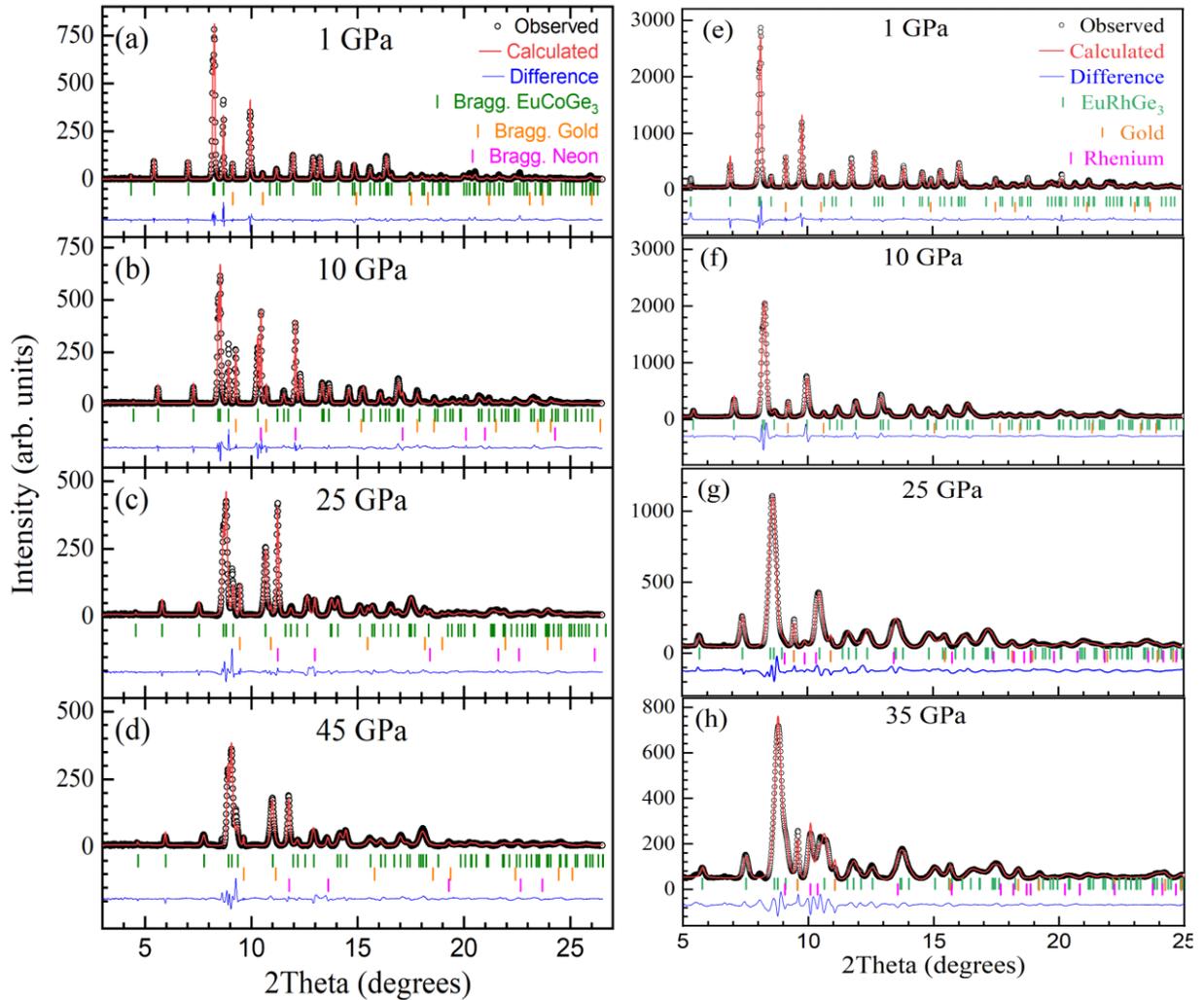


Figure 3.13: Integrated synchrotron XRD patterns of  $\text{EuCoGe}_3$  with the results of refinement at (a) 1 GPa, (b) 10 GPa, (c) 25 GPa, and (d) 45 GPa. The vertical bars indicate Bragg peak positions of  $\text{EuCoGe}_3$  (green), gold (orange), and neon (magenta). Integrated synchrotron XRD patterns and refinement results of  $\text{EuRhGe}_3$  at (e) 1 GPa, (f) 10 GPa, (g) 25 GPa, and (h) 35 GPa. The vertical bars indicate Bragg peak positions of  $\text{EuRhGe}_3$  (green), gold (orange), and rhenium (magenta).

material), and neon as hydrostatic pressure medium. With increasing pressure, all Bragg peaks are continuously shifting towards higher  $2\theta$  angle, reflecting a compression of the unit cell. Around 6 GPa, new diffraction peaks (indicated by magenta arrows) emerge due to solidification of neon pressure medium [94]. No emergence or disappearance of Bragg peaks was observed in  $\text{EuCoGe}_3$  that could be related to any symmetry change in the investigated pressure range.

The lattice parameters of each phase were extracted by Rietveld refinement. The integrated diffraction peaks and refinement fitting at selected pressures are presented in Fig 3.13 (a-d). The

extracted lattice parameters and refinement parameters at selected pressures are listed in table 3.1 with lattice parameters obtained by the DFT calculation.

The unit cell volume shows smooth contraction as a function of pressure without any structural transition, while the lattice parameter exhibits anisotropic compressibility. Fig 3.14 (a) shows the unit cell volume as function of pressure with EOS fitting and DFT calculated unit cell volume at selected pressures. Fig 3.14 (b) shows pressure evolutions of the normalized  $a$ ,  $c$  lattice parameters. The lattice parameter  $a$  exhibits greater change than  $c$  with increasing pressure. A similar behaviour was observed in DFT calculations, as presented in Appendix B.0.1. The pressure evolution of the axial ratio ( $c/a$ ) demonstrates a linear increase with increasing pressure, with a rate of  $0.002 \text{ GPa}^{-1}$  up to 21 GPa and  $0.001 \text{ GPa}^{-1}$  in the higher pressure range, as presented in Fig 3.15.

The change in slope of the axial ratio at 21 GPa originates from a change in the compressibility of the  $c$ -axis, as can be observed in Fig. 3.14 (b). Linear EOS fitting was performed to investigate the linear moduli (axial compressibility). The linear EOS fitting revealed that, when  $P > 21$  GPa was applied, the linear modulus  $M_0$  of the  $c$ -axis increases considerably, making the  $c$ -axis less compressible and resulting in a change of slope in  $c/a$ . The observed linear modulus along  $c$ -axis, initially 287 GPa ( $P < 21$ ), changes to 311.2 GPa ( $P > 21$  GPa).

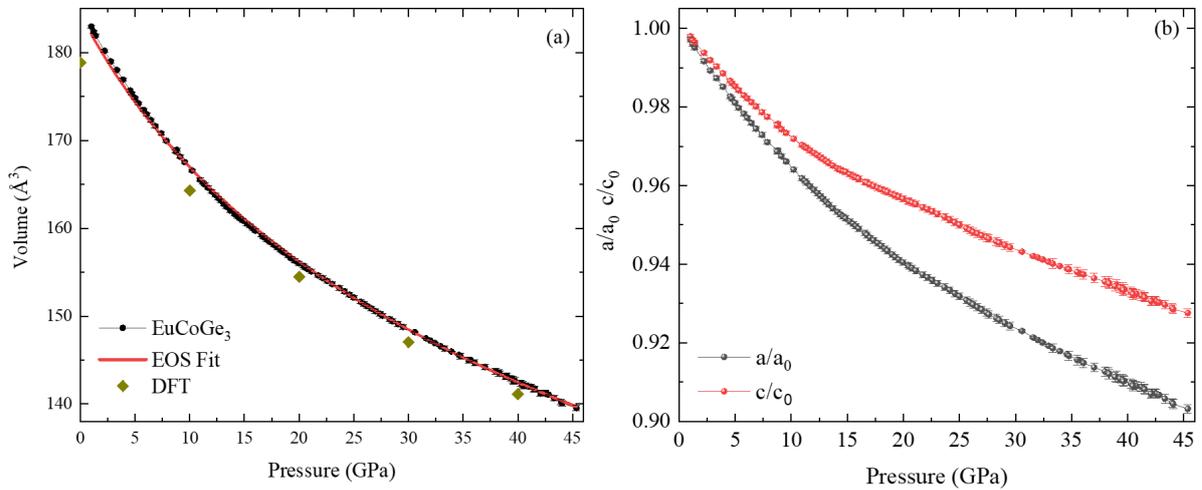


Figure 3.14: (a) XRD and DFT calculated unit cell volume of  $\text{EuCoGe}_3$  as a function of pressure and the result of 3<sup>rd</sup> order BM EOS Fit. (b) Normalized  $a$ ,  $c$  lattice parameters of  $\text{EuCoGe}_3$  as a function of pressure. The  $a_0$  and  $c_0$  values correspond to the obtained lattice parameters of the lowest pressure.

Table 3.1: **Top:** Experimental lattice parameters, unit cell volume, and refinement parameters of  $\text{EuCoGe}_3$  at selected pressures. Where  $R_{WP}$  is the weighted profile  $R$  factor,  $R_{exp}$  is the expected  $R$  factor and GOF is the goodness of fitting. **Bottom:** Lattice parameters and unit cell volume obtained by DFT calculation at various pressures.

Pressure	1 GPa	10 GPa	25 GPa	45 GPa
Lattice parameters and volume				
a (Å)	4.308 (4)	4.164 (2)	4.019 (6)	3.901 (1)
c (Å)	9.867 (1)	9.606 (9)	9.379 (2)	9.167 (1)
V (Å <sup>3</sup> )	183.156(1)	166.573(1)	151.541(4)	139.472(9)
Refinement parameters				
$R_{WP}$	17.84	16.12	17.69	21.16
$R_{exp}$	21.87	19.74	20.68	22.04
$\chi^2$	0.674	0.6669	0.7317	0.9231
GOF	0.821	0.8166	0.8554	0.9601
Pressure	0 GPa	10 GPa	30 GPa	40 GPa
Lattice parameters and volume				
a (Å)	4.269	4.1424	3.9804	3.9214
c (Å)	9.8136	9.5746	9.2821	9.1776
V (Å <sup>3</sup> )	178.8465	164.2951	147.0617	141.1274

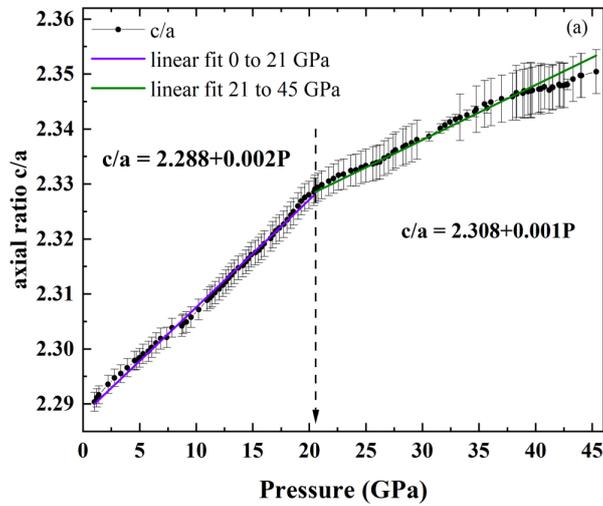


Figure 3.15: The axial ratio of  $\text{EuCoGe}_3$  as function of pressure. The change of the slope was observed around 21 GPa indicated with an arrow.

### 3.2.2 $\text{EuRhGe}_3$

Synchrotron powder XRD under pressure of  $\text{EuRhGe}_3$  was performed up to 35 GPa using helium as the pressure-transmitting medium. The contour map of diffraction intensities is pre-

sented in Fig 3.16. The pressure evolution of Bragg peak positions indicated two different phases,  $\text{EuRhGe}_3$  and gold. New peaks that appear above 25 GPa in the contour map (indicated by black arrows) were identified as rhenium from the gasket. Synchrotron XRD under pressure with neon transmission medium was also performed (see Appendix, C.0.1).

The lattice parameters of  $\text{EuRhGe}_3$  and gold were extracted from Rietveld refinement. The integrated diffraction peaks and refinement fitting at selected pressures are presented in Fig 3.13 (e-h). The extracted lattice parameters and refinement parameters are listed in table 3.2 with lattice parameters obtained by the DFT calculation.

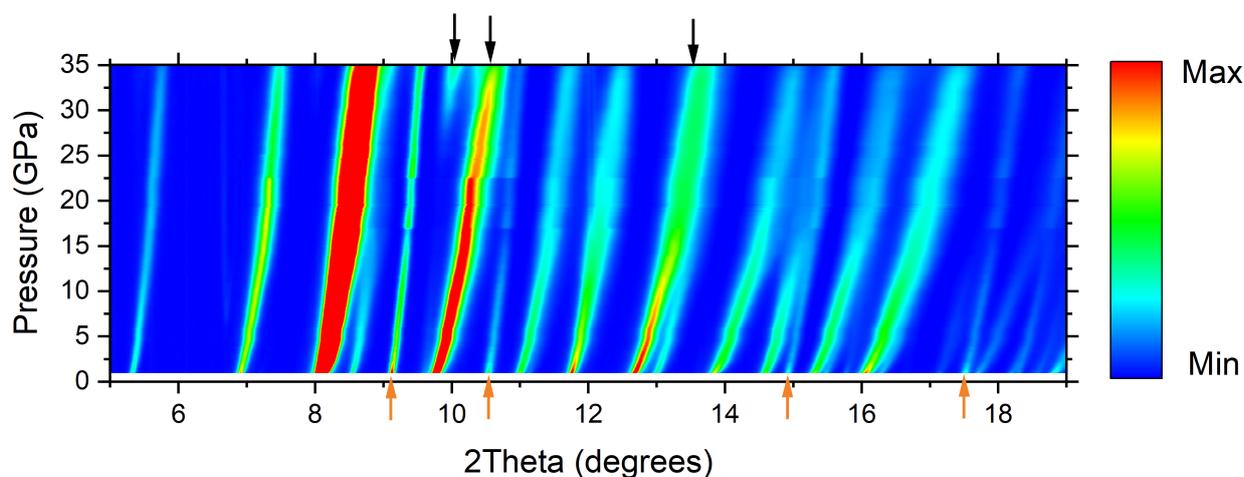


Figure 3.16: Contour map of synchrotron x-ray diffraction intensities in the pressure range from 1 to 35 GPa. The pressure evolution of Bragg peak positions contains  $\text{EuRhGe}_3$  (main phase), gold (standard material), and rhenium (gasket) which appears above 25 GPa. The black arrows (top) and yellow arrows (bottom) of the contour map represent the main peak positions of rhenium and gold respectively.

Similar to  $\text{EuCoGe}_3$ , the unit cell volume of  $\text{EuRhGe}_3$  exhibits a smooth contraction with increasing pressure without any structural transition up to 35 GPa, (See Fig. 3.17). The anisotropic compressibility along  $a$  and  $c$  lattice parameter is also observed in  $\text{EuRhGe}_3$ . Figure 3.18 shows the pressure evolution of axial ratio ( $c/a$ ). A change of slope can be seen around 13 GPa as indicated with an arrow. In the region  $P < 13$  GPa the value of the  $c/a$  linearly increases with pressure with a rate of  $0.003 \text{ GPa}^{-1}$ , then the rate decreases to  $0.001 \text{ GPa}^{-1}$  in the region  $P > 13$  GPa. This change in the  $c/a$  increase rate is ascribed to a change in compressibility along the  $a$ - and  $c$ -axis. The linear modulus of the  $c$ -axis increases considerably in the region  $P > 13$  GPa, which makes the  $c$ -axis less compressible and changes the slope of  $c/a$ . The observed linear modulus along  $c$ -axis, initially 181.6 GPa ( $P < 13$ ), changes to 302.8 GPa ( $P > 13$  GPa).

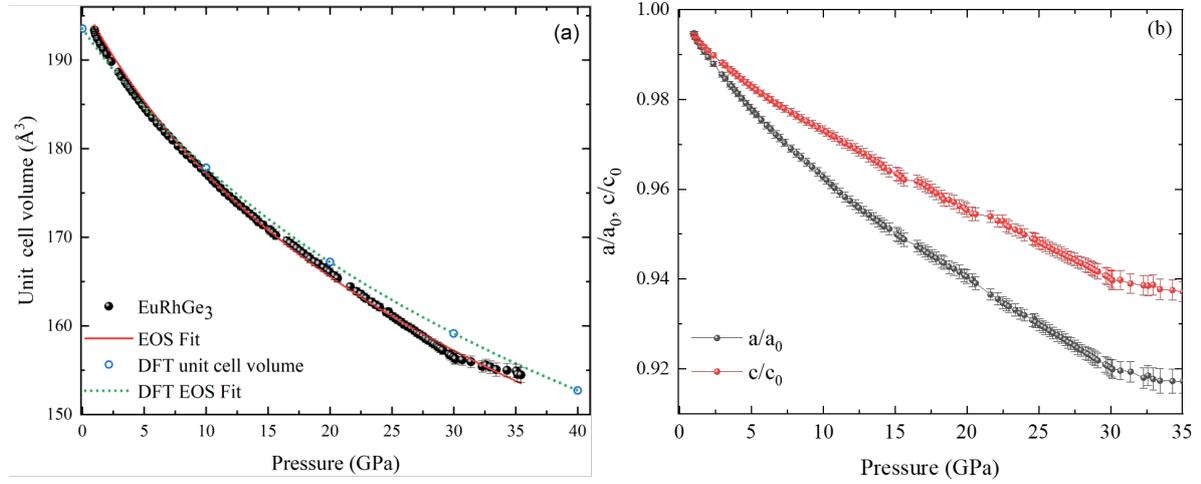


Figure 3.17: **(a)** EuRhGe<sub>3</sub> unit cell volume as function of pressure with 3<sup>rd</sup> order BM EOS Fit. DFT calculated unit volume and EOS Fit is also presented. **(b)** Normalized  $a$ ,  $c$  lattice parameters of EuRhGe<sub>3</sub> as a function of pressure.

Table 3.2: **Top:** Experimental lattice parameters, unit cell volume, and refinement parameters of EuRhGe<sub>3</sub> at selected pressures. **Bottom:** Lattice parameters and unit cell volume obtained by DFT calculation at various pressures.

Pressure	1 GPa	10 GPa	25 GPa	35 GPa
Lattice parameters and volume				
$a$ (Å)	4.389 (1)	4.249 (4)	4.103 (2)	4.04 (1)
$c$ (Å)	10.035 (3)	9.821 (9)	9.567 (6)	9.45 (2)
$V$ (Å <sup>3</sup> )	193.31 (8)	177.3 (3)	161.1 (1)	154.2 (8)
Refinement parameters				
$R_{WP}$	9.47	10.39	9.8	9.21
$R_{exp}$	10.11	9.55	9.98	10.52
$\chi^2$	0.88	1.17	0.96	0.77
GOF	0.95	1.06	0.98	0.88
Pressure	0 GPa	10 GPa	30 GPa	40 GPa
Lattice parameters and volume				
$a$ (Å)	4.3889	4.2547	4.0774	4.0104
$c$ (Å)	10.0478	9.8246	9.5731	9.4950
$V$ (Å <sup>3</sup> )	193.5451	177.8495	159.154	152.711

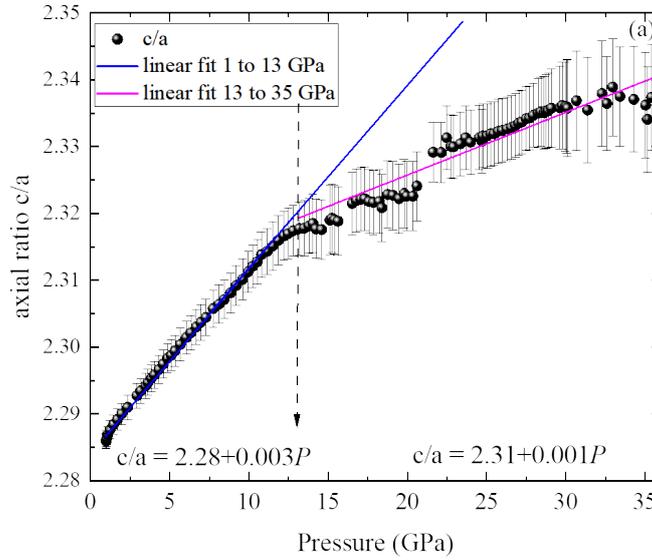


Figure 3.18: Pressure dependence of the axial ratio ( $c/a$ ) of  $\text{EuRhGe}_3$ . Straight lines emphasize linear behavior. To emphasize the change of slope, the linear fit of the low pressure region is extended into the high pressure region.

### 3.2.3 $\text{EuIrGe}_3$

Synchrotron powder XRD under pressure of  $\text{EuIrGe}_3$  was performed up to 40 GPa. Figure 3.19 presents the contour map of diffraction intensities in the pressure range from 0.5 to 34 GPa. The pressure evolution of Bragg peak positions indicates three different phases,  $\text{EuIrGe}_3$  (main phase), gold (standard material), and neon (pressure transmitting medium). New peaks appear above 28 GPa in contour map (indicated by black arrows) were identified as rhenium from the gasket.

Rietveld refinement was performed, and fitting for the diffractogram at various pressures is presented in Fig 3.20. The extracted lattice parameters and refinement parameters are listed in table 3.3 with the lattice parameters obtained by the DFT calculation. Since the goodness-of-fit (GOF) values from the Rietveld refinement turned out to be considerably high, the lattice parameters were also confirmed by LeBail method.

The unit cell volume of  $\text{EuIrGe}_3$  also exhibit a smooth contraction by applying pressure. An anisotropic compressibility between  $a$  and  $c$ -axis was observed in  $\text{EuIrGe}_3$  as well, presented in Fig 3.21. The pressure evolution of axial ratio ( $c/a$ ) shows a change of slope around 22 GPa. In the region  $P < 22$  GPa the value of the  $c/a$  linearly increases with pressure with a rate of  $0.002 \text{ GPa}^{-1}$ , then the rate decreases to  $0.0015 \text{ GPa}^{-1}$  in the region  $P > 22$  GPa. The linear EOS fitting was also performed on  $\text{EuIrGe}_3$ , which provides linear modulus  $M_0 = 358.8 \text{ GPa}$  ( $P < 22$  GPa), and  $M_0 = 421.53 \text{ GPa}$  ( $P > 22$  GPa). The linear modulus  $M_0$  of the  $c$ -axis increases

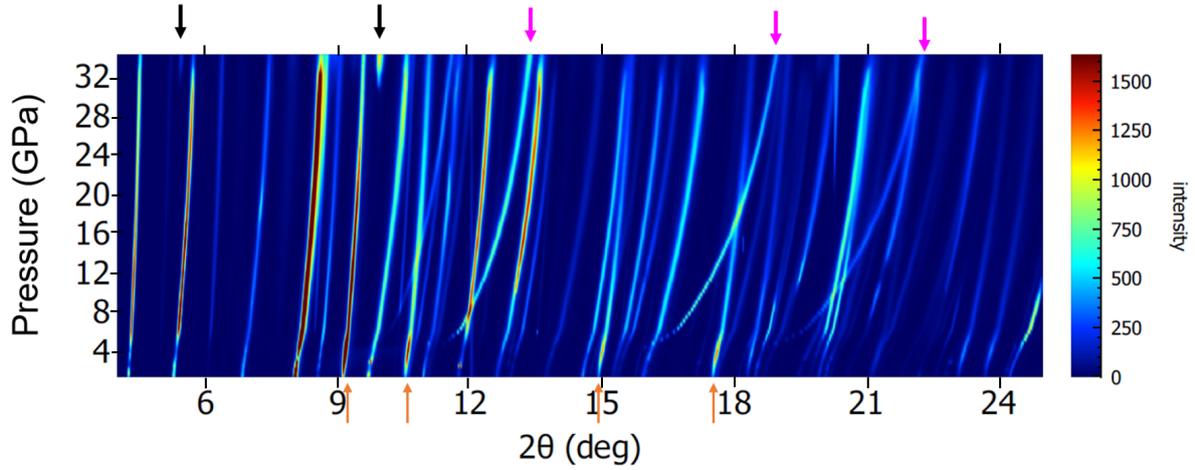


Figure 3.19: Contour map of synchrotron X-ray diffraction intensities in the pressure range of 0.5–34 GPa. The pressure evolution of Bragg peak positions contains  $\text{EuIrGe}_3$  (main phase), gold (standard material), neon (pressure-transmitting medium), and rhenium (gasket). The black arrows (top) represent rhenium, which appears around 30 GPa. The magenta arrow (top) represents neon as the pressure-transmitting medium, and the yellow arrows (bottom) represent gold Bragg peaks.

Table 3.3: **Top:** Experimental lattice parameters, unit cell volume, and refinement parameters of  $\text{EuIrGe}_3$  at selected pressures. **Bottom:** Lattice parameters and unit cell volume obtained by DFT calculation at various pressures.

Pressure	1 GPa	10 GPa	25 GPa	32 GPa
Lattice parameters and volume				
$a$ (Å)	4.4278 (18)	4.2802 (10)	4.1328 (12)	4.0788 (14)
$c$ (Å)	10.0441 (4)	9.8024 (16)	9.5843 (11)	9.5039 (12)
$V$ (Å <sup>3</sup> )	196.9187	179.58 (1)	163.71 (2)	158.12 (6)
Refinement parameters				
$R_{WP}$	38.10	48.22	46	44.1
$R_{exp}$	15.98	9.85	10.27	10.52
$\chi^2$	5.83	23.9	21.11	24
GOF	2.42	4.9	4.8	5.2
Pressure	0 GPa	10 GPa	30 GPa	40 GPa
Lattice parameters and volume				
$a$ (Å)	4.4142	4.2826	4.1078	4.0414
$c$ (Å)	10.039	9.8332	9.599	9.5258
$V$ (Å <sup>3</sup> )	195.61153	180.347405	161.97372	155.58407

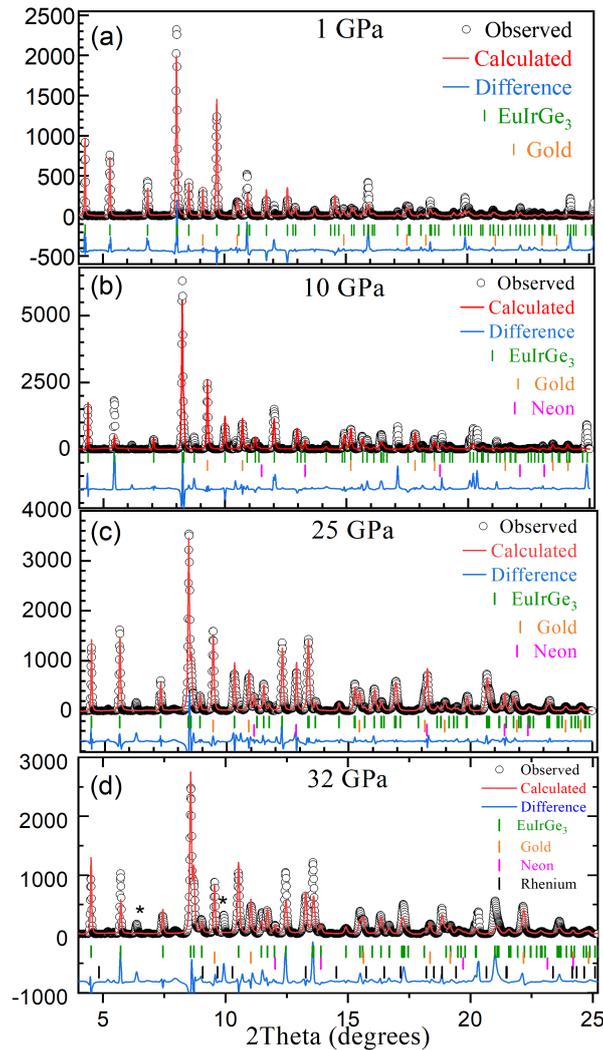


Figure 3.20: Integrated synchrotron XRD patterns of  $\text{EuIrGe}_3$  with the results of Rietveld refinement at (a) 1 GPa, (b) 10 GPa, (c) 25 GPa, and (d) 32 GPa. The vertical bars indicate Bragg peak positions of  $\text{EuIrGe}_3$  (green), gold (orange), neon (magenta) and rhenium (black). Some unindexed peaks are also visible in diffractogram shown with \*.

considerably, making the  $c$ -axis less compressible and resulting in a change of slope in  $c/a$ .

A few peaks were observed in diffractogram around 32 GPa, which does not belong to sample, gold, neon nor rhenium (gasket). To investigate the origin of these peaks, single crystal XRD under pressure was performed at CRISTAL beamline at SOLEIL synchrotron. The unit cell volume at different pressure extracted by *crysAlis pro* is presented in Fig 3.21(a). The observed lattice parameters as function of pressure are presented in Appendix C.2. The obtained lattice parameters and volume from single crystal XRD are consistent with the powder XRD data. The obtained structure at 40 GPa slightly deviates from tetragonal symmetry, though due

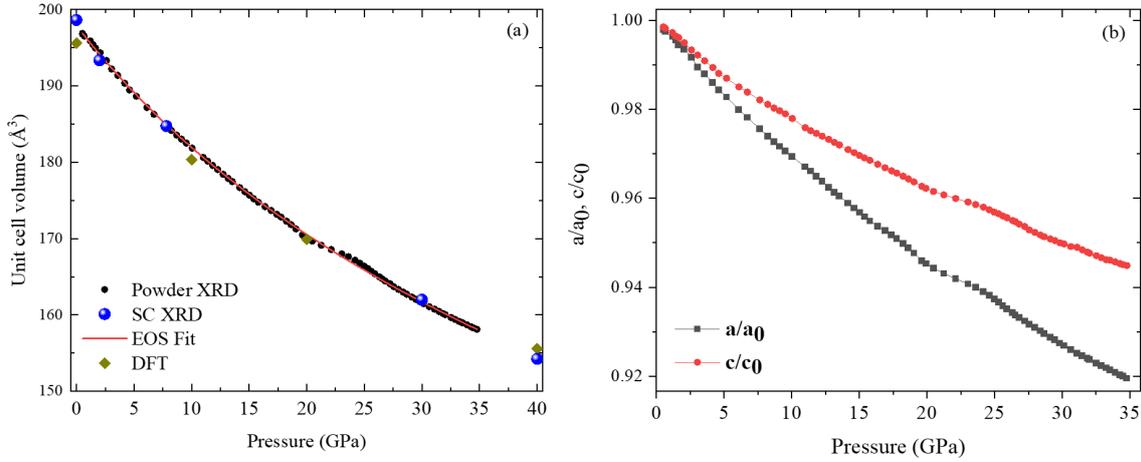


Figure 3.21: (a) Powder XRD, Single crystal XRD and DFT calculated unit cell volume of  $\text{EuIrGe}_3$  as function of pressure.  $3^{\text{rd}}$  order BM EOS fitting for powder XRD data is also provided. (b) Anisotropy along  $a$  and  $c$ - axis as function of pressure.

to the limited numbers of observed diffraction spots, it was not possible to determine the space group.

### 3.2.4 Comparison of XRD under pressure

X-ray diffraction (XRD) under pressure was conducted using a stainless steel gasket for  $\text{EuCoGe}_3$  and rhenium gaskets for  $\text{EuRhGe}_3$  and  $\text{EuIrGe}_3$ . All three compounds showed smooth contraction of unit cell volume without any structural change within the investigated pressure range. Bulk modulus ( $B_0$ ) and its pressure derivative  $B'_0$  of each compound were extracted by the EOS fitting of the pressure dependent unit cell volume. The extracted bulk modulus of  $\text{EuTGe}_3$  is in good agreement with isostructural  $\text{EuNiGe}_3$  [95]. The  $B_0$  and  $B'_0$  are summarized in table 3.4 with those obtained by the DFT calculation.

An anisotropic compressibility between  $a$  and  $c$  lattice parameters is presented in Fig. 3.22. A similar behaviours were observed in the DFT calculated crystal structures of  $\text{EuTGe}_3$ , as presented in Appendix B.0.1. The  $a$  lattice parameter is more compressed than that of  $c$ , which is opposite to the pressure response of centrosymmetric Eu-compounds with the  $\text{ThCr}_2\text{Si}_2$ -type ( $I4/mmm$ ) structure. In the  $\text{ThCr}_2\text{Si}_2$ -type structure,  $c$ -axis is more compressible than  $a$ -axis and pressure induced isostructural phase transition from tetragonal to the so-called collapsed tetragonal phase is observed in  $\text{EuCo}_2\text{As}_2$  [38] and  $\text{EuCo}_2\text{P}_2$  [40].

The pressure evolution of  $c/a$  shows linear increase with increasing pressure and exhibits a slope change at certain pressure in all three compounds. The change of slope was observed at

Table 3.4: The unit cell volumes, bulk modulus, and its first pressure derivative of  $\text{EuTGe}_3$  series and those obtained by the DFT calculations. The values of  $\text{EuNiGe}_3$  are taken from Ref. [95].

Compound	Unit cell volume ( $V_0$ )	Bulk modulus ( $B_0$ )	$B'_0$
$\text{EuCoGe}_3$ (XRD)	184.39 ( $\text{\AA}^3$ )	75.6	5.58
$\text{EuCoGe}_3$ (DFT)	178.84 ( $\text{\AA}^3$ )	98.9	4.16
$\text{EuRhGe}_3$ (XRD)	196.50 ( $\text{\AA}^3$ )	73	5.4
$\text{EuRhGe}_3$ (DFT)	193.54 ( $\text{\AA}^3$ )	97.43	4.61
$\text{EuIrGe}_3$ (XRD)	197.90 ( $\text{\AA}^3$ )	101.42	3.8
$\text{EuIrGe}_3$ (DFT)	195.61 ( $\text{\AA}^3$ )	103.13	4.27
$\text{EuNiGe}_3$ (XRD)	185.7 ( $\text{\AA}^3$ )	79	8.8

21 GPa, 13 GPa and 22 GPa in  $\text{EuCoGe}_3$ ,  $\text{EuRhGe}_3$ , and  $\text{EuIrGe}_3$ , respectively. The  $c/a$  slope change of all compounds are presented in Fig. 3.22. The two different colors represent two different pressure regions, where magenta represents the pressure range below the slope change, while green represents the higher pressure range than the slope change. The slope change in the axial ratio became evident due to its smaller scale compared to the change in lattice parameters. To investigate the reason behind the axial ratio deviation from linearity, linear EOS fitting was performed for all three compounds, below and above the kink pressure. The linear EOS fitting revealed that the  $c$ -axis linear modulus changes drastically at the kink pressure, making the  $c$ -axis less compressible and altering the slope of  $c/a$  evolution as a function of pressure. The change in linear modulus values for the compounds is presented in the respective sections.

### 3.3 Electric resistivity under pressure of $\text{EuIrGe}_3$

Pressure-induced superconductivities have been reported among ternary Ce-compounds that are isostructural to the  $\text{EuTGe}_3$  series. For example, the antiferromagnetic  $\text{CeTX}_3$ , in which pressure induced superconductivity was observed in  $\text{CeCoGe}_3$  with critical pressure  $T_c - 0.64$  K at  $P > 4.3$  GPa [96], in  $\text{CeIrGe}_3$   $T_c - 1.5$  K at  $P > 20$  GPa [21], and  $\text{CeIrSi}_3$   $T_c - 1.6$  K at  $P > 1.8$  GPa [20]. Although the emergence of pressure-induced superconductivity has not been reported in the  $\text{EuTX}_3$  series so far, an atypical pressure response was observed in  $\text{EuRhSi}_3$  [29], utilizing electric resistivity measurements under pressure up to 15 GPa.  $\text{EuRhSi}_3$  exhibits antiferromagnetic ground state with magnetic ordering temperature  $T_N = 49$  K. With increasing pressure, the  $T_N$  increases linearly up to 5 GPa. Upon applying higher pressure than 5 GPa, the  $T_N$  starts to decrease smoothly. This behavior shows a similar P-T phase diagram as observed in  $\text{CeTX}_3$  compounds.

As mentioned in introduction section, the pressure dependent electric resistivity measure-

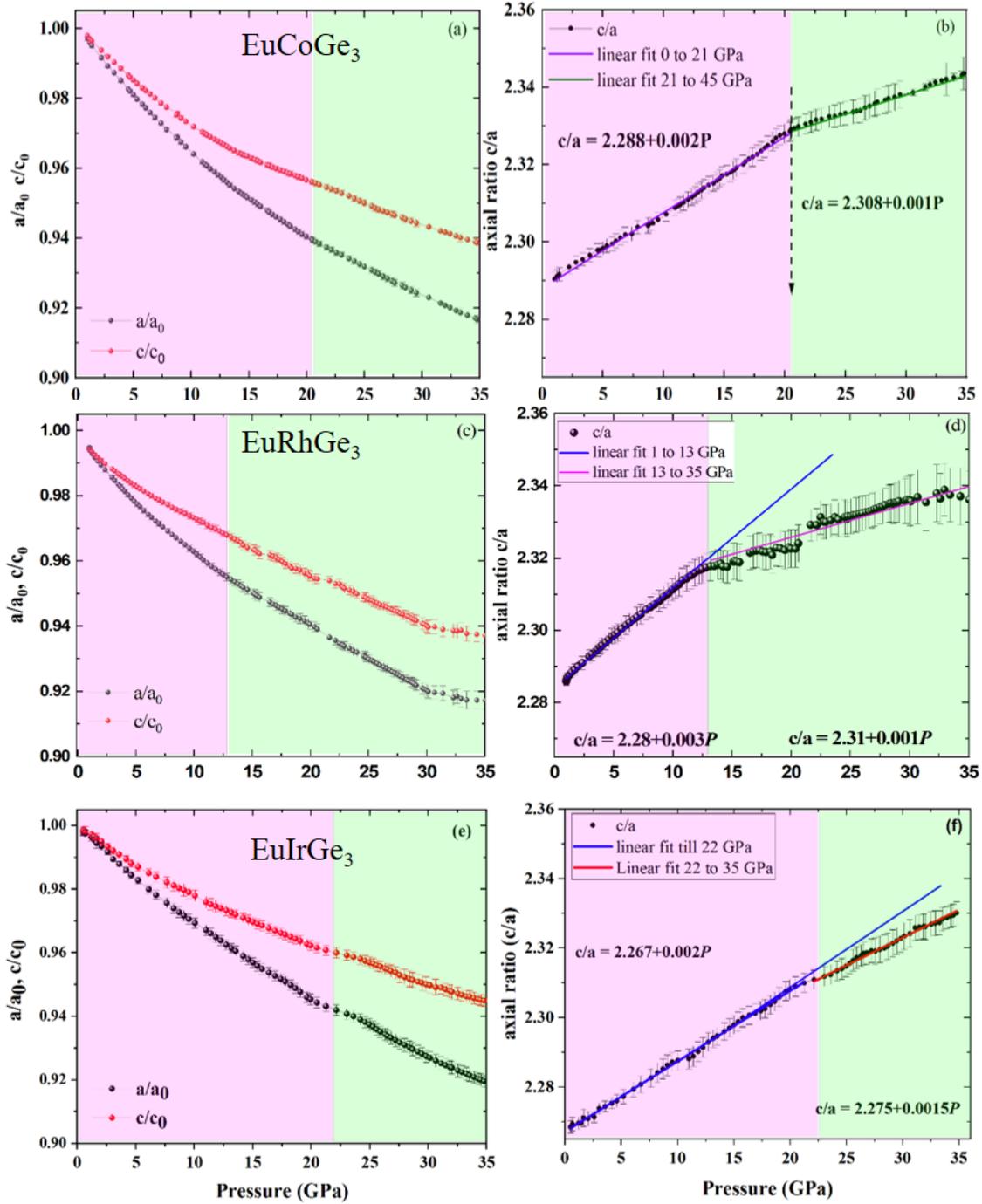


Figure 3.22: Relative pressure variations of the lattice parameters of  $\text{EuCoGe}_3$  (a),  $\text{EuRhGe}_3$  (c), and  $\text{EuIrGe}_3$  (e) with respect to the values at the lowest experimental pressure. Pressure dependence of the axial ratio of  $\text{EuCoGe}_3$  (b),  $\text{EuRhGe}_3$  (d), and  $\text{EuIrGe}_3$  (f). Straight lines emphasize linear behavior. To emphasize the change of slope, the linear fit of the low pressure region is extended into the high pressure region in few cases.

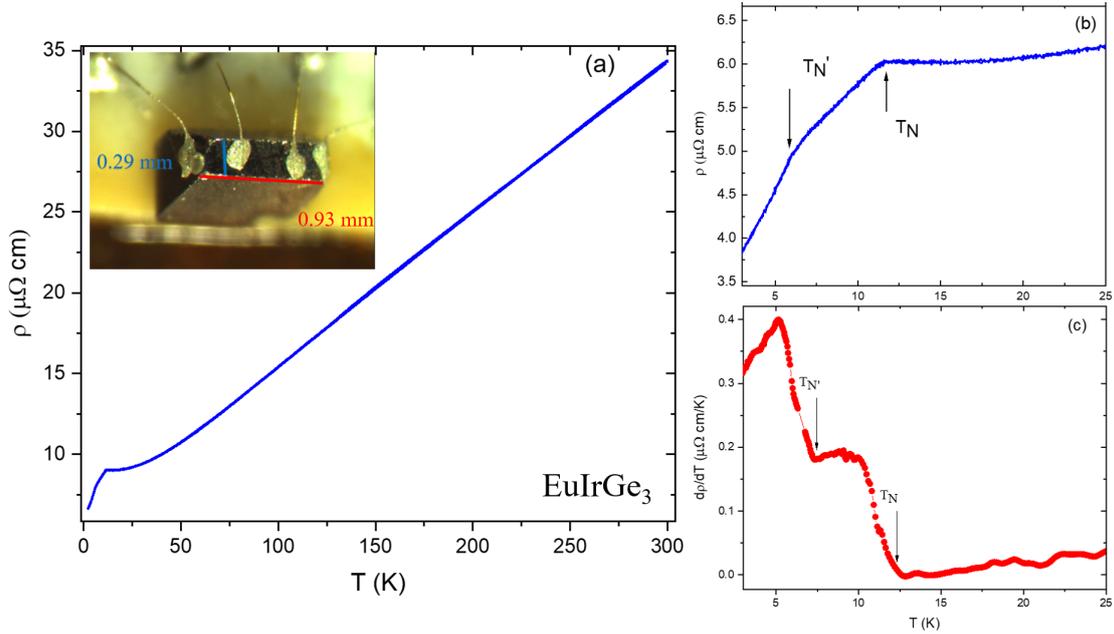


Figure 3.23: (a): Temperature dependent electric resistivity curve of  $\text{EuIrGe}_3$  measured by four probe method at ambient pressure. The inset shows a single crystal of  $\text{EuIrGe}_3$  with electric contacts. (b): Magnified view of the resistivity curve at low temperatures. The magnetic transition temperatures  $T_N$  and  $T_{N'}$ , which can be extracted from first or second order of temperature derivative of resistivity. (c): First order derivative of temperature dependent resistivity curve which was used to determine  $T_N$  and  $T_{N'}$ .

ments were also performed in  $\text{EuTGe}_3$  series to explore the pressure-induced superconductivity. The electric resistivity under pressure was measured up to 8 GPa [44]. However, no pressure induced superconductivity was observed in  $\text{EuTGe}_3$  ( $T = \text{Co, Rh and Ir}$ ) within the pressure range. Only a monotonous increase of  $T_N$  as function of pressure was observed in  $\text{EuCoGe}_3$ ,  $\text{EuRhGe}_3$  and  $\text{EuIrGe}_3$  with increase rate  $dT_N/dP = 1.0, 2.0, \text{ and } 2.2 \text{ K/GPa}$ , respectively. Similar results were obtained from pressure-dependent ac calorimetry in  $\text{EuCoGe}_3$  up to 10.4 GPa, which additionally indicated a pressure-driven moderate effective mass enhancement [50]. Hence, pressure higher than 10 GPa was necessary to study whether the phase diagram of  $\text{EuTGe}_3$  exhibits a conventional type or the Doniach-type like  $\text{EuRhSi}_3$ , as presented in Fig.1.4.

Figure 3.23 presents the temperature dependent electrical resistivity curve in the single crystal of  $\text{EuIrGe}_3$  at ambient pressure. The resistivity curve shows metallic behaviour with kinks at magnetic ordering temperatures  $T_N$  at 12.3 K and successive magnetic transition and  $T_{N'}$  at 7.5 K. The temperature behaviour of resistivity curve and obtained magnetic transition temperatures were consistent with the reported result in Ref [51]. Small pieces of single crystals for electric resistivity measurements under pressure were cut out from the same sample.

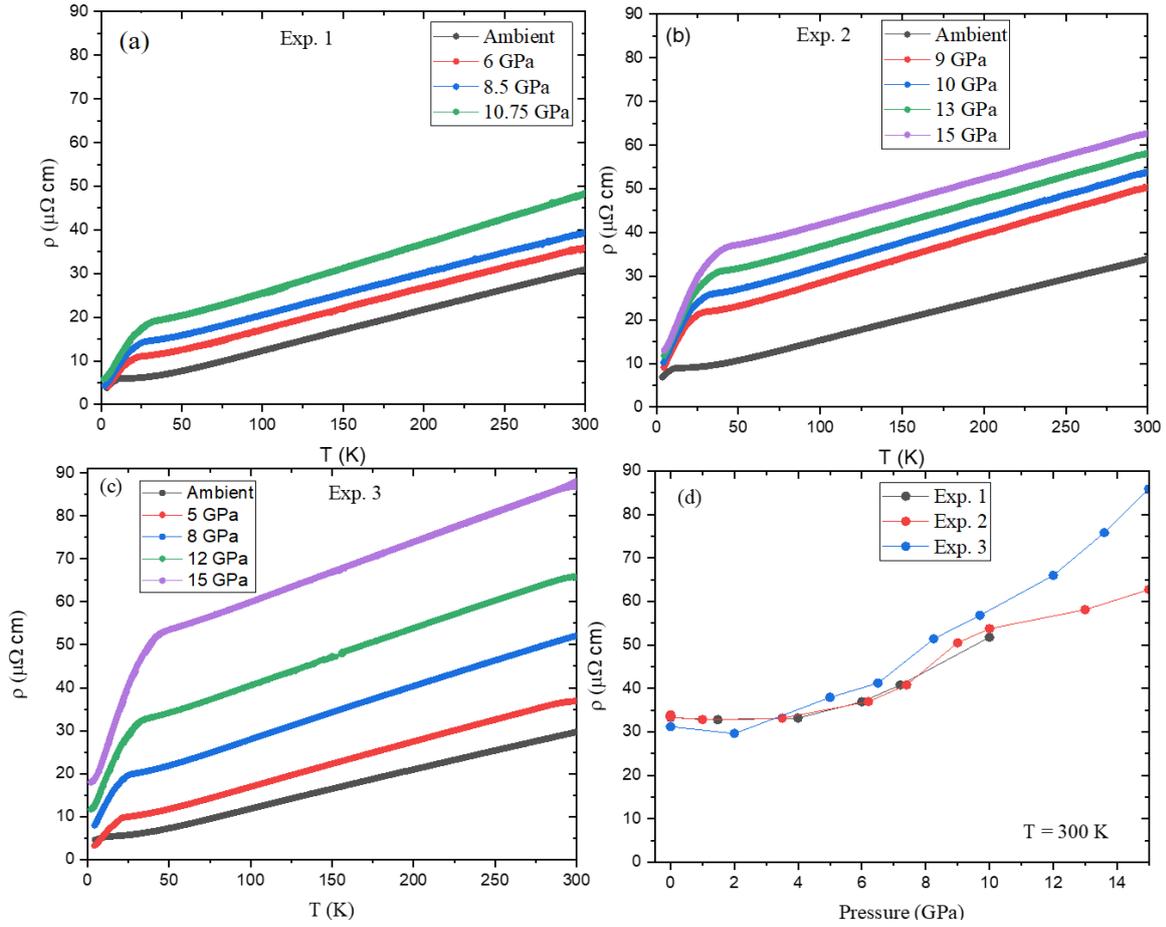


Figure 3.24: Temperature dependent electric resistivity of  $\text{EuIrGe}_3$  under pressure. (a): Exp. 1 (b): Exp. 2, (c): Exp. 3, and (d): Resistivity at 300 K of three samples as function of pressure.

Electric resistivity of  $\text{EuIrGe}_3$  was measured up to 15 GPa utilizing a DAC. Electric resistivity under pressure was performed up to 10 GPa in experiment 1 (Exp. 1). The temperature-dependent electric resistivity curves at selected pressures are presented in Fig. 3.24 (a). Experiments 2 and 3 were conducted up to 15 GPa, and selected curves are presented in Fig. 3.24 (b, c). The resistivity curves of the experiments 1 and 2 show similar pressure behavior, while experiment 3 shows an increase of the residual resistivity ( $\rho_0$ ) with increasing pressure and tends to have larger increase of resistivity with pressure in whole temperature range compared with exp.1, exp.2. The measurement conditions in all three experiments were kept similar. The increase of  $\rho_0$  as a function of pressure reflects an increase in static defects, which may originate from inhomogeneous valence fluctuations under pressure.

The electric resistivity as function of pressure at 300 K are presented in Fig. 3.24 (d). With increasing pressure, resistivity shows almost no change till 6 GPa, reproducing the reported

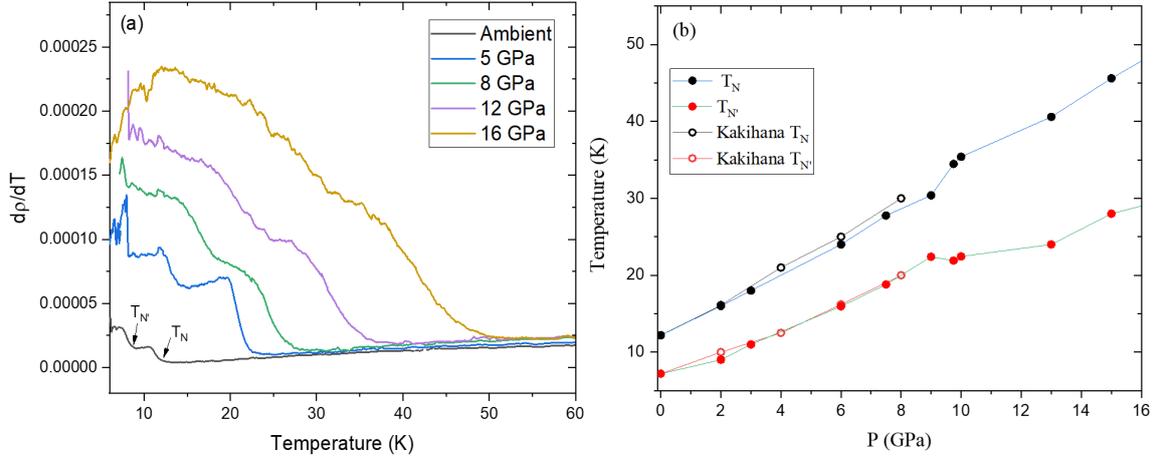


Figure 3.25: (a): First order derivative of resistivity curve of  $\text{EuIrGe}_3$  (Exp. 3) at different pressures. Magnetic ordering temperature  $T_N$  and  $T_{N'}$  are extracted from resistivity derivative, presented by arrows at ambient pressure curve. (b): Pressure evolution of magnetic ordering temperatures  $T_N$  and  $T_{N'}$  of  $\text{EuIrGe}_3$  compared with the reported values in Ref. [44].

electric resistivity as a function of pressure [44]. When pressure higher than 6 GPa was applied, the electric resistivity starts to increase. Between experiments 2 and 3, the resistivity starts to deviate from each other around 15 GPa. A similar increase in resistivity under pressure at 300 K was observed in isostructural  $\text{EuRhSi}_3$  [29]. The increases of the resistivity at low temperatures and the  $T_N$  are proposed to be related with the enhancement of the RKKY interaction with increasing pressure [44]. Note that the temperature-dependent resistivity curves were only measured at selected pressure, while the resistivity change at 300 K with pressure were recorded at various pressure points.

The pressure evolution of  $T_N$  and  $T_{N'}$  is in good agreement with earlier studies [44]. The different residual resistivities at low temperatures were observed in experiment 2 and 3, while  $T_N$  and  $T_{N'}$  values are same for all three experiments at respective pressure. The observed  $T_N$  increases linearly as function of pressure with  $dT_N/dP = 2.25 \pm 0.04$  K/GPa. The successive transition temperature ( $T_{N'}$ ) also increases linearly as function of pressure with rate  $dT_{N'}/dP = 1.39 \pm 0.06$  K/GPa. A similar monotonous increase of  $T_N$  as function of pressure and rate  $dT_N/dP = 1.8$  K/GPa was observed in  $\text{EuNiGe}_3$  [49].

# Chapter 4

## Thesis summary and outlook

### 4.1 Summary of this Thesis

The pressure evolution of electronic and crystal structures and pressure-temperature (P-T) phase diagrams of  $\text{Eu}T\text{Ge}_3$  ( $T = \text{Co}, \text{Rh}$  and  $\text{Ir}$ ) with the  $\text{BaNiSn}_3$ -type structure were studied by using complimentary experimental techniques in this thesis. HERFD XAS was utilized to study the pressure evolution of the electronic structure, and powder/single-crystal XRD was used to observe the crystal structural changes as a function of pressure. The temperature dependent electrical resistivity of  $\text{EuIrGe}_3$  were measured under pressure. The results from each measurement are briefly summarized in this chapter. By combining the results from three different experimental methods, the P-T phase diagram of  $\text{EuIrGe}_3$  is proposed.

#### 4.1.1 Pressure evolution of the electronic structure

Pressure dependent HERFD XAS spectra of  $\text{EuCoGe}_3$  were measured at the Eu  $L_3$ , Co  $K$ , and Ge  $K$  edges. The Eu  $L_3$  spectra exhibited the dominant  $\text{Eu}^{2+}$  contribution at the lowest pressure, and a spectral intensity transfer from  $\text{Eu}^{2+}$  to  $\text{Eu}^{3+}$  was observed with increasing pressure. The obtained pressure evolution of the mean Eu valence in  $\text{EuCoGe}_3$  changes from  $2.20 \pm 0.02$  at 4 GPa to  $2.31 \pm 0.02$  at 50 GPa. No spectral changes were observed at the Co  $K$  and Ge  $K$  edges, suggesting that the pressure evolution of Eu valence involves intra-atomic charge transfer from Eu 4f to Eu 5d, but no contribution from Ge and Co ions.

The pressure-dependent Eu  $L_3$  spectra of  $\text{EuRhGe}_3$  showed similar pressure response as  $\text{EuCoGe}_3$ . However, the spectral change is larger than  $\text{EuCoGe}_3$ . The obtained mean Eu valence varies from  $2.13 \pm 0.02$  at ambient pressure to  $2.40 \pm 0.02$  around 40 GPa.

The Eu  $L_3$  HERFD XAS spectra of  $\text{EuIrGe}_3$  showed a similar pressure response as  $\text{EuRhGe}_3$ .

The obtained mean Eu valence changes from  $2.12 \pm 0.02$  at ambient pressure to  $2.45 \pm 0.02$  around 45 GPa. The pressure dependence of Eu  $L_3$  XAS spectrum was also measured in transmission mode at 300 and 4 K. The observed spectra at both temperatures showed the similar pressure change as HERFD XAS spectra. The Ir  $L_3$  spectra showed energy shift towards higher energy with increasing pressure. The Ge K spectra showed the shift of spectral intensity from low to high energy peaks derived from Ge ions at 4b and 2a Wyckoff positions respectively with increasing pressure.

The pressure evolutions of the obtained mean Eu valences in three compounds are summarized in Fig. 4.1. The mean Eu valence showed the smallest change in  $\text{EuCoGe}_3$  and the largest change in  $\text{EuIrGe}_3$ . The results indicate that different pressure responses of the Eu valence among three compounds are originating from different natures among 3d (localized), 4d and 5d (less localized) transition metal orbitals.

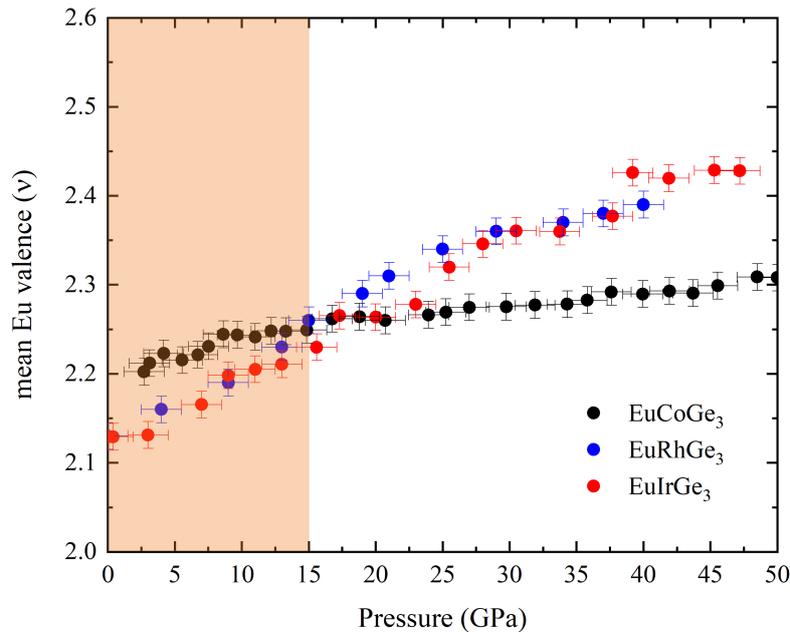


Figure 4.1: Mean Eu valence as function of pressure of  $\text{EuCoGe}_3$ ,  $\text{EuRhGe}_3$  and  $\text{EuIrGe}_3$ . Shaded region is showing the coexisting intermediate valence and antiferromagnetism.

#### 4.1.2 Pressure evolution of crystal structure

All three compounds show a smooth contraction of unit cell volume, preserving crystal symmetry up to 40 GPa. Anisotropic compression between the  $a$  and  $c$  lattice parameters was observed, where the  $a$  lattice parameter showed a larger change compared with the  $c$  lattice parameter. This pressure behaviour is in contrast to that of centrosymmetric  $\text{Eu122}$ -systems. In

general, the  $c$  lattice parameter is more compressed than the  $a$  lattice parameter under pressure and in some cases a structural transition to the collapse tetragonal phase occurs. The axial ratio ( $c/a$ ) increases linearly as a function of pressure in the  $\text{EuTGe}_3$  series. A change in the slope of the axial ratio was observed around 21 GPa, 13 GPa, and 22 GPa in  $\text{EuCoGe}_3$ ,  $\text{EuRhGe}_3$ , and  $\text{EuIrGe}_3$ , respectively, as presented in Fig. 4.2 (a).

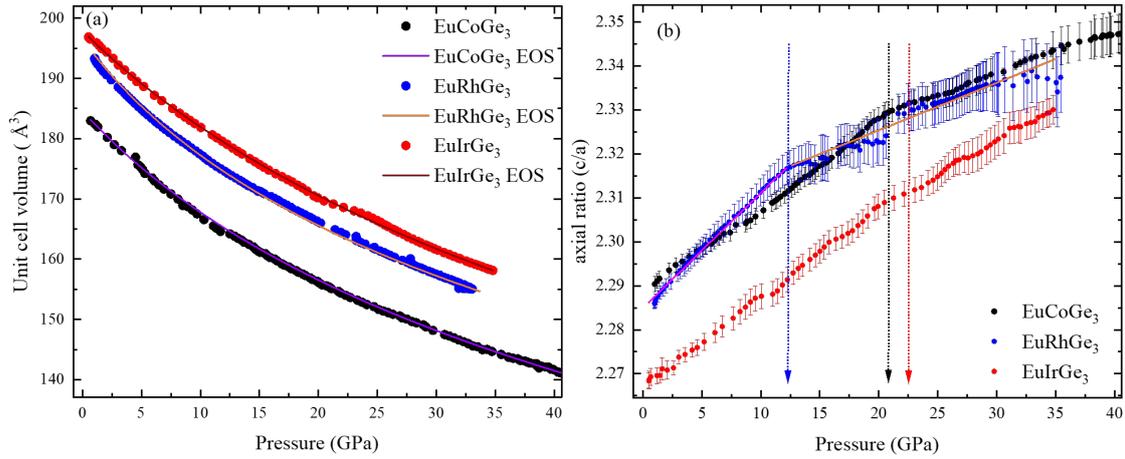


Figure 4.2: (a) Unit cell volume as function of pressure for all three compounds with respective EOS fitting. (b) The axial ratio ( $c/a$ ) for  $\text{EuTGe}_3$ , showing the kink at 21 GPa, 13 GPa and 22 GPa in  $\text{EuCoGe}_3$ ,  $\text{EuRhGe}_3$  and  $\text{EuIrGe}_3$  respectively. The linear fit are presented for  $\text{EuRhGe}_3$ .

The Eu valence as a function of pressure shows a change in slope around 9 GPa in  $\text{EuCoGe}_3$  and 25 GPa in  $\text{EuRhGe}_3$ , while no change in unit cell volume was observed at these pressures. Hence, no direct correlation between unit cell volume and Eu valence was found in the non-centrosymmetric  $\text{EuTGe}_3$  series, contrasting with the behavior observed in the  $\text{EuT}_2\text{X}_2$  type centrosymmetric system.

### 4.1.3 Electric resistivity under pressure

Pressure-induced superconductivities have been reported among ternary Ce-compounds that are isostructural to the  $\text{EuTGe}_3$  series, such as  $\text{CeCoGe}_3$  and  $\text{CeIrGe}_3$ . To investigate pressure-induced superconductivity and the pressure-temperature phase diagram, electric resistivity measurements of  $\text{EuIrGe}_3$  were performed under pressure up to 15 GPa. No pressure-induced superconductivity was observed in  $\text{EuIrGe}_3$  within the pressure and temperature ranges of the experiments. The pressure change of  $T_N$  and  $T_N'$  showed good agreement with earlier studies

[44]. The resistivity at 300 K exhibited negligible change up to 6 GPa, while upon increasing pressure beyond 6 GPa, electric resistivity started to increase, this phenomenon was also observed in a few isostructural compounds. This behavior was proposed due to increasing c-f hybridization or increasing RKKY interaction as function of pressure.

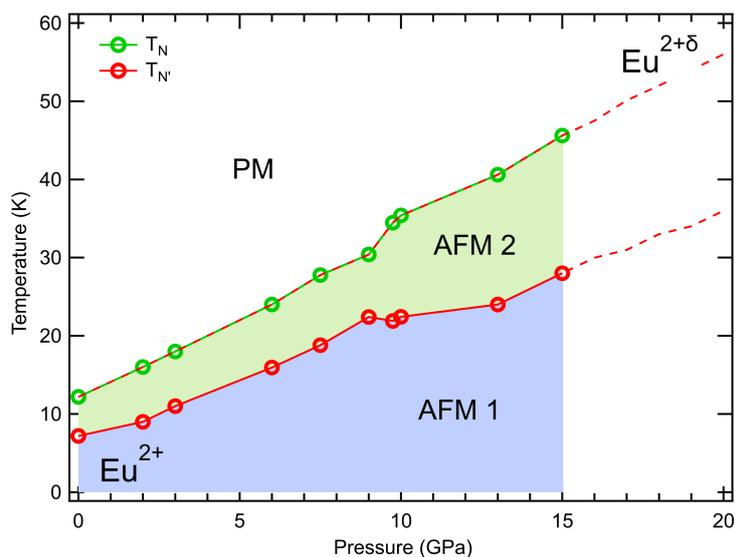


Figure 4.3: Pressure-Temperature phase diagram of  $\text{EuIrGe}_3$ .

The magnetic ordering temperatures ( $T_N$  and  $T_{N'}$ ) increases monotonically as function of pressure. The proposed P-T phase diagram of  $\text{EuIrGe}_3$  up to 15 GPa is presented in Fig 4.3.

# Appendix A

## Hydrostatic or quasi-hydrostatic pressure

In order to specify the meanings of mean pressure, deviatoric stress tensor, hydrostatic pressure, and uniaxial pressure, one refers to the time independent stress tensor  $[\sigma_{ij}]$ . The component of the stress tensor is written as;

$$\sigma = \begin{bmatrix} \sigma_{11} & \sigma_{12} & \sigma_{13} \\ \sigma_{21} & \sigma_{22} & \sigma_{23} \\ \sigma_{31} & \sigma_{32} & \sigma_{33} \end{bmatrix}$$

The subscripts  $ij$  refer to the axes of an orthogonal three-dimensional coordinate system of arbitrary or symmetry-adopted orientation. The scalar components  $\sigma_{ij}$  represent the magnitude of the internal forces per unit area. The first index refers to the direction of stress acting on a plane (normal or tangential) and the second index refers to the direction of the normal of the plane on which the stress acts [55].

Mean pressure defines as the negative of average of three diagonal stress tensors:

$$P(r) = -\frac{1}{3}[\sigma_{11}(r) + \sigma_{22}(r) + \sigma_{33}(r)]. \quad (\text{A.1})$$

Deviatoric stress tensor is defined as anisotropic forces within a sample. All other stresses, i.e. the shear stresses, are given by the zero-trace stress tensor  $[\tau_{ij}]$ :

$$\tau_{ij}(r) = \sigma_{ij}(r) - \delta_{ij}P(r). \quad (\text{A.2})$$

Hydrostatic pressure is characterized by isotropic normal stresses and zero deviatoric stresses, formally written as

$$\begin{aligned}
 -P(r) &= \sigma_{11} = \sigma_{22}(r) = \sigma_{33}(r) \\
 \tau_{ij}(r) &= 0.
 \end{aligned}
 \tag{A.3}$$

These equations provides a point in space with hydrostaticity. All other conditions can be considered as inhomogeneous stress (non-hydrostaticity). One more commonly occurring term is quasi-hydrostatic, the complete meaning of quasi-hydrostatic stress cannot be specified qualitatively and quantitatively. The term may also refer to a transient state of deviatoric or inhomogeneous stress.

### A.0.1 Ruby fluorescence spectra fitting

Ruby fluorescence pressure calibration method uses the two distinguished R1 and R2 peaks. However, when the pressure departs from hydrostaticity in the sample space, the peak widths of the R1 and R2 lines increase, and both lines become inseparable.

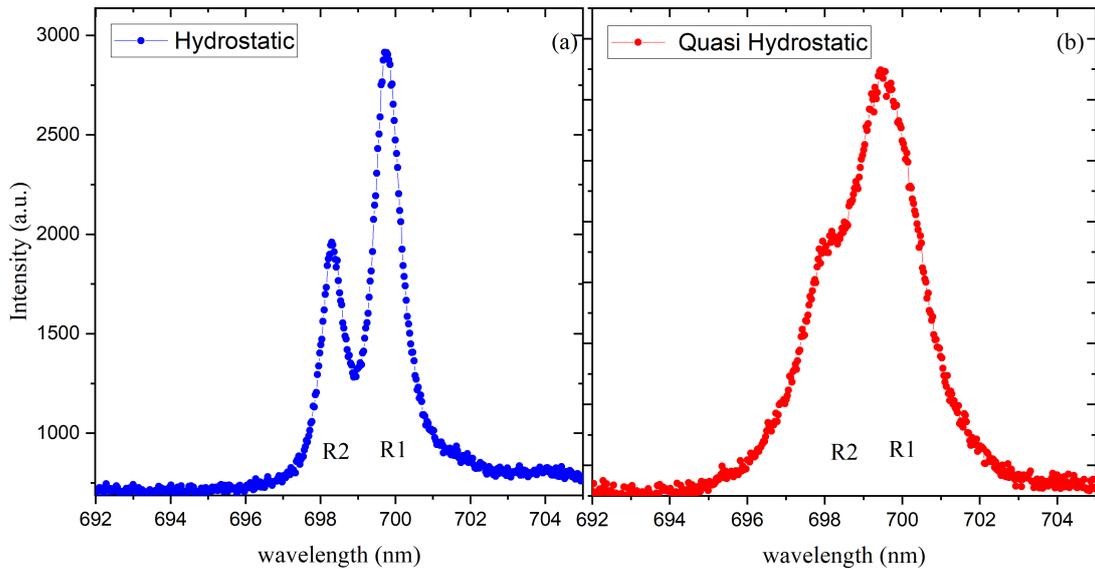


Figure A.1: Ruby fluorescence spectra at 14 GPa. **(a)** hydrostatic pressure. **(b)** quasi or non-hydrostatic pressure.

Figure A.1 presents the fluorescence spectra at 14 GPa, visualizing the difference between hydrostatic and non-hydrostatic cases. To determine the peak shifts for pressure calibration, the fluorescence spectra are fitted using three different functions Gaussian, Lorentzian, and Vogit. In case of hydrostatic pressure, the fitting with three different functions provides similar results. While non-hydrostatic case, the results of fittings show some deviation. The results of three

different fitting are presented in Fig. A.2 and the obtained values from the fitting are presented in table A.1.

Table A.1: Various peak fittings and corresponding pressure for quasi or non-hydrostatic case. Pressure is calculated by using equation 2.1.

Fitting Type	R1 Peak Position	R1 FWHM	R2 Peak Position	R2 FWHM	Pressure
Gaussian	699.557 nm	2.266	697.626 nm	1.624	14.263 GPa
Lorentzian	699.593 nm	2.048	697.932 nm	1.541	14.367 GPa
Voigt	699.594 nm	2.103	697.885 nm	1.517	14.372 GPa

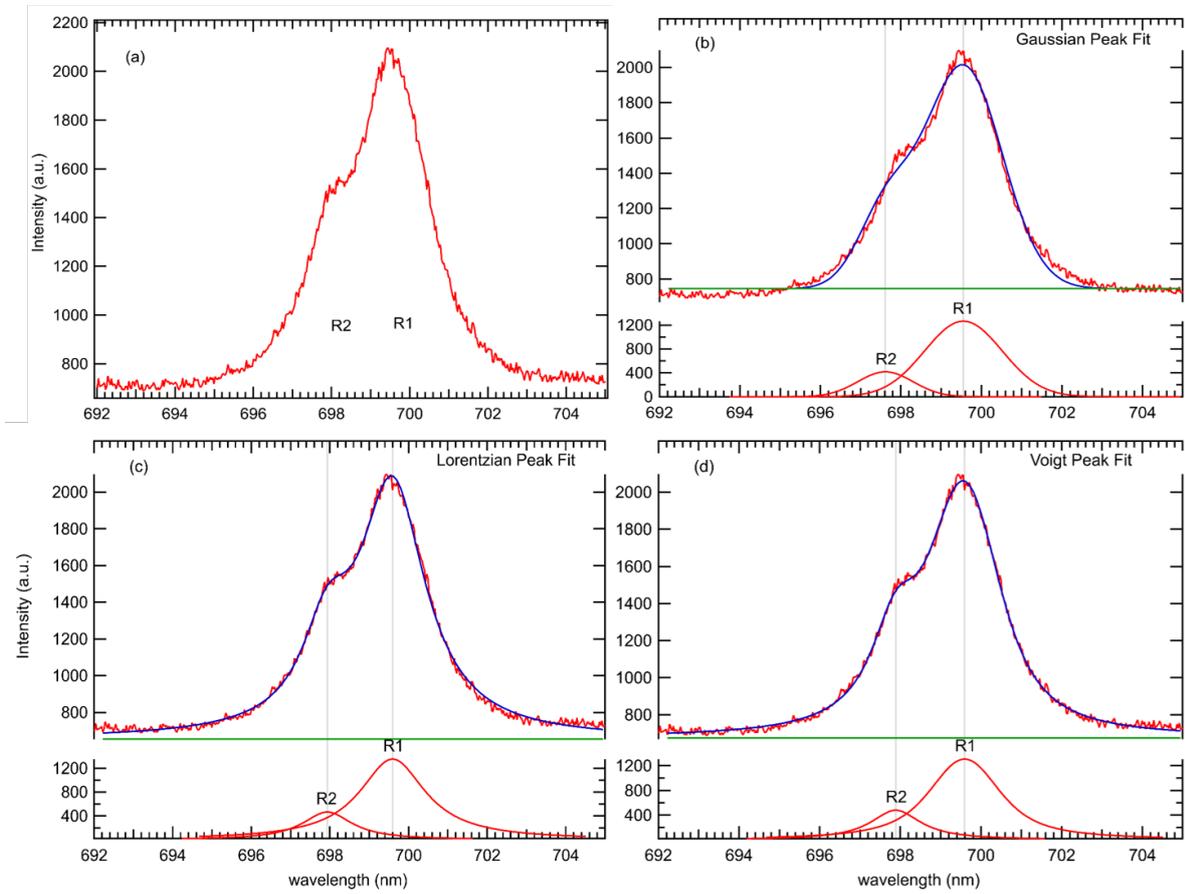


Figure A.2: (a) Ruby fluorescence spectrum under quasi hydrostatic pressure at 14 GPa. The R1 and R2 peaks fitted by using (b) Gaussian functions, (c) Lorentzian functions, and (d) Voigt functions.

# Appendix B

## DFT calculations and technical details of pressure cell

### B.0.1 DFT calculation

The pressure evolutions of the crystal structure of  $\text{EuCoGe}_3$ ,  $\text{EuRhGe}_3$ , and  $\text{EuIrGe}_3$  were also studied theoretically by using the Quantum ESPRESSO DFT package [86; 87]. More details about DFT calculations is presented in chapter 3. Figure B.1 illustrates the density of states (DOS) calculated of  $\text{EuTGe}_3$  by DFT + U ( $U = 3.8$  eV) are presented for few selected pressures.

The total DOS at 0 GPa has a quasi-gap like low-DOS region located  $\sim 1.5$  eV above  $E_F$ , though it completely disappears at 50 GPa. DFT calculated unit cell volumes are in good agreement with the XRD extracted volumes as function of pressure, as presented in respective sections in chapter 3. The calculated crystal structures also show anisotropic compressibility along  $a$  and  $c$ -axis similar as observed in XRD. The  $a$ -axis exhibits larger compressibility than  $c$ -axis. Figure B.2 shows the anisotropic compressibility along  $a$  and  $c$ -axis.

### B.0.2 Technical details of pressure cell

Here, a few technical details of high pressure cell which were not explained in the main text are presented. The section contains the general introduction of piston-cylinder cell, and gasket strength testing.

#### Piston-cylinder cell

The working principle of the piston-cylinder cell involves applying pressure to the sample by moving the piston within the cylinder. The cell typically consists of a metal cylinder made of

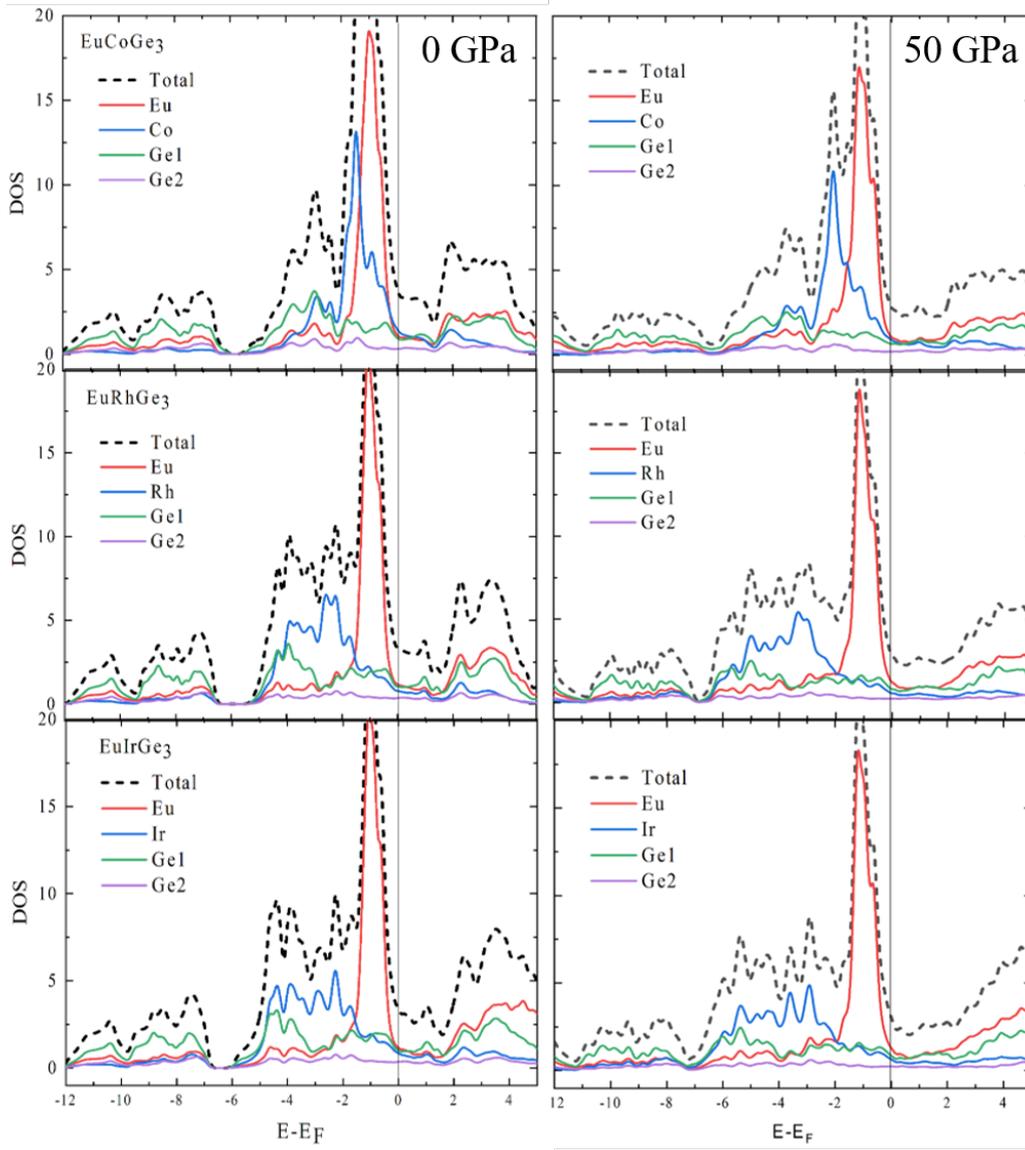


Figure B.1: DOS at ambient pressure (left) and highest pressure (right). (Top)  $\text{EuCoGe}_3$ , (Middle)  $\text{EuRhGe}_3$  and (Bottom)  $\text{EuIrGe}_3$ .

NiCrAl alloy/stainless steel, piston is usually made of tungsten carbide, which can withstand the high pressures involved. Piston-cylinder cell have advantage over DAC for bigger sample space, while pressure range is limited up to 3 GPa. The accessibility of the sample space and the capability to measure multiple samples are among the biggest advantages. Its flexibility, and compatibility with various measurement techniques make it a valuable apparatus for studying phase transitions, electronic properties, and magnetic behavior. Figure B.3 presents the images of assembled piston-cylinder cell with its cross-section view and sample loading mechanism.

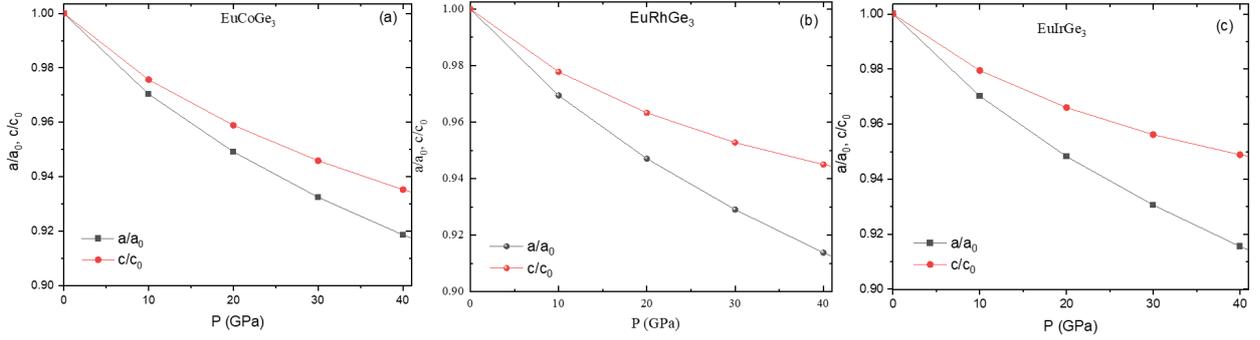


Figure B.2: Relative pressure variation of the DFT calculated lattice parameters of (a) EuCoGe<sub>3</sub>, (b) EuRhGe<sub>3</sub>, and (c) EuIrGe<sub>3</sub>.

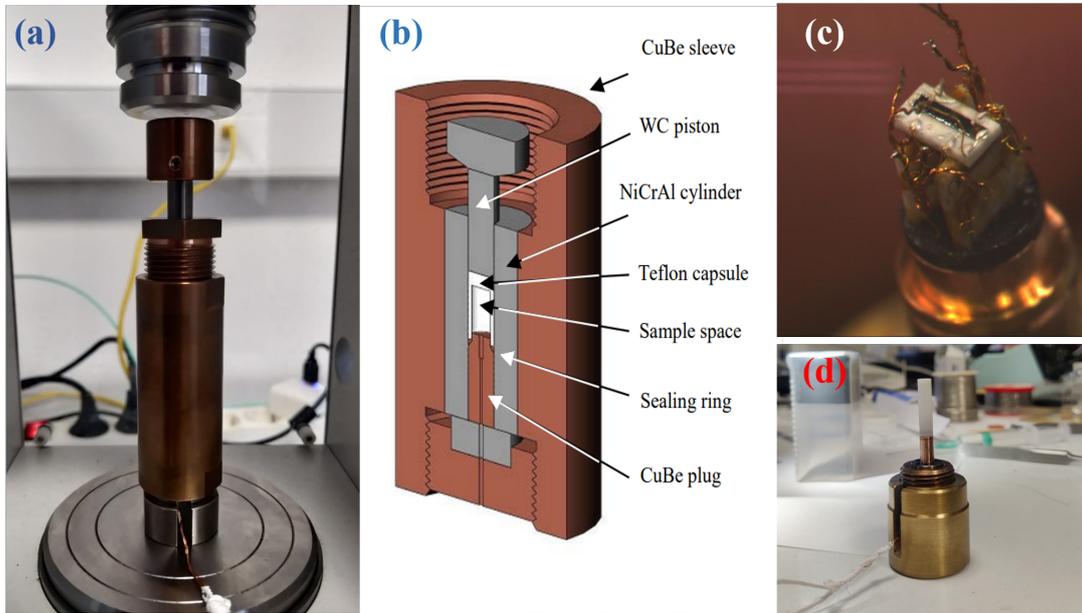


Figure B.3: (a) Assembled Piston cylinder cell in hydraulic press. (b) Illustration of the cross section of a piston-cylinder-type NiCrAl pressure cell, Taken from [97]. (c) Sample connected with the outer connections, sample is glued to ceramic bases. (d) Samples are loaded inside a 20 mm long and 5 mm diameter teflon tube.

### Gasket strength testing

When pressure is applied to the gasket enclosed within the DAC, the gasket material undergoes plastic deformation due to the high compressive forces. This deformation can lead to the formation of indentations or impressions on the surface of the gasket. The pre-indentation of the gasket by the diamond anvils plays a significant role in ensuring the stability and reliability of pressure experiments, while also offering insights into the load-bearing characteristics of the

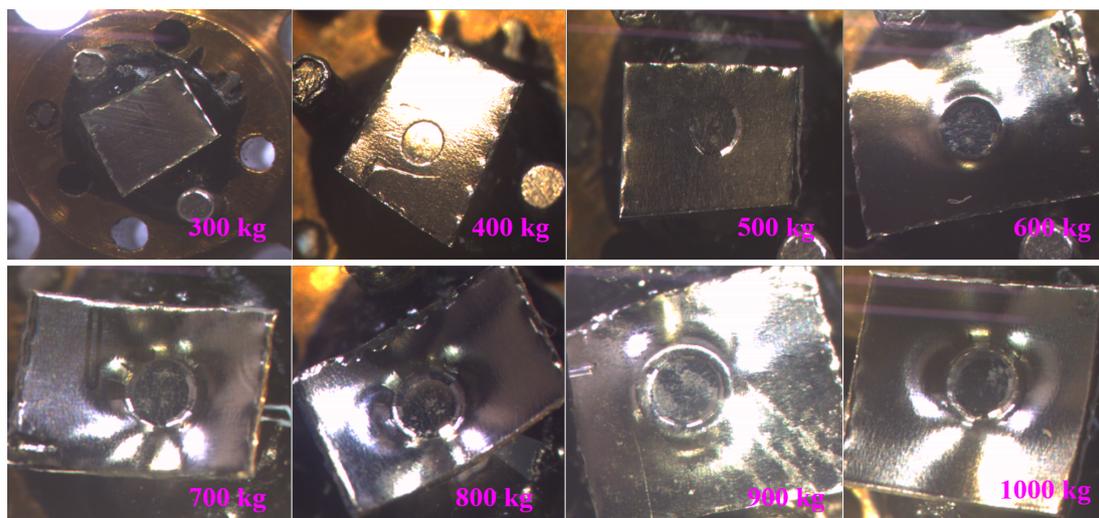


Figure B.4: V56004 Stainless steel gasket strength testing. No diamond indentation was observed till 300 Kg load, around 500 Kg gasket started to show indentation. Upon applying load higher than 600Kg gasket started to deform and indentation was observed.

Table B.1: Various gasket materials and their indentation thickness dependence on loads and diamond culet size.

Gasket Material	Load	Initial t ( $t_i$ )	1.1 mm culet	0.9 mm culet
			Indented ( $t_f$ )	Indented ( $t_f$ )
V56004 - Stainless steel	300 kg	250 $\mu\text{m}$	250 $\mu\text{m}$	
	400 kg	250 $\mu\text{m}$	248 $\mu\text{m}$	
	500 kg	250 $\mu\text{m}$	222 $\mu\text{m}$	
	600 kg	250 $\mu\text{m}$	157 $\mu\text{m}$	
	700 kg	250 $\mu\text{m}$	132 $\mu\text{m}$	
	800 kg	250 $\mu\text{m}$	110 $\mu\text{m}$	
	900 kg	250 $\mu\text{m}$	95 $\mu\text{m}$	
	1000 kg	250 $\mu\text{m}$	91 $\mu\text{m}$	
MP35N - Stainless steel	500 kg	200 $\mu\text{m}$		109 $\mu\text{m}$
	550 kg	200 $\mu\text{m}$		80 $\mu\text{m}$
	600 kg	200 $\mu\text{m}$		70 $\mu\text{m}$
	800 kg	200 $\mu\text{m}$	85 $\mu\text{m}$	
	850 kg	200 $\mu\text{m}$	78 $\mu\text{m}$	
	900 kg	200 $\mu\text{m}$	70 $\mu\text{m}$	
Inconel	800 kg	300 $\mu\text{m}$	121 $\mu\text{m}$	66 $\mu\text{m}$
	850 kg	300 $\mu\text{m}$	115 $\mu\text{m}$	
	900 kg	300 $\mu\text{m}$	103 $\mu\text{m}$	
	550 kg	300 $\mu\text{m}$		72 $\mu\text{m}$
	600 kg	300 $\mu\text{m}$		68 $\mu\text{m}$

gasket material.

As discussed in chapter 2, gaskets made of various materials (stainless steel, inox, inconel) were tested to achieve reliable pressure for electric resistivity measurement. Table B.1 presents the indented gasket thickness at various loads of MP35N, V56004 stainless steel and inconel. The indentation of gasket made of stainless steel (V56004) at various load with 1.1 mm diameter diamond culet is presented in Fig. B.4. When diamonds with smaller culet size were used the indentation, the required load considerably dropped and final indented thickness of gasket reduced.

# Appendix C

## Additional X-ray diffraction results

A few additional topics of XRD experiments under pressure. The preliminary XRD under pressure of  $\text{EuRhGe}_3$  was performed by using laboratory x-ray source. A comparison between lab XRD and synchrotron XRD data is presented. The neon PTM crystalizes around 6 GPa at room temperature, and Bragg reflections from solidified neon are also observed in XRD patterns. The EOS fitting was performed on neon. The quality of EOS fitting and visual assesment of  $\text{EuCoGe}_3$  is also presented. This section also covers powder XRD data processing using Diop-tas program, and extracted lattice constants from single crystal XRD experiment under pressure of  $\text{EuIrGe}_3$ .

### C.0.1 Synchrotron vs lab XRD under pressure

A direct comparison between synchrotron and lab XRD under high pressures is not entirely equitable. Synchrotron offer advantages over laboratory XRD setups, including tunable, intense, and collimated X-ray beams. This comparison underscores the necessity of synchrotron experiments for high-pressure studies. As depicted in Fig. C.1, synchrotrons yield superior data quality, with more distinct diffraction peaks and better resolution compared to laboratory XRD instruments. The XRD peaks are at different angles due to different wavelengths used in the experiments, lab XRD ( $0.7107 \text{ \AA}$ ) and synchrotron ( $0.3738 \text{ \AA}$ ). The signal-to-noise ratio is better in Synchrotron XRD data in comparison to lab XRD data, which plays an important role in extracting the atomic coordinates from XRD.

### C.0.2 EOS fitting of pressure transmitting medium neon

Figure C.2 (a) presents the pressure dependent unit cell volume of neon obtained during the XRD experiment of  $\text{EuCoGe}_3$  under pressure compared with data from Ref. [94] and Ref. [98].

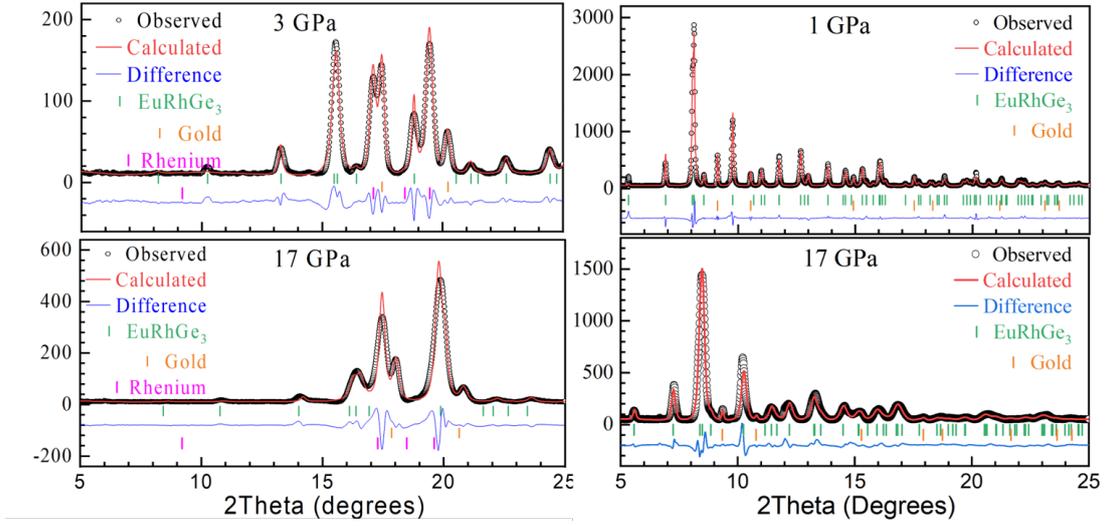


Figure C.1: Comparison of laboratory and synchrotron XRD data of  $\text{EuRhGe}_3$  at low and high pressures.

The result of fitting analysis by using  $3^{\text{rd}}$  order BM EOS is presented in Fig. C.2(b). The unit cell volume at 0 GPa  $V_0 = 88.967 \text{ \AA}^3$  from Ref. [98] was used, and obtained bulk modulus and its pressure derivative  $B_0 = 1.15 \pm 0.06 \text{ GPa}$ ,  $B'_0 = 9.0 \pm 0.3$  are in good agreement with the earlier studies [94].

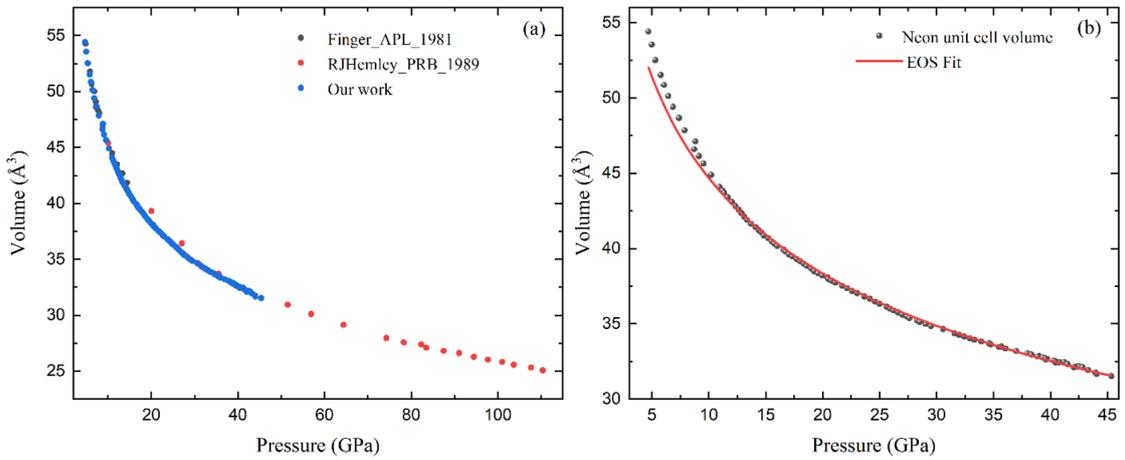


Figure C.2: (a) Pressure dependent unit cell volume of neon obtained from XRD experiment compared with data in Ref. [94] and [98]. (b) Pressure dependent unit cell volume of neon and the result of  $3^{\text{rd}}$  order BM EOS fitting with  $V_0 = 88.967 \text{ \AA}^3$  [98].

### C.0.3 Different EOS fitting and quality of EOS Fit

The most commonly used EOS fittings are BM and Vinet EOS. A comparison between 3<sup>rd</sup> order BM and Vinet EOS fitting of EuTGe<sub>3</sub> and extracted B<sub>0</sub> and its pressure derivative B'<sub>0</sub> are presented in table C.1.

Table C.1: Comparison between different EOS fitting methods for EuTGe<sub>3</sub> unit cell volume.

Compound	EOS Method	Unit cell volume (V <sub>0</sub> )	Bulk modulus (B <sub>0</sub> )	B' <sub>0</sub>
EuCoGe <sub>3</sub>	BM	184.39 (Å <sup>3</sup> )	75.6	5.58
	Vinet	184.39 (Å <sup>3</sup> )	74.5	5.87
EuRhGe <sub>3</sub>	BM	196.5 (Å <sup>3</sup> )	73	5.4
	Vinet	196.5 (Å <sup>3</sup> )	72.3	5.7
EuIrGe <sub>3</sub>	BM	197.9 (Å <sup>3</sup> )	101.42	3.79
	Vinet	197.9 (Å <sup>3</sup> )	100.86	3.93

Figure C.3 (a) presents the F-f plot (Normalized pressure F vs Eulerian strain f) for 3<sup>rd</sup> order BM EOS fitting of EuCoGe<sub>3</sub>. Here Eulerian strain (f) and normalized pressure (F) are defined as;

$$f = \frac{\left(\frac{V_0}{V}\right)^{2/3} - 1}{2} \text{ and } F = \frac{P}{(3f(1+2f)^{5/2})}.$$

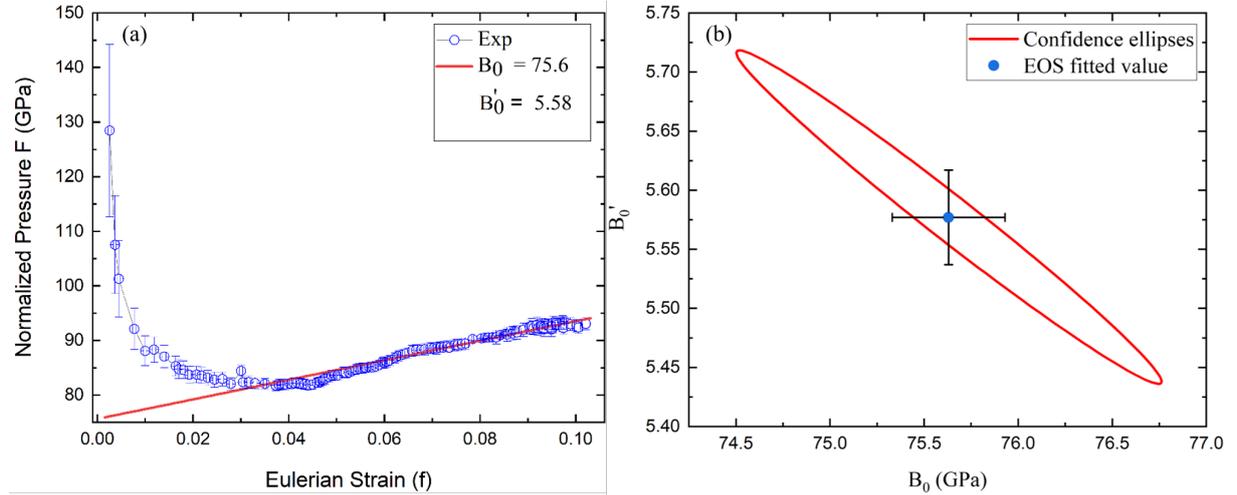


Figure C.3: Visual quality assessment of EOS fitting. (a) Normalized pressure F vs Eulerian strain f plot of EuCoGe<sub>3</sub>. The red line presents the linear fit by using  $F = B_0 + [3B_0 (B'_0 - 4)f]/2$ . (b) The confidence ellipse between B<sub>0</sub> and B'<sub>0</sub>. Confidence ellipse is presented for 99.73 percent confidence level.

## C.0.4 Powder XRD data processing

As mentioned in chapter 2, the powder XRD data integration was done by using Dioptas [72]. The data were collected as image files, which require image reduction/integration process to extract structural information from the measured XRD patterns. Dioptas is a Python-based program for on-the-fly data processing and exploration of two-dimensional X-ray diffraction area detector data, specifically designed for the large amount of data collected at XRD beamlines at synchrotrons. Figure C.4 and Fig. C.5 present the XRD image processing without mask and with masking. The figure on right hand side are the extracted diffractogram where one can also observe the peaks from diamonds and detector without mask.

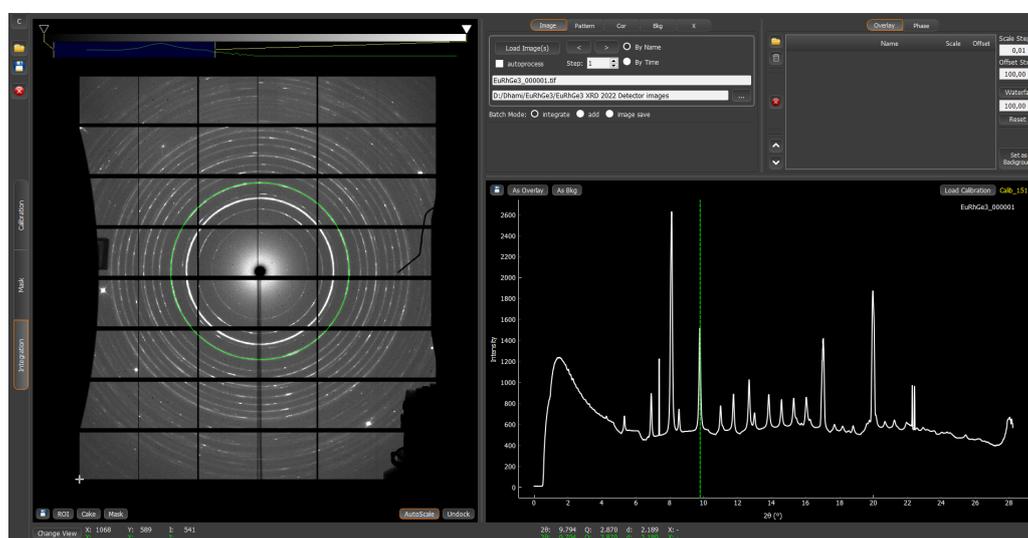


Figure C.4: Dioptas windows of raw XRD image (left) and extracted diffractogram (right) without mask.

## C.0.5 $\text{EuIrGe}_3$ single crystal XRD under pressure

Single crystal XRD under pressure was performed on  $\text{EuIrGe}_3$ . Due to a limited opening of DAC windows, a small part of reciprocal space was detected. that restricted a thorough analysis of possible structural transition under pressure. By using CrisAlisPro and preserving the I4mm (107) symmetry, lattice parameters at selected pressures could be extracted. The extracted lattice parameters and unit cell volume are presented in table C.2. The obtained unit cell volumes are plotted with powder XRD and DFT calculated data in Fig. 3.21 (a).

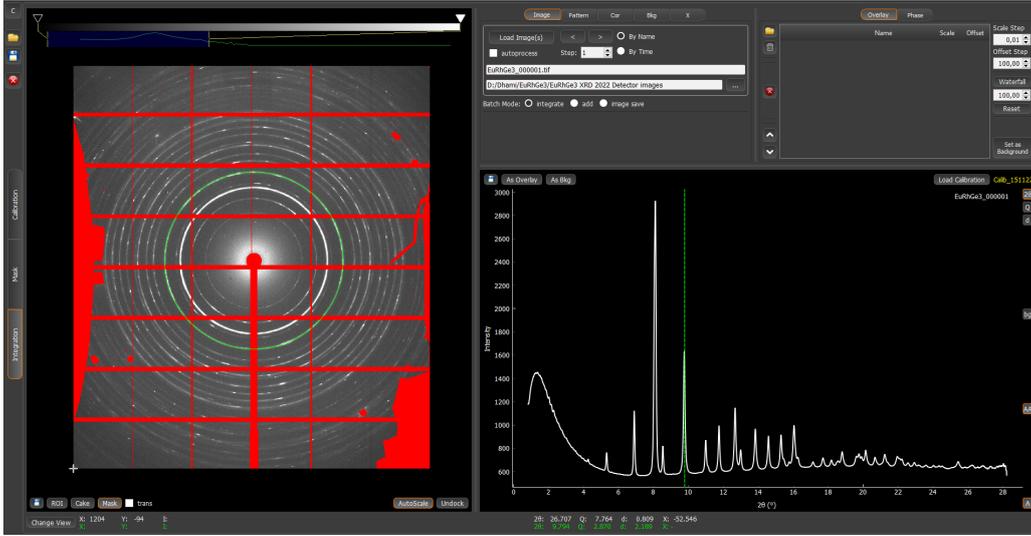


Figure C.5: Dioplas windows of raw XRD (left) and extracted diffractogram (right) with mask. Application of mask removes the peaks generated from diamonds and/or detector.

Table C.2: Experimental lattice parameters, unit cell volume of  $\text{EuIrGe}_3$  at selected pressures for sample 1 and 2.

Pressure	0 GPa	7.8 GPa	30 GPa	40 GPa
<b>Sample 1</b>				
a (Å)	4.4358 (4)	4.325 (2)	4.1164(2)	4.018(5)
c (Å)	10.058 (1)	9.875(6)	9.599(5)	9.421 (1)
V (Å <sup>3</sup> )	197.91 (4)	184.72 (8)	162.65 (2)	152.1 (9)
<b>Sample 2</b>				
a (Å)	4.434 (5)	4.322 (7)	4.1182 (7)	3.955(7)
c (Å)	10.055 (9)	9.894(6)	9.556 (2)	9.410 (1)
V (Å <sup>3</sup> )	197.68 (4)	184.81(2)	162.1 (2)	147.2 (3)

### C.0.6 $\text{EuRhGe}_3$ XRD under pressure with neon PTM

In chapter 3, XRD experiments of  $\text{EuRhGe}_3$  under pressure using helium PTM was presented. Additionally synchrotron powder XRD of  $\text{EuRhGe}_3$  was measured at room temperature using neon PTM. The experimental conditions are the same as described chapter 2. Due to the small amount of sample in the DAC (as one can also see the relative intensity of diffraction peaks of  $\text{EuRhGe}_3$  compares to that of Au peaks in Fig.C.6). The quality of the data was considered insufficient to present in the main text. The data is presented here to emphasize, that regardless of the data quality and different PTM, the anisotropic compression between a and c lattice parameters is present. The anisotropic pressure behaviors in Fig. 3.17 and Fig. C.7, and the

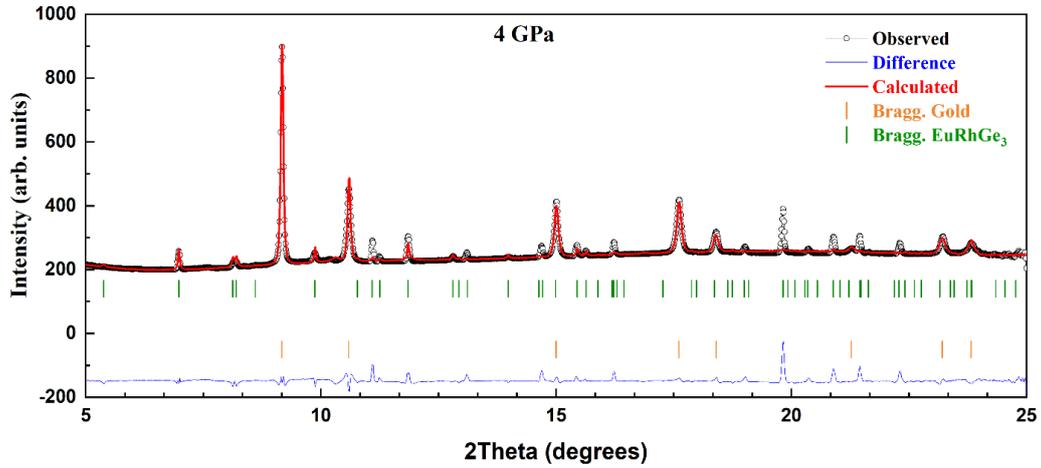


Figure C.6: Synchrotron powder XRD pattern of  $\text{EuRhGe}_3$  along with the results of Rietveld refinement with neon PTM, showing the dominance of gold signal over  $\text{EuRhGe}_3$ .

obtained  $B_0$  and  $B'_0$  by EOS fitting are consistent with those values obtained with helium PTM.

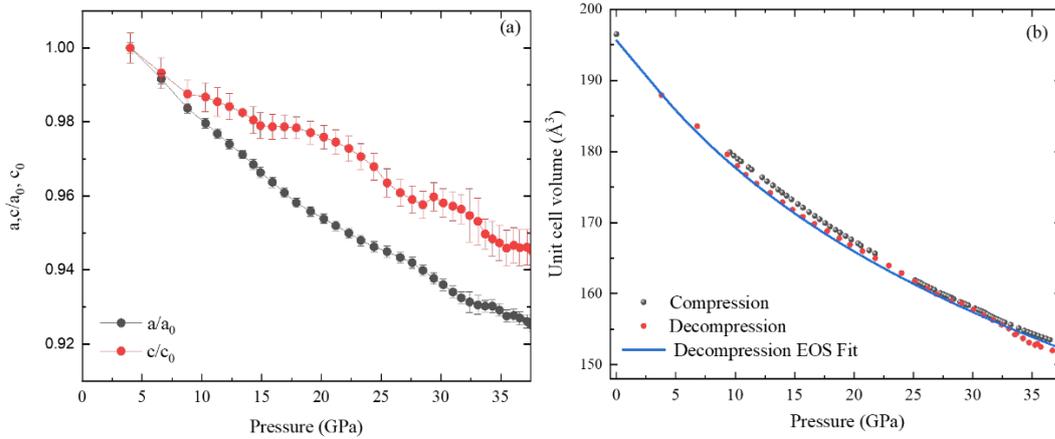


Figure C.7: (a) Pressure variation of the lattice parameters of  $\text{EuRhGe}_3$ . (b) Pressure-dependent unit cell volume of  $\text{EuRhGe}_3$  by using neon PTM. Black and red dots represent the data obtained during compression and decompression processes, respectively. Here, the EOS fit is applied to the decompression data.

### C.0.7 XRD and DFT extracted atomic coordinates as function of pressure of $\text{EuTGe}_3$ compounds

Tables C.3, C.4, and C.5 present the atomic coordinates of  $\text{EuCoGe}_3$ ,  $\text{EuRhGe}_3$ , and  $\text{EuIrGe}_3$ , respectively. Crystallographic Information File (CIF) files were extracted using profex after performing Rietveld refinement. CIF file contains information, lattice parameters, unit cell volume, lattice angles, occupation, atomic coordinates, and space group etc. Here in the afformentioned tables only contain atomic coordinates extracted from the XRD experiment and its comparison with DFT calculated atomic coordinates to avoid complexity.

Table C.3: Atomic coordinates for  $\text{EuCoGe}_3$  under pressure extracted from refinement of XRD data and DFT calculation.

Pressure	Atoms	Symmetry	XRD			DFT		
			x	y	z	x	y	z
0 GPa								
	Eu	2a	0.0	0.0	0.0	0.0	0.0	0.0
	Co	2a	0.0	0.0	0.3384	0.0	0.0	0.3415
	Ge1	4b	0.0	0.5	0.2499	0.0	0.5	0.2477
	Ge2	2a	0.0	0.0	0.5702	0.0	0.0	0.5717
10 GPa								
	Eu	2a	0.0	0.0	0.0	0.0	0.0	0.0
	Co	2a	0.0	0.0	0.3432	0.0	0.0	0.3441
	Ge1	4b	0.0	0.5	0.2488	0.0	0.5	0.2476
	Ge2	2a	0.0	0.0	0.5802	0.0	0.0	0.5745
20 GPa								
	Eu	2a	0.0	0.0	0.0	0.0	0.0	0.0
	Co	2a	0.0	0.0	0.3467	0.0	0.0	0.3460
	Ge1	4b	0.0	0.5	0.2501	0.0	0.5	0.2475
	Ge2	2a	0.0	0.0	0.5801	0.0	0.0	0.5761
30 GPa								
	Eu	2a	0.0	0.0	0.0	0.0	0.0	0.0
	Co	2a	0.0	0.0	0.3500	0.0	0.0	0.3475
	Ge1	4b	0.0	0.5	0.2511	0.0	0.5	0.2473
	Ge2	2a	0.0	0.0	0.5761	0.0	0.0	0.5773
40 GPa								
	Eu	2a	0.0	0.0	0.0	0.0	0.0	0.0
	Co	2a	0.0	0.0	0.3567	0.0	0.0	0.3488
	Ge1	4b	0.0	0.5	0.2505	0.0	0.5	0.2472
	Ge2	2a	0.0	0.0	0.5748	0.0	0.0	0.5783

Table C.4: Atomic coordinates for  $\text{EuRhGe}_3$  under pressure extracted from refinement of XRD data and DFT calculation.

Pressure	Atoms	Symmetry	XRD			DFT		
			x	y	z	x	y	z
0 GPa								
	Eu	2a	0.0	0.0	0.0	0.0	0.0	0.0
	Rh	2a	0.0	0.0	0.3544	0.0	0.0	0.3488
	Ge1	4b	0.0	0.5	0.2425	0.0	0.5	0.2435
	Ge2	2a	0.0	0.0	0.5812	0.0	0.0	0.5864
10 GPa								
	Eu	2a	0.0	0.0	0.0	0.0	0.0	0.0
	Rh	2a	0.0	0.0	0.3542	0.0	0.0	0.3514
	Ge1	4b	0.0	0.5	0.2404	0.0	0.5	0.2423
	Ge2	2a	0.0	0.0	0.5816	0.0	0.0	0.5886
20 GPa								
	Eu	2a	0.0	0.0	0.0	0.0	0.0	0.0
	Rh	2a	0.0	0.0	0.3542	0.0	0.0	0.3532
	Ge1	4b	0.0	0.5	0.2395	0.0	0.5	0.2412
	Ge2	2a	0.0	0.0	0.5853	0.0	0.0	0.5897
30 GPa								
	Eu	2a	0.0	0.0	0.0	0.0	0.0	0.0
	Rh	2a	0.0	0.0	0.3555	0.0	0.0	0.3547
	Ge1	4b	0.0	0.5	0.2406	0.0	0.5	0.2404
	Ge2	2a	0.0	0.0	0.5815	0.0	0.0	0.5903
40 GPa								
	Eu	2a				0.0	0.0	0.0
	Rh	2a				0.0	0.0	0.3557
	Ge1	4b				0.0	0.5	0.2394
	Ge2	2a				0.0	0.	0.5905

Table C.5: Atomic coordinates for EuIrGe<sub>3</sub> under pressure extracted from refinement of XRD data and DFT calculation.

Pressure	Atoms	Symmetry	XRD			DFT		
			x	y	z	x	y	z
0 GPa								
	Eu	2a	0.0	0.0	0.0	0.0	0.0	0.0
	Ir	2a	0.0	0.0	0.3544	0.0	0.0	0.3490
	Ge1	4b	0.0	0.5	0.2425	0.0	0.5	0.2432
	Ge2	2a	0.0	0.0	0.58124	0.0	0.0	0.5867
10 GPa								
	Eu	2a	0.0	0.0	0.0	0.0	0.0	0.0
	Ir	2a	0.0	0.0	0.35428	0.0	0.0	0.3518
	Ge1	4b	0.0	0.5	0.24044	0.0	0.5	0.2413
	Ge2	2a	0.0	0.0	0.5816	0.0	0.0	0.5897
20 GPa								
	Eu	2a	0.0	0.0	0.0	0.0	0.0	0.0
	Ir	2a	0.0	0.0	0.35427	0.0	0.0	0.3535
	Ge1	4b	0.0	0.5	0.2395	0.0	0.5	0.2397
	Ge2	2a	0.0	0.0	0.5853	0.0	0.0	0.5910
30 GPa								
	Eu	2a	0.0	0.0	0.0	0.0	0.0	0.0
	Ir	2a	0.0	0.0	0.3555	0.0	0.0	0.3549
	Ge1	4b	0.0	0.5	0.2406	0.0	0.5	0.2385
	Ge2	2a	0.0	0.0	0.5815	0.0	0.0	0.5918
40 GPa								
	Eu	2a				0.0	0.0	0.0
	Ir	2a				0.0	0.0	0.3559
	Ge1	4b				0.0	0.5	0.2373
	Ge2	2a				0.0	0.	0.5920

# References

- [1] E. Dagotto, *Reviews of Modern Physics* **66**, 763 (1994).
- [2] M. Brahlek, L. Zhang, J. Lapano, H.-T. Zhang, R. Engel-Herbert, N. Shukla, S. Datta, H. Paik and D. G. Schlom, *MRS Communications* **7**, 27 (2017).
- [3] B. Coqblin, (The electronic structure of rare-earth metals and alloys, the magnetic heavy rare-earths) (1977).
- [4] F. Steglich, J. Aarts, C. D. Bredl, W. Lieke, D. Meschede, W. Franz and H. Schäfer, *Phys. Rev. Lett.* **43**, 1892 (1979).
- [5] C. Pfleiderer, *Rev. Mod. Phys.* **81**, 1551 (2009).
- [6] J. Lawrence, P. Riseborough and R. Parks, *Reports on Progress in Physics* **44**, 1 (1981).
- [7] B. Johansson and S. Li, *Philosophical Magazine* **89**, 1793 (2009).
- [8] P. Coleman, arXiv preprint arXiv:1509.05769 (2015).
- [9] W. De Haas, J. De Boer and G. Van den Berg, *Physica* **1**, 1115 (1934).
- [10] J. Kondo, *Progress of theoretical physics* **32**, 37 (1964).
- [11] Y. Nagaoka, *Physical Review* **138**, A1112 (1965).
- [12] K. Yosida and A. Yoshimori, *Progress of Theoretical Physics* **42**, 753 (1969).
- [13] S. Doniach, *physica B+ C* **91**, 231 (1977).
- [14] J. Kroha, arXiv preprint arXiv:1710.00192 (2017).
- [15] N. Mathur, F. Grosche, S. Julian, I. Walker, D. Freye, R. Haselwimmer and G. Lonzarich, *Nature* **394**, 39 (1998).
- [16] T. Takimoto, *Journal of the Physical Society of Japan* **77**, 113706 (2008), [<https://doi.org/10.1143/JPSJ.77.113706>].
- [17] T. Takimoto and P. Thalmeier, *Journal of the Physical Society of Japan* **78**, 103703 (2009).
- [18] N. Kimura, K. Ito, K. Saitoh, Y. Umeda, H. Aoki and T. Terashima, *Phys. Rev. Lett.* **95**, 247004 (2005).
- [19] R. Settai, I. Sugitani, Y. Okuda, A. Thamizhavel, M. Nakashima, Y. Ōnuki and H. Harima, *Journal of magnetism and magnetic materials* **310**, 844 (2007).
- [20] I. Sugitani, Y. Okuda, H. Shishido, T. Yamada, A. Thamizhavel, E. Yamamoto, T. D. Matsuda, Y. Haga, T. Takeuchi, R. Settai and Y. Onuki, *Journal of the Physical Society of Japan* **75**, 043703 (2006), [<https://doi.org/10.1143/JPSJ.75.043703>].
- [21] F. Honda, I. Bonalde, S. Yoshiuchi, Y. Hirose, T. Nakamura, K. Shimizu, R. Settai and Y. Ōnuki, *Physica C: Superconductivity and its applications* **470**, S543 (2010).
- [22] Y. A. Svane, W. Temmerman and Z. Szotek, *Physical Review B* **59**, 7888 (1999).
- [23] A. Jayaraman, P. Dernier and L. Longinotti, *Physical Review B* **11**, 2783 (1975).
- [24] J.-M. Mignot, I. Goncharenko, P. Link, T. Matsumura and T. Suzuki, *Hyperfine interactions* **128**, 207 (2000).
- [25] C. Varma, *Reviews of Modern physics* **48**, 219 (1976).
- [26] K. Momma and F. Izumi, *Journal of Applied Crystallography* **44**, 1272 (2011).
- [27] J. M. Coey, *Magnetism and magnetic materials* (Cambridge university press, 2010).
- [28] S. Seiro and C. Geibel, *Journal of Physics: Condensed Matter* **23**, 375601 (2011).

- [29] M. Nakashima, Y. Amako, K. Matsubayashi, Y. Uwatoko, M. Nada, K. Sugiyama, M. Hagiwara, Y. Haga, T. Takeuchi, A. Nakamura, H. Akamine, K. Tomori, T. Yara, Y. Ashitomi, M. Hedo, T. Nakama and Y. Ōnuki, *Journal of the Physical Society of Japan* **86**, 034708 (2017), [<https://doi.org/10.7566/JPSJ.86.034708>].
- [30] S. Seiro, K. Kummer, D. Vyalikh, N. Caroca-Canales and C. Geibel, *physica status solidi (b)* **250**, 621 (2013).
- [31] I. Harris and G. Raynor, *Journal of the Less Common Metals* **9**, 263 (1965).
- [32] E. R. Bauminger, D. Froindlich, I. Nowik, S. Ofer, I. Felner and I. Mayer, *Phys. Rev. Lett.* **30**, 1053 (1973).
- [33] F. Honda, K. Okauchi, A. Nakamura, D. Aoki, H. Akamine, Y. Ashitomi, M. Hedo, T. Nakama and Y. Ōnuki, Pressure evolution of characteristic electronic states in *euRh2Si2* and *euni2Ge2*, in *Journal of Physics: Conference Series* Vol. 807, p. 022004, IOP Publishing, 2017.
- [34] F. Honda, K. Okauchi, A. Nakamura, D. Li, D. Aoki, H. Akamine, Y. Ashitomi, M. Hedo, T. Nakama and Y. Ōnuki, *Journal of the Physical Society of Japan* **85**, 063701 (2016).
- [35] F. Honda, K. Okauchi, A. Nakamura, D. Aoki, H. Akamine, Y. Ashitomi, M. Hedo, T. Nakama and Y. Ōnuki, Pressure evolution of characteristic electronic states in *euRh2Si2* and *euni2Ge2*, in *Journal of Physics: Conference Series* Vol. 807, p. 022004, IOP Publishing, 2017.
- [36] A. Nakamura, T. Nakama, K. Uchima, N. Arakaki, C. Zukeran, S. Komesu, M. Takeda, Y. Takaesu, D. Nakamura, M. Hedo *et al.*, Effect of pressure on thermopower of *euni2Ge2*, in *Journal of Physics: Conference Series* Vol. 400, p. 032106, IOP Publishing, 2012.
- [37] C. Huhnt, W. Schlabitz, A. Wurth, A. Mewis and M. Reehuis, *Physica B: Condensed Matter* **252**, 44 (1998).
- [38] M. Bishop, W. Uhoya, G. Tsoi, Y. K. Vohra, A. S. Sefat and B. C. Sales, *Journal of Physics: Condensed Matter* **22**, 425701 (2010).
- [39] H.-J. Hesse, R. Lübbbers, M. Winzenick, H. Neuling and G. Wortmann, *Journal of Alloys and Compounds* **246**, 220 (1997).
- [40] C. Huhnt, W. Schlabitz, A. Wurth, A. Mewis and M. Reehuis, *Physical Review B* **56**, 13796 (1997).
- [41] O. Bednarchuk, A. Gagor and D. Kaczorowski, *Journal of Alloys and Compounds* **622**, 432 (2015).
- [42] O. Bednarchuk and D. Kaczorowski, *Journal of Alloys and Compounds* **646**, 291 (2015).
- [43] O. Bednarchuk and D. Kaczorowski, *Acta Physica Polonica A* **127**, 418 (2015).
- [44] M. Kakihana, H. Akamine, K. Tomori, K. Nishimura, A. Teruya, A. Nakamura, F. Honda, D. Aoki, M. Nakashima, Y. Amako, K. Matsubayashi, Y. Uwatoko, T. Takeuchi, T. Kida, M. Hagiwara, Y. Haga, E. Yamamoto, H. Harima, M. Hedo, T. Nakama and Y. Ōnuki, *Journal of Alloys and Compounds* **694**, 439 (2017).
- [45] A. Maurya, P. Bonville, A. Thamizhavel and S. K. Dhar, *Journal of Physics: Condensed Matter* **26**, 216001 (2014).
- [46] A. Maurya, P. Bonville, R. Kulkarni, A. Thamizhavel and S. Dhar, *Journal of Magnetism and Magnetic Materials* **401**, 823 (2016).
- [47] T. Matsumura, M. Tsukagoshi, Y. Ueda, N. Higa, A. Nakao, K. Kaneko, M. Kakihana, M. Hedo, T. Nakama and Y. Ōnuki, *Journal of the Physical Society of Japan* **91**, 073703 (2022).
- [48] A. Nakamura, T. Okazaki, M. Nakashima, Y. Amako, K. Matsubayashi, Y. Uwatoko, S. Kayama, T. Kagayama, K. Shimizu, T. Uejo *et al.*, *Journal of the Physical Society of Japan* **84**, 053701 (2015).
- [49] K. Uchima, N. Arakaki, S. Hirakawa, Y. Hiranaka, T. Uejo, A. Teruya, A. Nakamura, M. Takeda, Y. Takaesu, M. Hedo, T. Nakama, K. Yagasaki and Y. Uwatoko, *Pressure Effect on Transport Properties of EuNiGe3*, , <https://journals.jps.jp/doi/pdf/10.7566/JPSJ.1.012015>.
- [50] S. E. Muthu, D. Braithwaite, B. Salce, S. Arumugam, L. Govindaraj, C. Saravanan, M. Kanagaraj, S. Sarkar and S. C. Peter, *Journal of the Physical Society of Japan* **88**, 074702 (2019), [<https://doi.org/10.7566/JPSJ.88.074702>].
- [51] O. Bednarchuk, A. Gagor and D. Kaczorowski, *Journal of Alloys and Compounds* **622**, 432 (2015).
- [52] C. Weir, E. Lippincott, A. Van Valkenburg and E. Bunting, *Journal of research of the National Bureau of Standards. Section A, Physics and chemistry* **63**, 55 (1959).

- [53] E. F. O'Bannon, Z. Jenei, H. Cynn, M. J. Lipp and J. R. Jeffries, *Review of Scientific Instruments* **89** (2018).
- [54] D. Dunstan, *Review of scientific instruments* **60**, 3789 (1989).
- [55] K. Syassen, *High Pressure Research* **28**, 75 (2008).
- [56] R. A. Forman, G. J. Piermarini, J. D. Barnett and S. Block, *Science* **176**, 284 (1972).
- [57] H. Yamaoka, Y. Zekko, I. Jarrige, J.-F. Lin, N. Hiraoka, H. Ishii, K.-D. Tsuei and J. Mizuki, *Journal of Applied Physics* **112** (2012).
- [58] I. F. Silvera, A. D. Chijioke, W. Nellis, A. Soldatov and J. Tempere, *physica status solidi (b)* **244**, 460 (2007).
- [59] F. Birch, *Phys. Rev.* **71**, 809 (1947).
- [60] D. L. Heinz and R. Jeanloz, *Journal of applied physics* **55**, 885 (1984).
- [61] A. Eiling and J. Schilling, *Journal of Physics F: Metal Physics* **11**, 623 (1981).
- [62] Y. Han, C. Gao, Y. Ma, H. Liu, Y. Pan, J. Luo, M. Li, C. He, X. Huang, G. Zou *et al.*, *Applied Physics Letters* **86** (2005).
- [63] C. Rotundu, T. Čuk, R. Greene, Z.-X. Shen, R. J. Hemley and V. Struzhkin, *Review of Scientific Instruments* **84** (2013).
- [64] J.-P. Rueff and A. Shukla, *Reviews of Modern Physics* **82**, 847 (2010).
- [65] J. M. Ablett, S. R. Shieh, V. Balédent, J. C. Woicik, E. Cockayne and E. L. Shirley, *Phys. Rev. B* **104**, 054119 (2021).
- [66] J.-P. Rueff, J. M. Ablett, D. Céolin, D. Prieur, T. Moreno, V. Balédent, B. Lassalle-Kaiser, J. E. Rault, M. Simon and A. Shukla, *Journal of Synchrotron Radiation* **22**, 175 (2015).
- [67] J. M. Ablett, D. Prieur, D. Céolin, B. Lassalle-Kaiser, B. Lebert, M. Sauvage, T. Moreno, S. Bac, V. Balédent, A. Ovono, M. Morand, F. Gélebart, A. Shukla and J.-P. Rueff, *Journal of Synchrotron Radiation* **26**, 263 (2019).
- [68] H. K. Mao, J. Xu and P. M. Bell, *Journal of Geophysical Research: Solid Earth* **91**, 4673 (1986).
- [69] G. Shen and H. K. Mao, *Reports on Progress in Physics* **80**, 016101 (2016).
- [70] R. Letoullec, J. Pinceaux and P. Loubeyre, *International Journal of High Pressure Research* **1**, 77 (1988).
- [71] A. King, N. Guignot, J.-P. Deslandes, M. Pelerin, I. Joosten, D. De Loeff, J. Li, L. Bertrand, E. Rosenberg, A. Dewaele *et al.*, *Integrating Materials and Manufacturing Innovation* **8**, 551 (2019).
- [72] C. Prescher and V. B. Prakapenka, *High Pressure Research* **35**, 223 (2015).
- [73] A. Rothkirch, G. D. Gatta, M. Meyer, S. Merkel, M. Merlini and H.-P. Liermann, *Journal of Synchrotron Radiation* **20**, 711 (2013).
- [74] V. Petříček, L. Palatinus, J. Plášil and M. Dušek, *Zeitschrift für Kristallographie-Crystalline Materials* **238**, 271 (2023).
- [75] G. S. Henderson, F. M. De Groot and B. J. Moulton, *Reviews in Mineralogy and Geochemistry* **78**, 75 (2014).
- [76] E. K. Hlil, R. Baudoing-Savois, B. Moraweck and A. J. Renouprez, *The Journal of Physical Chemistry* **100**, 3102 (1996), [<https://doi.org/10.1021/jp951440t>].
- [77] G. Vankó, J.-P. Rueff, A. Mattila, Z. Németh and A. Shukla, *Phys. Rev. B* **73**, 024424 (2006).
- [78] M. Kim, Y. Im, E. Oh, K. Kim and C. Yo, *Physica B: Condensed Matter* **229**, 338 (1997).
- [79] A. Rogalev, F. Wilhelm, E. Ovchinnikova, A. Enikeev, R. Bakonin, K. Kozlovskaya, A. Oreshko, D. Aoki and V. E. Dmitrienko, *Crystals* **11** (2021).
- [80] Y. Mizuguchi, E. Paris, T. Wakita, G. Jinno, A. Puri, K. Terashima, B. Joseph, O. Miura, T. Yokoya and N. L. Saini, *Phys. Rev. B* **95**, 064515 (2017).
- [81] Y. Utsumi, I. Batistić, V. Balédent, S. Shieh, N. Dhami, O. Bednarchuk, D. Kaczorowski, J. Ablett and J.-P. Rueff, *Electronic Structure* **3**, 034002 (2021).
- [82] B. Ravel and M. Newville, *Journal of synchrotron radiation* **12**, 537 (2005).
- [83] V. Monteseuro, J. Sans, V. Cuartero, F. Cova, I. A. Abrikosov, W. Olovsson, C. Popescu, S. Pascarelli, G. Garbarino, H. J. M. Jönsson *et al.*, *Scientific reports* **9**, 8940 (2019).

- [84] Y. Utsumi, D. Kasinathan, P. Swatek, O. Bednarchuk, D. Kaczorowski, J. M. Ablett and J.-P. Rueff, *Phys. Rev. B* **97**, 115155 (2018).
- [85] N. Doebelin and R. Kleeberg, *Journal of Applied Crystallography* **48**, 1573 (2015).
- [86] P. Giannozzi *et al.*, *Journal of Physics: Condensed Matter* **21**, 395502 (2009).
- [87] P. Giannozzi, O. Andreussi, T. Brumme, O. Bunau, M. B. Nardelli, M. Calandra, R. Car, C. Cavazzoni, D. Ceresoli, M. Cococcioni *et al.*, *Journal of physics: Condensed matter* **29**, 465901 (2017).
- [88] A. Dal Corso, *Computational Materials Science* **95**, 337 (2014).
- [89] J. P. Perdew, A. Ruzsinszky, G. I. Csonka, O. A. Vydrov, G. E. Scuseria, L. A. Constantin, X. Zhou and K. Burke, *Physical review letters* **100**, 136406 (2008).
- [90] J. P. Perdew, A. Ruzsinszky, G. I. Csonka, O. A. Vydrov, G. E. Scuseria, L. A. Constantin, X. Zhou and K. Burke, *Phys. Rev. Lett.* **102**, 039902 (2009).
- [91] N. Marzari, D. Vanderbilt, A. De Vita and M. Payne, *Physical review letters* **82**, 3296 (1999).
- [92] S. L. Dudarev, G. A. Botton, S. Y. Savrasov, C. J. Humphreys and A. P. Sutton, *Phys. Rev. B* **57**, 1505 (1998).
- [93] R. Angel, J. Gonzalez-Platas and M. Alvaro, *Zeitschrift für Kristallographie* (2014).
- [94] L. Finger, R. Hazen, G. Zou, H. Mao and P. Bell, *Applied Physics Letters* **39**, 892 (1981).
- [95] K. Chen, C. Luo, Y. Zhao, F. Baudelet, A. Maurya, A. Thamizhavel, U. Roßler, D. Makarov and F. Radu, *The Journal of Physical Chemistry Letters* **14**, 1000 (2023).
- [96] R. Settai, Y. Okuda, I. Sugitani, Y. Ōnuki, T. Matsuda, Y. Haga and H. Harima, *International Journal of Modern Physics B* **21**, 3238 (2007).
- [97] N. Fujiwara, N. Kawaguchi, S. Imura, S. Matsuishi and H. Hosono, Tc enhancement under pressure in the  $1a1111$  pnictide  $\text{LaFeAsO}_{1-x}\text{Hx}$  ( $x=0.2$ ) studied by nmr, in *Journal of Physics: Conference Series* Vol. 950, p. 042033, IOP Publishing, 2017.
- [98] R. Hemley, C. Zha, A. Jephcoat, H. Mao, L. Finger and D. Cox, *Physical Review B* **39**, 11820 (1989).

# Curriculum vitae

Naveen Singh Dhani

## Education

- 1 Doctor of Science (Physics), University of Zagreb, Croatia : 2019 - **Ongoing** : Doctoral thesis: Pressure evolutions of electronic and crystal structures of europium compounds
- 2 Master of Science (Physics), IIT Bombay, Mumbai, India : 2019: Master thesis: Electrolytic gating on gold thin film field effect transistors (FET)
- 3 Bachelor of Science, (Physics, Chemistry and Mathematics), S.S.J. Campus almora, Kumaun University Nainital, India : 2016

## Employment

- 1 Research Assistant: Institute of Physics, Zagreb, Croatia; 2019 - Ongoing.
- 2 Research Intern: Laboratoire de Physique des Solides (LPS), Orsay, France; 2018 (May - July)

## Awards and Fellowships

- 1 2023: Best poster presentation award in SCIRES (Solid-State Science & Research) 2023 international conference.
- 2 2023: Awarded with international scholarship for exchange of doctoral students by Polish National Agency for Academic Exchange, nawa.
- 3 2022: Best oral talk award in 6<sup>th</sup> international PhD symposium, university of Zagreb, Croatia.

## Conferences

### Invited talk

- 1 2023: Pressure evolution of electronic and crystal structures of  $\text{EuTGe}_3$  : 29th International Scientific Meeting on Vacuum Science and Technique (ISMVST) conference, Kranjska gora, Slovenia.
- 2 2019: Ionic liquid gating on thin gold films: Institute of Physics, Zagreb.

### Contributed talk

- 1 2023: Hydrostatic pressure effects on electronic and crystal structures of non-centrosymmetric  $\text{EuTGe}_3$  ( $T = \text{Co, Rh, and Ir}$ ): Zakopane School of Physics 2023, Zakopane, Poland
- 2 2022: Pressure evolution of electronic and crystal structures of  $\text{EuTGe}_3$ : ECmet AC Days 2022, Split, Croatia
- 3 2020: Electronic structure of  $\text{EuRhGe}_3$  under pressure: ECmet AC Days 2020, Online
- 4 2020: Spectroscopic measurement results on (europium based materials) strongly correlated systems: GEWP 2020 (Grandmaster Early career Workshop in Physics), Prague, Czech republic

### Poster Presentation

- 1 2023: ECMet AC days 2023, Kranjska Gora, Slovenia; Crystal structure study of non-centrosymmetric  $\text{EuTGe}_3$  ( $T = \text{Co, Rh, and Ir}$ ) under hydrostatic pressure.
- 2 2023: MPG-UBC-UTokyo Center 2023, MPI Dresden, 'X-rays for the study of quantum materials'. High energy resolution fluorescence detected XAS study of non-centrosymmetric  $\text{EuTGe}_3$  ( $T = \text{Co, Rh, and Ir}$ ) under pressure.
- 3 2023: SCIRES 2023: Hydrostatic pressure effects on electronic and crystal structures of non-centrosymmetric  $\text{EuTGe}_3$  ( $T = \text{Co, Rh, and Ir}$ ).
- 4 2022: SCTE 2022, Bordeaux, France: Pressure dependent electronic and crystal structure of  $\text{EuTGe}_3$  ( $T = \text{Co, Rh, and Ir}$ ).

## Publications

### Submitted

- 3 **Dhami, N.S.**, Balédent, V., Batistić, I., Bednarchuk O., Kaczorowski, D., Itié, J.P., Kumar, C.M.N. and Utsumi, Y., accepted for publication in, High Pressure Research. *Synchrotron x-ray diffraction and DFT study of non-centrosymmetric EuRhGe<sub>3</sub> under high pressure.*

### Published

- 3 Zorić, M., **Dhami, N.S.**, Bader, K., Gille, P., Smontara, A. and Popčević, P., 2023. Negative Magnetoresistance in Hopping Regime of Lightly Doped Thermoelectric SnSe. *Materials*, 16(7), p.2863
- 2 **Dhami, N. S.**, V. Balédent, O. Bednarchuk, D. Kaczorowski, S. R. Shieh, J. M. Ablett, J-P. Rueff, J. P. Itié, C. M. N. Kumar, and Y. Utsumi. "Pressure evolution of electronic and crystal structure of noncentrosymmetric EuCoGe<sub>3</sub>." *Physical Review B* 107, no. 15 (2023): 155119.
- 1 Utsumi, Y and Batistić, I and Balédent, V and Shieh, SR and **Dhami, N.S.** and Bednarchuk, O and Kaczorowski, D and Ablett, JM and Rueff, Jean-Pascal, Pressure evolution of the electronic structure of non-centrosymmetric EuRhGe<sub>3</sub>, *Electronic Structure*, 3, (2021), 034002